Karlsruhe Institute of Technology

ETP-KA/2018-21

Irradiation Studies of Charge Collection and Interstrip Resistance of Silicon Strip Sensors in the Course of the CMS Phase-2 Upgrade

Master Thesis

Jan-Ole Gosewisch

At the Department of Physics
Institut für Experimentelle Teilchenphysik (ETP)

Reviewer:	Prof. Dr. Thomas Müller
Second reviewer:	Prof. Dr. Ulrich Husemann
Advisor:	Dr. Alexander Dierlamm

Karlsruhe, 22 October 2018

This thesis has been accepted by the first reviewer of the master thesis.

Karlsruhe, 22 October 2018

.....

(**Prof. Dr. Thomas Müller**)

I declare that I have developed and written the enclosed thesis completely by myself, and have not used sources or means without declaration in the text.

Karlsruhe, 22 October 2018

.....

(**Jan-Ole Gosewisch**)

Contents

1. Introduction **1**

2. Particle Detection with Silicon Sensors **3**
2.1. Electrical Conductivity - Band Model . . . 3
2.2. Doping of Semiconductors . . . 4
2.3. Manufacturing of Silicon Wafers . . . 5
2.4. The pn-Junction . . . 6
2.5. Interaction of Particles in Matter . . . 8
2.6. Working Principle of Silicon Strip Sensors . . . 11
2.6.1. Interstrip Insulation . . . 12
2.6.2. p-Type Strip Sensor Design . . . 12
2.7. Irradiation of Silicon Strip Sensors . . . 12
2.7.1. Irradiation Effects on Sensor Properties . . . 14
2.7.2. Differences of n-in-p and p-in-n Sensors . . . 20

3. LHC and the CMS Phase-2 Upgrade **23**
3.1. The LHC at CERN . . . 23
3.2. The Concept of Integrated Luminosity . . . 23
3.3. The CMS Experiment . . . 25
3.4. Current CMS Tracker . . . 25
3.5. Outer Tracker in Phase-2 . . . 27

4. Experimental Setups **31**
4.1. Probe Station . . . 31
4.2. ALiBaVa Setup . . . 31
4.3. Irradiation Facilities . . . 38

5. Sensor Properties after Irradiation **41**
5.1. Quality Assurance of Sensor Properties after Irradiation . . . 41
5.2. Validation of Optimal Sensor Thickness for 2S Sensors . . . 42
5.3. Neutron versus Proton Irradiation . . . 44
5.4. Neutrons vs Protons of n-type Strip Sensors . . . 46
5.4.1. Pure Irradiations . . . 46
5.4.2. Mixed Irradiation . . . 48
5.5. Summary of Chapter 5 . . . 53

6. Interplay of Surface and Bulk Damage **55**
6.1. X-Ray Tube Characterisation . . . 56
6.2. Measurement Procedure . . . 58
6.3. Interstrip Properties Before Irradiation . . . 59
6.4. X-Ray Induced Surface Damage . . . 61
6.5. Combination of Surface and Bulk Damage . . . 61

7. Conclusion **67**

Bibliography **71**

Appendix **75**
A. Appendix to Chapter 3 75
B. Appendix to Chapter 4 77
C. Appendix to Chapter 5 79
D. Appendix to Chapter 6 81

List of Figures

2.1. Material classification via band model 4
2.2. Illustration of p-doped and n-doped silicon 5
2.3. Different manufacturing technologies for sensor grade silicon 6
2.4. Schematic illustration of deep diffused material 7
2.5. Scheme of a pn-junction 7
2.6. pn-junction in reverse bias 8
2.7. Plot of the Bethe equation 9
2.8. Typical straggling functions 10
2.9. Interactions of electrons in lead 10
2.10. Working principle of a silicon strip sensor 11
2.11. Possbile insulation structures between the strips of a n-in-p silicon sensor . 12
2.12. Sketch of the silicon strip sensor design 13
2.13. Displacement damage function dependent on the energy 14
2.14. Atomic displacements due to irradiation 15
2.15. Vacancy distribution due to irradiation 15
2.16. Irradiation induced defects in the band model scheme 16
2.17. Normalised leakage current over the fluence to monitor the damage rate . . 17
2.18. Leakage current affected by different annealing times and temperatures . . 18
2.19. Sensor capacitance before and after irradiation 19
2.20. Type inversion of n-type sensors due to irradiation 20
2.21. Comparison of the signal from n-type and p-type material after irradiation 21

3.1. Illustration of the CERN accelerator complex 24
3.2. Higgs-like event in CMS 24
3.3. The CMS detector 26
3.4. The CMS Tracker in Phase-1 26
3.5. Schematic illustration of the stub finding mechanism 27
3.6. The CMS Tracker in Phase-2 28
3.7. FLUKA expected fluences of the tracker in Phase-2 28
3.8. FLUKA expected particle type ratios in the tracker 29

4.1. Interior of the probe station at ETP 32
4.2. Picture of the ALiBaVa daughterboard with a sensor 32
4.3. Exemplary plot of the common mode distribution 34
4.4. Exemplary plot of the noise per strip of a sensor in the ALiBaVa setup . . . 34
4.5. Exemplary gain calibration plot 35
4.6. Operating modes of the ALiBaVa system 36
4.7. Signal timing with the ALiBaVa setup 36
4.8. Cluster signal with a Landau-Gaussian fit 37
4.9. Seed signal with a Landau-Gaussian fit 38
4.10. Relative number of seed events as a function of the applied cut 39
4.11. Picture of the x-ray irradiation setup 39

4.12. Picture of the sensor cooling whithin x-ray irradiation procedure 40

5.1. Damage rate at an operating voltage of 600 V 42
5.2. Seed signal of 200, 240 and 300 µm material 43
5.3. Seed signal of 240 µm and 300 µm material 43
5.4. Seed signal of 240 µm material for a fluence of $\Phi \approx 3 \cdot 10^{14} n_{eq}/cm^2$ 44
5.5. Seed signal of 240 µm Material at a fluence of $\Phi \approx 6 \cdot 10^{14} n_{eq}/cm^2$ 45
5.6. Comparison of annealing behaviours of 240 µm and 300 µm material at a fluence of $\Phi \approx 6 \cdot 10^{14} n_{eq}/cm^2$ 46
5.7. Annealing behaviour of magnetic Czochralski and diffusion oxygenated float zone material 47
5.8. CV characteristics of MCZ and DOFZ material after pure irradiations with $\Phi \approx 6 \cdot 10^{14} n_{eq}/cm^2$ 48
5.9. Signal and CV characteristics of FZ material after pure irradiations with $\Phi \approx 6 \cdot 10^{14} n_{eq}/cm^2$ 48
5.10. CV characteristics after mixed irradiation for deep diffused material 49
5.11. CV characteristics of MCZ material in mixed irradiations 50
5.12. CV characteristics of DOFZ material in mixed irradiations 50
5.13. CV characteristics of FZ material in mixed irradiations 50
5.14. Signal annealing behaviour after mixed irradiation for DOFZ and FZ material 51
5.15. Voltage dependence of the signal of DOFZ Material for different annealing . 52
5.16. Voltage dependence of the signal of FZ material for different annealing . . . 52
5.17. Mixed versus pure irradiation for FZ and DOFZ material 52
5.18. Signal dependence on the irradiation sequence for MCZ material 53
5.19. Signal behaviour after annealing of MCZ material in a mixed irradiation environment 53

6.1. Simulated interstrip resistance after a fluence of $\Phi \approx 1 \cdot 10^{15} n_{eq}/cm^2$ proton irradiation 56
6.2. Beamspot profiles of the x-ray tube 57
6.3. Cuts at 100 mm distance 58
6.4. Comparison of interstrip low voltage ramps 59
6.5. Interstrip parameters before irradiation at 300 V 60
6.6. Voltage dependence of the interstrip resistance without irradiation 60
6.7. Simulated interstrip resistance before irradiation 61
6.8. Interstrip resistance dependent on x-ray dose and annealing time 62
6.9. Interstrip resistance after x-ray irradiation for different temperatures 62
6.10. Interstrip resistance after proton irradiation 63
6.11. Comparison of the interstrip resistance after neutron and proton irradiation 64
6.12. Interstrip resistance after $\Phi \approx 3 \cdot 10^{14} n_{eq}/cm^2$ neutron irradiation with additional x-ray irradiation 65
6.13. Interstrip resistance after $\Phi \approx 6 \cdot 10^{14} n_{eq}/cm^2$ neutron irradiation with additional x-ray irradiation 65

A.1. FLUKA expected dose in Phase-2 75
A.2. p_T modules for Phase-2 76
B.1. Probe station at ETP 77
B.2. Beetle chip for LHCb 78
C.1. Picture of a KIT_Test and Irradiation type sensor 79
D.2. Picture of a No_Pstop sensor 81
D.3. Cuts at 300 mm distance 82
D.4. 3D heatmaps 82

List of Tables

3.1. Expected fluences and doses in Phase-2 regarding different regions 29

5.1. Oxygen concentrations of the four materials investigated within signal studies 47

B.1. Usual time and temperatures for annealing studies 77
C.2. Sensors with their name within the HPK campaign and the respective plot label 79
C.3. NitroStrip design sensors with the corresponding plot label and particle type 80
D.4. No_Pstop sensors with the plot label, thickness and project 81

1. Introduction

The Large Hadron Collider (LHC) at CERN in Geneva is the world's largest experimental facility in particle physics. It is constructed to accelerate protons and collide them up to a center of mass energy of 14 TeV. The products of the reactions are detected by massive detector complexes like ATLAS and CMS by which the Higgs boson was discovered simultaneously in 2012 [CER]. With the Higgs boson the *standard model of particle physics* was completed. It was developed over years after 1961 to describe the fundamental components of matter and their interactions. The predictions of the standard model were validated in the last decades [Wel].

The LHC will be upgraded to the High-Luminosity LHC (HL-LHC) in 2026. With this upgrade the luminosity, a parameter quantifying the reaction rate, will increase by a factor of five. This leads to an increased discovery potential. After the runtime of the HL-LHC, the size of datasets will be ten times higher than with the LHC [G+17].

With the HL-LHC the integrated luminosity will increase to 3000^{-1} fb corresponding to the Phase-2 of the CMS detector. This leads to increased radiation damage which requires more radiation hardness of the detectors. Therefore the CMS detector will be fully replaced and will have an increased granularity as well as other improvements besides the radiation hardness. In Phase-2 the Outer Tracker of CMS will consist of modules incorporating macropixel and strip sensors (PS) and two strip sensors (2S). The readout will be binary to accelerate the data transfer and decrease the amount of generated data.

This master thesis is divided into two parts. The first part focuses on the radiation hardness of n-in-p silicon strip sensors for the 2S requirements. Since the readout is binary, it has to be ensured that the sensors are able to generate a certain signal by a traversing charged particle. In case of the 2S sensors, a signal of 12 000 electrons has to be exceeded by one strip (seed signal) under the frame conditions of a maximum fluence of $\Phi = 3 \cdot 10^{14} \mathrm{n_{eq}/cm^2}$, a nominal operating voltage of 600 V and an operating temperature of $\mathrm{T} \approx -20°\mathrm{C}$. The sensor thickness mainly determines the signal height as well as the leakage current. Sensors of the three thicknesses, 200, 240 and 300 µm, were investigated. These sensors were produced by the most likely vendor. The leakage current scales with the fluence as expected, although high fluctuations occur. Therefore a major focus is set on the seed signal and the corresponding annealing behaviour to 60 weeks room temperature equivalent in total, to evaluate the optimal sensor thickness. Within these investigations a difference in neutron and proton irradiation is observed. The particle type dependence is further evaluated with different available strip sensors made of n-type material and at

a higher fluence of $\Phi_{tot} = 6 \cdot 10^{14} n_{eq}/cm^2$. Additional to the pure irradiations, mixed irradiations with $\Phi = 3 \cdot 10^{14} n_{eq}/cm^2$ protons and $\Phi = 3 \cdot 10^{14} n_{eq}/cm^2$ neutrons were performed. Compensation effects, due to an unchanged depletion voltage after the second irradiation, are indicated by the CV characteristics for all n-type materials and the p-type material, if the samples were irradiated with protons after the neutron irradiation. Therefore the signal in mixed irradiation environments is further investigated with these n-type samples.

The second part of this thesis deals with a further evaluation of surface damage and the combination with bulk defects. Using an n-in-p sensor requires a specific interstrip isolation structure. If no isolation structure is implemented, positive oxide charges in the SiO_2 layer attract electrons from the bulk. This leads to the forming of an electron accumulation layer beneath the strips. Therefore the strips are short-circuited and the spatial resolution is lost. On the other hand, an unexpected high interstrip resistance was observed for sensors without any isolation structure after proton irradiation. Simulations have shown a possible mechanism to understand this feature. Bulk damage near the surface creates defects which trap electrons. The resulting electric field prohibits the forming of the electron accumulation layer beneath the strips. To get a better understanding, samples without a specific isolation structure were irradiated with x-rays, neutrons, x-rays and neutrons and pure protons. By investigating the interstrip resistance, possibly occuring compensation effects are visualised.

The thesis starts with an overview of the basic properties of silicon strip sensors followed by some facts about the LHC, CMS and the corresponding upgrades. Insight in the experimental setups available at the Institut für Experimentelle Teilchenphysik (ETP) is given in chapter 4. The results of investigations regarding the signal height of n-in-p silicon strip sensors and further evaluation of some additionally occuring features are presented in chapter 5. Chapter 6 deals with surface damage and the combination with bulk defects. More detailed information regarding investigated sensors and laboratories at ETP can be found in the appendix.

2. Particle Detection with Silicon Sensors

2.1. Electrical Conductivity - Band Model

To describe and understand the electrical conductivity of different materials, usually the band model is used. By describing electrons of a single atom obeying quantum dynamics, it emerges that the electrons are bound in orbitals. The occupation of the energy states follows the Pauli-Fermi exclusion principle which holds that two electrons cannot be in the exact same quantum state, at the same time.

A huge amount of other atoms (in the region of roughly 1 mol[1]) has to be taken into account when a description of the electron quantum states of a macroscopic structure, like a solid, is required. Atoms in solids can form a specific periodic crystal structure so that neighbouring atoms can be represented by a periodic potential which influence the possible energy states of the electrons. Due to the large number of atoms, the amount of possible energy states is also very high and especially dense in some regions, which justify the assumption of a continous *energy band*. Moreover, regions occur where the Pauli-Fermi exclusion principle leads to *forbidden bands*. The states in the energy range of a forbidden band cannot be occupied by any electrons and the energy range is therefore labeled *energy gap*. This leads to a minimal energy which an electron below the forbidden band has to receive, to be able to occupy an energy state above the forbidden band. In this model electrical conduction is possible when an energy band is neither fully occupied nor empty, so that the electrons are mobile.

In figure 2.1 the occupation of energy bands for different materials are shown schemetically. Every rectangle represents an energy band. The band with the highest energy that is already fully occupied at $T = 0\,K$, is called *valence band* and the corresponding energy is the *fermi energy*. The second band is the conduction band. As visible, insulators are materials where the electrons are able to fully occupy the valence band but cannot reach the conduction band, even at a finite temperature. The conduction band is partially occupied for metals as well as for semiconductors at a finite temperature. The partial occupation of an energy band results in electrical conductivity. This is correlated with the band gap E_g which is the energy gap between valence and conduction band. For insulators it is approximately above $4\,eV$. If the band gap is small ($E_g < 0.1\,eV$) enough, that the conduction band is always partly filled with electrons, the material is classified as a metal. Semiconductors are materials with a gap of roughly $4\,eV > E_g > 0.1\,eV$. Semiconductors

[1] 1 mol $\approx 6 \cdot 10^{23}$ particles

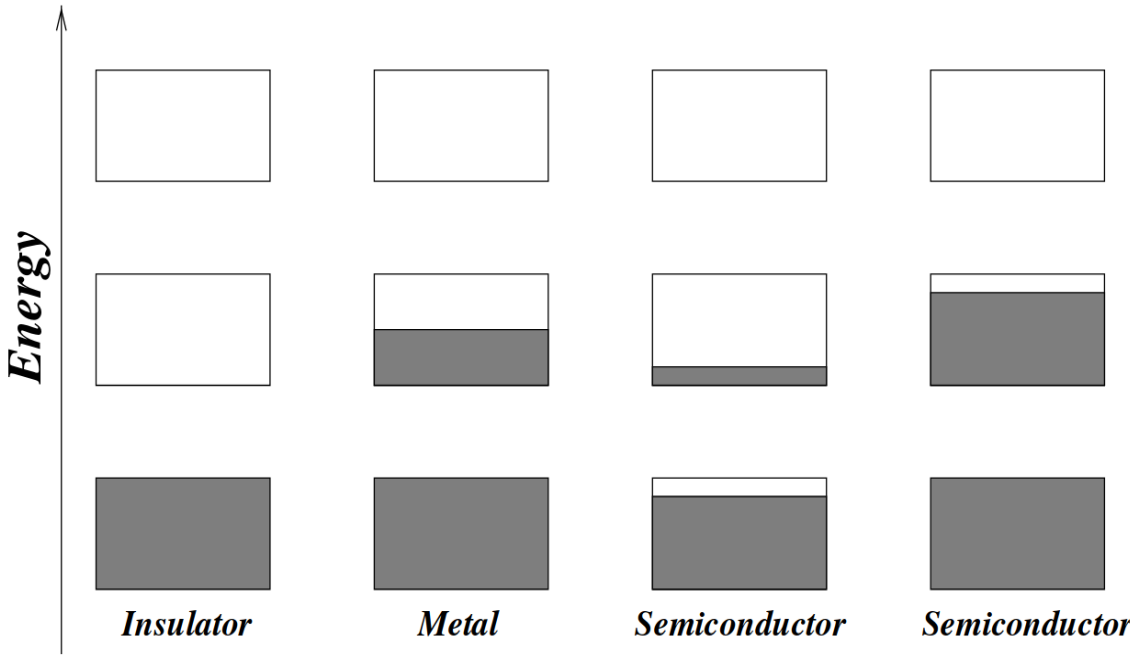

Figure 2.1.: Schematic differences in the occupation of the energy band of insulators, metals and semiconductors [Gal14].

provide electrical conductivity because at finite temperature, electrons of the valence band can reach the conduction band by thermal excitation. The absence of an electron in the crystal structure is represented by *holes* which is marked here by a slight white strip in the valence band. Holes have an effective positive charge. Therefore both, holes and electrons, contribute to the conduction.

2.2. Doping of Semiconductors

Defects are never absent in a crystal structure. Undesired features like grain boundaries and impurities always occur. These additional parameters make the physical description of the properties of a macroscopic structure more complex. However, impurities can be useful for an improvement of the electrical conductivity and are the basis for many technical applications. The artificial introduction of impurities into semiconducting material is called *doping*. Silicon as one of the most important materials for semiconducting electrical components has four valence electrons. With these electrons covalent bonds are formed, which result in four neighbour atoms for every silicon atom in the crystal lattice. If an atom of the third or fifth main group is replacing a silicon atom, the properties in the crystal structure are changing. As an example for an element of the third main group, the behaviour of aluminum inside a silicon crystal is shown in figure 2.2 on the left side. Since the aluminum atom has only three valence electrons, one electron is missing for the usual binding. This missing electron is referred to a hole and contributes to the electrical conductivity, because it leads to effective moving electrons. They fill the binding gap and therefore create other holes which will be filled by other electrons and so on and so forth. Doping with an element which has less valence electrons than the main element forming the crystal is called *p-doping*. The right part of figure 2.2 shows phosphorus as an element of the fifth main group to visualise the counterpart which is called *n-doping*. The fifth electron of the phosphorus atom cannot contribute to any covalent bond and is therefore mobile, behaving like a free charge.

Doping introduces new possible energy levels inside the forbidden band, which leads to an increased electrical conductivity. Since elements, which are used for n-doping, provide

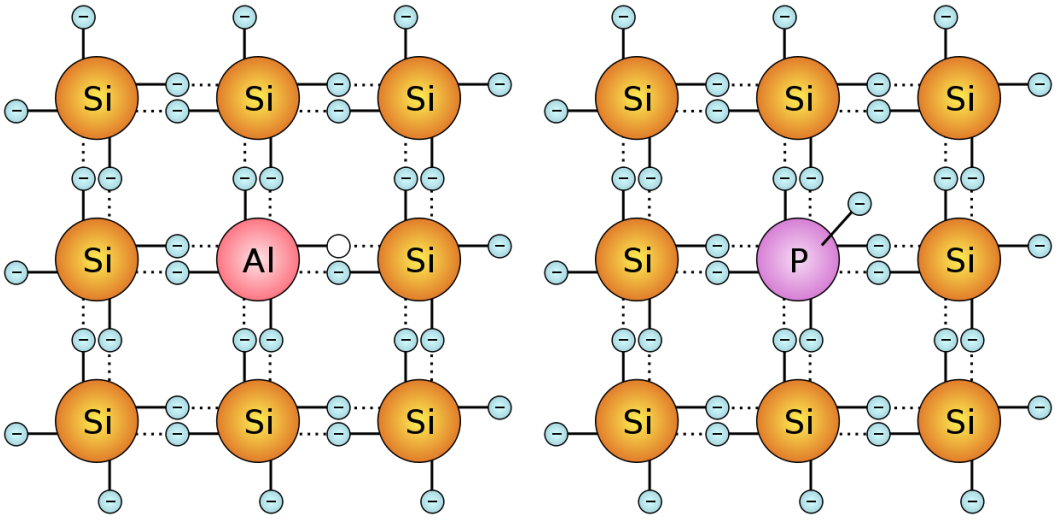

Figure 2.2.: Schematic visualisation of doping in a silicon crystal lattice. The material on the left side is p-doped with aluminum (third main group) and therefore a hole is the free charge carrier. On the right side phosphorus is introduced, which serves one unbound electron and is therefore an electron donator. Doping with phosphorus is an example for n-doping [Hen06a][Hen06b].

electrons, they are called *donors* and introduce corresponding donor levels in the band gap. Those additional energy states are beneath the conduction band. In the case of p-doping the dopants are called *acceptors* due to the fact that the holes can recombine with electrons. Acceptor states are introduced near the valence band.

2.3. Manufacturing of Silicon Wafers

Processing silicon wafers and therefore eventually high-grade sensors is a complex procedure which cannot be completely explained here. However, a basic overview of the different crystal growth methods is given, since materials are classified by the different techniques. The description follows [Har17].

The first method is called *Czochalski* (Cz) process. Silicon is heaten up to temperatures just above the melting point where it stays liquid. A single crystal seed is slowly pulled out of the melt while rotating. This leads to a slow crystalisation resulting in a nearly perfect crystal structure. Homogeneous doping can be done by introducing the dopant materials into the liquid. The process is schematically illustrated in figure 2.3 on the right side. It can be further optimised by using magnetic fields. Therefore it is then labeled *Magnetic Czochalski* (MCz). Since oxygen is abundant in the atmosphere, it diffuses into the material, resulting in an oxygen enrichment.

Another possibility to produce pure silicon material is the *Float Zone* (FZ) technique. A polycrystal silicon rod with a single crystal seed is melted locally with a RF (Radio Frequency) heater. Afterwards the silicon forms a perfect crystal while solidifying. This process is displayed on the left side in figure 2.3. FZ material has an intrinsic low oxygen concentration. However, if a high oxygen concetration is required, it can be added afterwards through diffusion processes. This material is then called *Diffusion Oxygenated Float Zone* (DOFZ) material.

The common way to produce sensors with a certain thickness is *thinning*, where silicon wafer disks are sliced out of the silicon ingot. Afterwards the wafers are ground to the

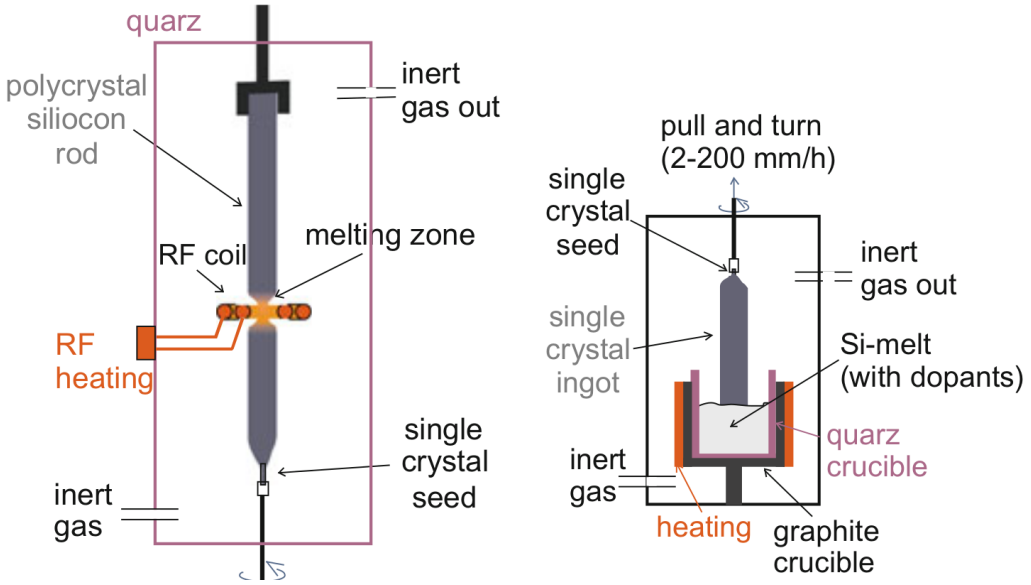

Figure 2.3.: Illustration of the float zone (left) and Czochalski (right) manufacturing of pure silicon ingots. For float zone silicon a polycrystal silicon rod is locally heated up by a RF heater. The liquid silicon crystalises again at the single crystal seed, forming a pure crystal structure. The Czochalski technique uses a liquid silicon bath, from where a single crystal seed is pulled out, while rotating. Silicon solidifies at this seed and forms a monocrystal. [Har17].

desired thickness. However, another technique was developed bei Hamamatsu Photonics K.K.[2]. This technique is called *deep diffusion* since all wafers are cut with the same thickness of 320 µm and a thinner active thickness is achieved by diffusing dopant atoms from a highly doped backplane further into the bulk. The difference between thinned and deep diffused sensors material is illustrated in figure 2.4.

2.4. The pn-Junction

The mechanism of a pn-junction is the basis for important electrical components like diodes and transistors. If a n-doped and a p-doped material is in direct electrical contact to each other, the electrons of the n-type material start to diffuse inside the p-doped material occupying the holes. This process is called recombination.

Since the doped material was neutral before, the area where the diffusion takes place gets electrically charged, as visible in figure 2.5. Therefore this region is called *space charge region*. The left side of the space charge region in the picture is negative because of electrons recombining with holes. The right side is positive due to the absence of electrons. The accumulation of charges results in a build-up of an electric field which mitigates the diffusion force until it vanishes. When the diffusion stops an equilibrium is reached. Electrons in the space charge region now contribute to the electric field but are no free charge carriers anymore, because they are bound in the crystal lattice. Therefore the space charge region is also called *depletion region* (depleted of free charge carriers).

If a pn-junction is biased positivly on the p-doped and negativly on the n-doped side it is operated in *forward* direction. The external electric field supports the diffusion processes of holes and electrons so that a current flow is possible. Biasing the pn-junction in *reverse*, with negative potential on the p-doped side, leads to a larger depletion voltage which is illustrated in figure 2.6.

[2]Hamamatsu Photonics K.K. (HPK, website: [KK])

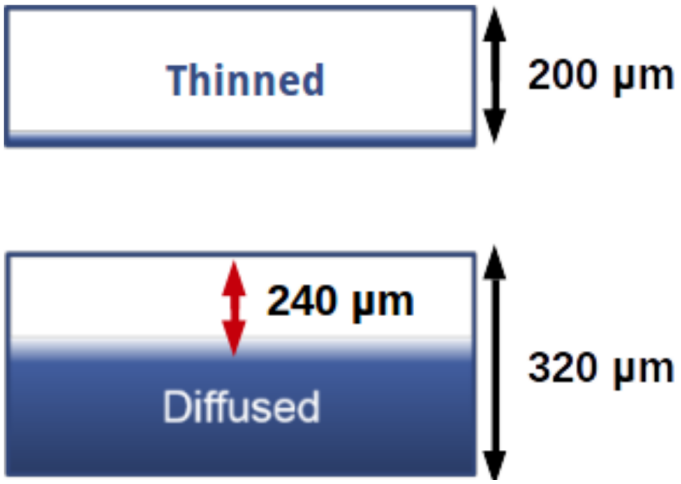

Figure 2.4.: Schmematic visualisation of the difference between thinned and deep diffused material. For deep diffused material the active and physical thickness are not the same. A smaller active thickness is reached by thermally pushing dopant atoms of the backplane further into the bulk.

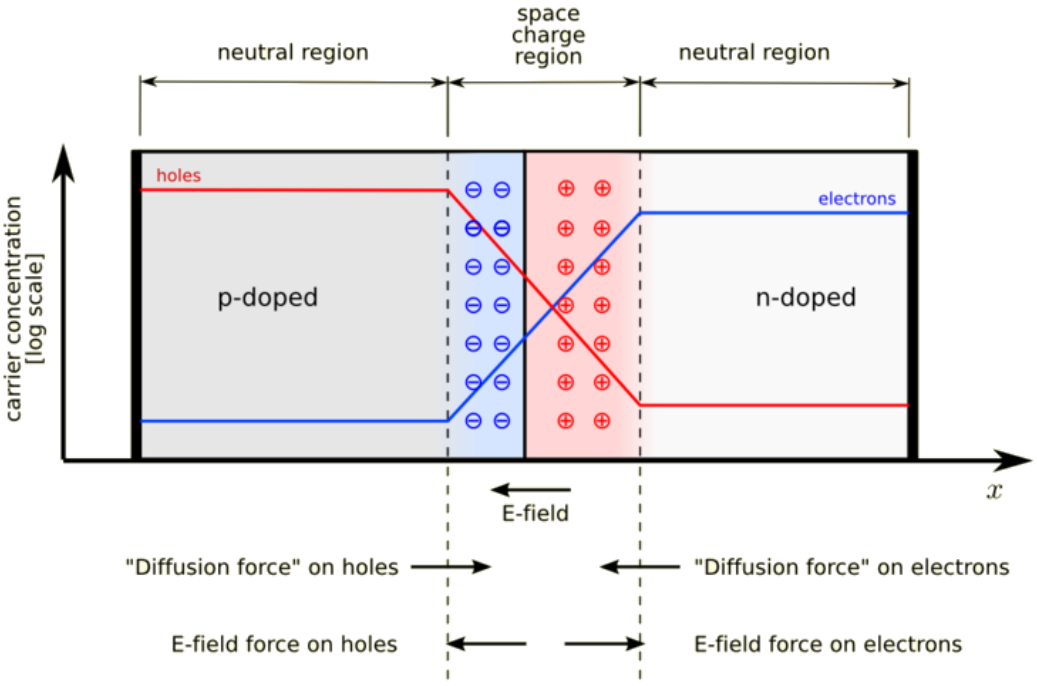

Figure 2.5.: Illustration of a pn-junction. A p-doped material (left side) and a n-doped material (right side) are in direct electrical contact to each other. The electrons in the n-doped material diffuse into the p-doped material and recombine with holes. The holes diffuse into the n-doped material. A space charge region is build-up, which causes an electric field that mitigate the diffusion till an equilibrium is reached [The07].

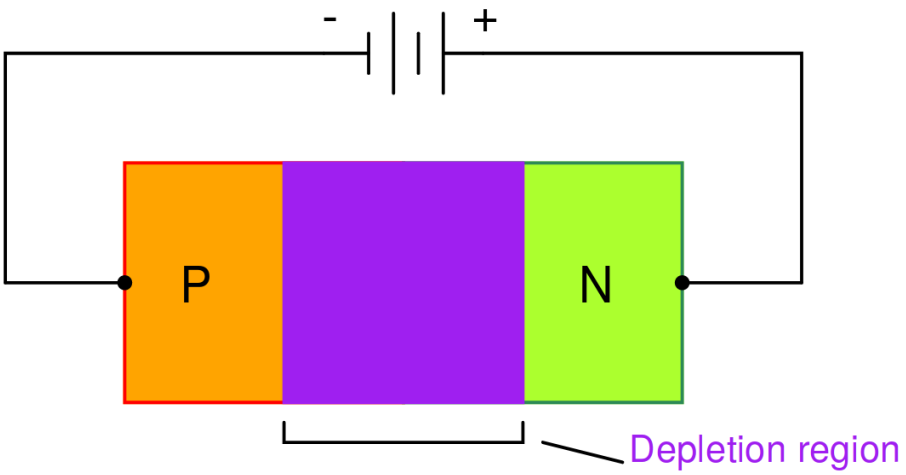

Figure 2.6.: Schematic visualisation of a pn-junction in reverse bias. The depletion region grows because electrons in the n-doped material directly move into the electrode. On the side of the p-doped material holes move into the electrode so that the depleted zone gets larger on both sides [Kup09].

2.5. Interaction of Particles in Matter

When a particle crosses a medium, a large amount of interactions are possible. For a complete description all cross sections for every single interaction (which are again dependent on different parameters like energy or charge) have to be taken into account. Therefore this section is only focused on heavy charged particles and light ionising particles like electrons and photons which are important for irradiation studies of silicon devices.

Heavy Charged Particles

The mean energy loss of heavy charged particles in matter can be described by the *Bethe equation*.

$$-\left\langle \frac{\mathrm{d}E}{\mathrm{d}x} \right\rangle = \mathrm{K}z^2 \frac{Z}{A}\frac{1}{\beta^2}\left[\frac{1}{2}\ln\left(\frac{2m_e c^2\beta^2\gamma^2 T_{\max}}{I^2}\right) - \beta^2 - \frac{\delta(\beta\gamma)}{2}\right] \tag{2.1}$$

The constant K is a compound of physical constants. Further included constants are the electron mass m_e and the speed of light c. As indicated in (2.1) the bethe equation is dependent on the charge of the incoming particle z, the atomic number of the matter Z, the velocity in natural units β, the lorentz factor γ, the mean excitation energy I, the density-effect corretion $\delta(\beta\gamma)$ and the maximum transfered kinetic energy $T_{\max}$. It is valid within a few percentage in the region of $0.1 \leq \beta\gamma \leq 1000$ [Tan+18].

The stopping power of a muon in copper, calculated by the bethe equation in its valid range, is illustrated in figure 2.7. In the range of $\beta\gamma \leq 0.1$ the bethe equation has to be corrected by nuclear losses. Radiative losses like bremsstrahlung affecting the stopping power stronger than ionisating losses at higher range.

The energy loss of charged particles in silicon sensors results in the generation of electron-hole-pairs which can be seperated by an electric field. Therefore the induced field due to the drift of electrons creates a signal. For a silicon sensor of a finite thickness it has to be taken into account that the probability of depositing a certain energy is statistically distributed.

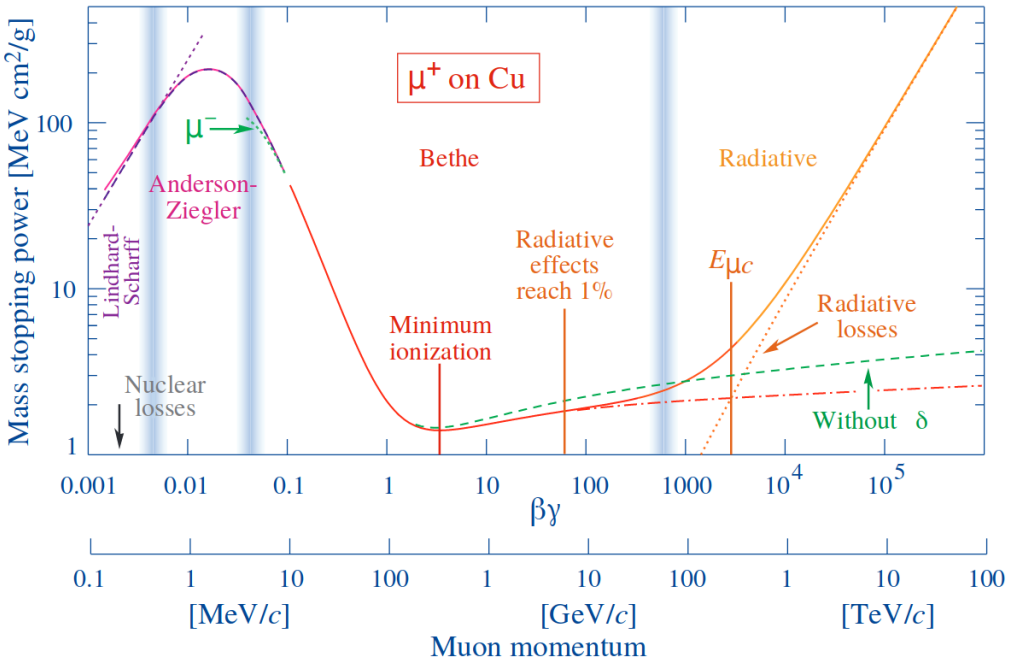

Figure 2.7.: Examplary visualisation of the stopping power of a muon in copper. It is calculated with the bethe equation in its valid range of $0.1 \leq \beta\gamma \leq 1000$. For low energies nuclear losses become more important and for higher energies radiative losses through bremsstrahlung getting dominant [Tan+18].

The energy loss probability distribution $f(\Delta/x)$ (dependent on energy loss Δ and thickness x) is not gaussian shaped due to the possibility of depositing a high amount of energy on δ-electrons. In figure 2.8 the dependency of the energy loss probability distribution on Δ/x is visualised. The corresponding functions are called straggling functions. It is also visible that the mean energy loss is higher than the *most probable value* (MPV). This is caused by the tail to high energies and leads to the fact that approximately 90% of the collisions result in an energy loss below the mean. In a gaussian statistical behaviour this would have been 50%. Regarding a silicon sensor, this effect leads to a corrected most probable electron-hole-pair generation of approximately 30% less than expected by the mean value [Tan+18][Har17].

Electrons and Photons

The Bethe equation is not sufficient for electron and photon interactions, because it does not take bremsstrahlung into account which is dominating at high energies. Due to the Pauli-Fermi exclusion principle, the spin of the electron leads to a correction of the cross sections, since the most frequent interactions are with shell electrons. For photons the Bethe equation is not valid, because they have neither mass nor charge.

The most important sources of energy loss for electrons in lead are illustrated in figure 2.9. Bremsstrahlung leads to the most significant energy deposit in matter especially at high energies. For intermediate energies with $\beta\gamma \approx 3 - 4$, electrons behave like MIPs[3]. While traversing a medium, MIPs lose a minimal amount of energy so that these particles are able to surrive over long distances within a medium [Ber+17]. Therefore electrons, emitted by a ^{90}Sr source, are used to mimic MIPs, which generate electron-hole-pairs and therefore signal over the whole sensor.

[3]MIP = Minimum Ionising Particle

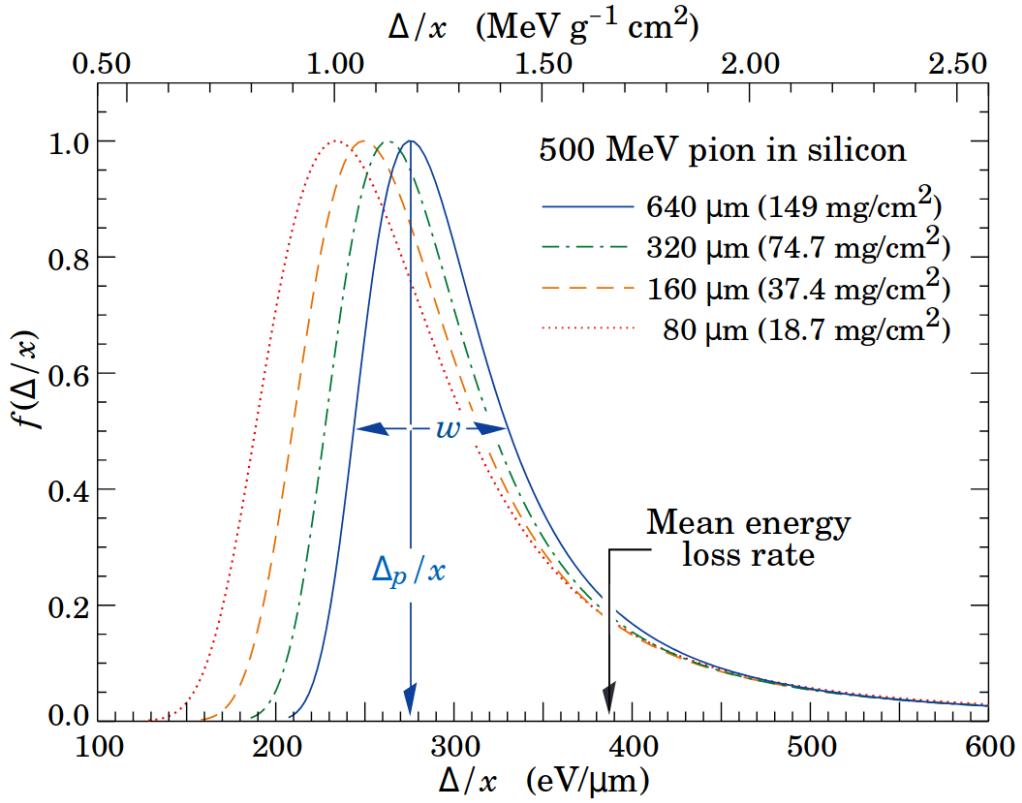

Figure 2.8.: Straggling functions of 500 MeV pions in silicon. The most probable value is approximately 1/3 less than the mean energy loss rate. This shift is caused by the tail towards high energies. The dependency on the thickness is visualised by different line styles and colours [Tan+18].

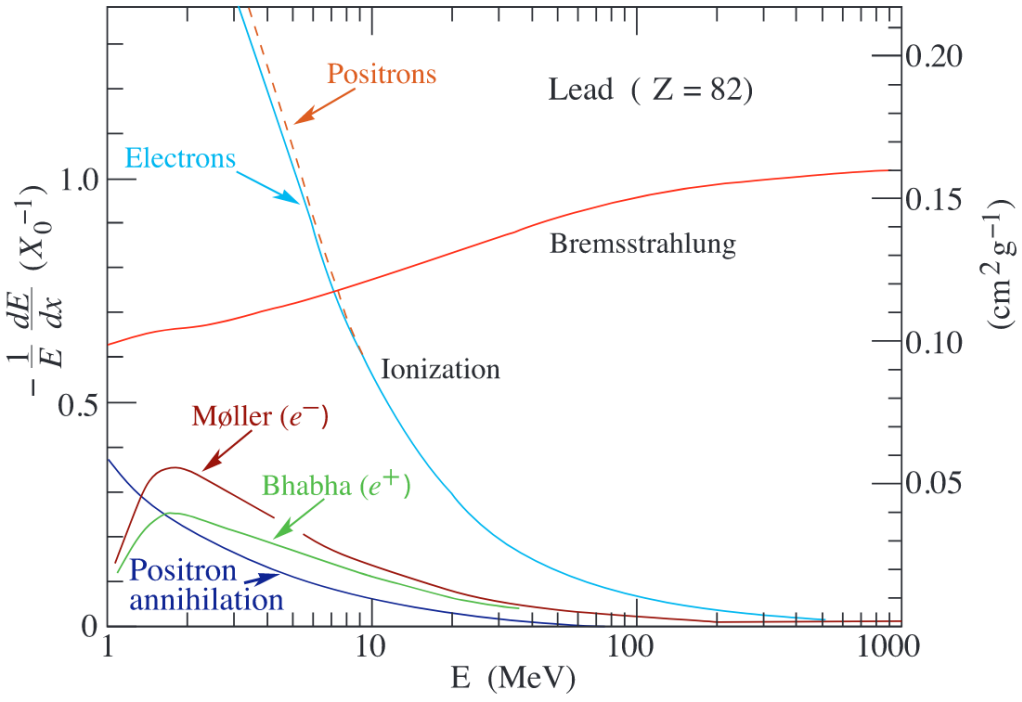

Figure 2.9.: Illustration of the energy loss of electrons and positrons in lead. In the lower energy region ionisation is the main interaction type, but also Bhabha- (positrons) and Møller-scattering (electrons) take place. For higher energies, above 10 MeV, bremsstrahlung gets dominant over ionisation [Oli+14].

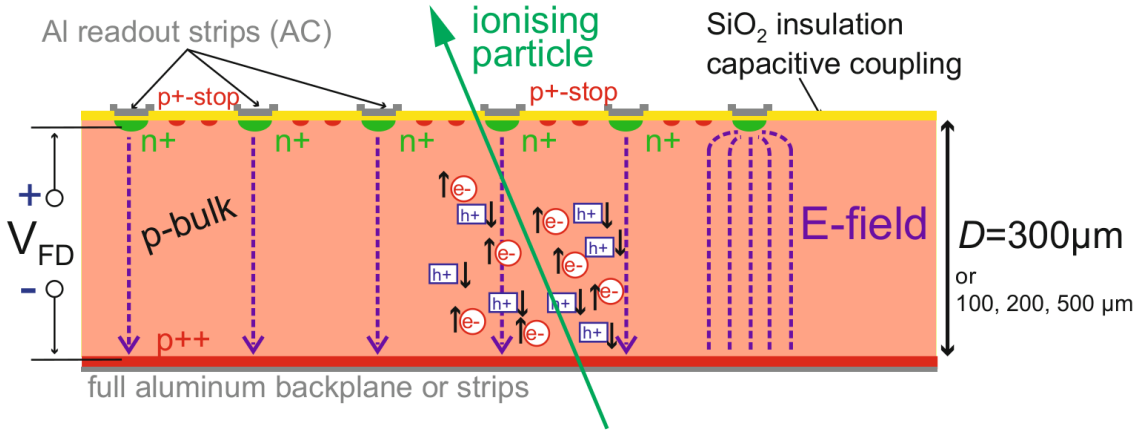

Figure 2.10.: Schematic visiualisation of the signal generation in a n-in-p silicon strip sensor, by a crossing ionising particle. A reversed bias of the full depletion voltage is applied to sufficiently operate the sensor. The ionising particle creates electrons (holes) inside the bulk which are then accelerated towards the strips (backplane). Through induction a signal is generated inside the strips [Har17].

When a photon interacts with matter three main mechanisms take place, where the strength is energy dependent. The mechanisms are pair production (above roughly 1 MeV), compton scattering and ionisation. At even higher energies the fragmentation in electromagnetic cascades has to be taken into account additionally.

2.6. Working Principle of Silicon Strip Sensors

The amount of free charge carriers in a silicon sensor of a standard size is in the region of 10^9. However, only $2 \cdot 10^4$ electrons are induced by an ionising particle crossing the sensor. To prohibit that a signal is superposed by noise, either the sensor has to be cooled down to a technically not feasible degree, or free charge carriers have to be removed by using a pn-junction in reverse bias [Har17].

To fully deplete a pn-junction of a certain thickness D and resistivity ρ a voltage of

$$V_{\mathrm{FD}} = \frac{D^2}{2\epsilon\mu\rho} \tag{2.2}$$

is required. The constants are the mobility of charge carriers μ and the permittivity $\epsilon = \epsilon_0 \cdot \epsilon_{\mathrm{Si}}$. The full depletion voltage is the minimum voltage the sensor should be operated with. Furthermore a high electric field for a fast readout and a sufficient signal height is required. Sources of uncertainities have to be taken into account, for example the noise of the readout electronics, which decrease the significance of the signal. Therefore the sensor should be operated above the depletion voltage V_{FD}.

A strip sensor is basically a compound of many pn-junctions next to each other. Figure 2.10 is a schematic illustration of the signal generation in an n-in-p silicon strip sensor. On the upper side aluminum (Al) strips are located over n^{++} implants[4]. At the bottom of the main p-bulk a thin p^{++}-layer is placed over the aluminum backplane.

[4]The notation $\mathrm{n/p}^+$ is referred to a high doping concentration and not to charges

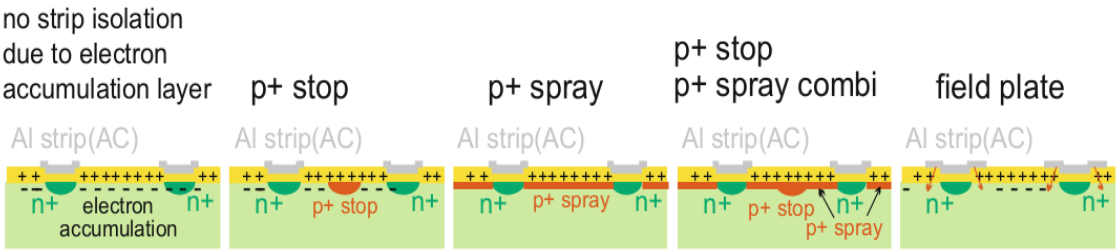

Figure 2.11.: Schematic illustration of how an electron accumulation layer between the strips is formed and how to prohibit it with p-doped implantants or a field plate. The accumulation layer is formed due to impurities in the SiO_2 layer which can be represented by positive oxide charges. Those attracted electrons form the electron accumulation and short-circuit the strips [Har17].

2.6.1. Interstrip Insulation

In principle the use of a n-type bulk and p-doped strips (p-in-n) is also possible. There are differences in the radiation hardness, which will be discussed in the next section. Impurities lead to positive charges inside the SiO_2 surface of silicon sensors. These charges attract electrons from the bulk resulting in an electron accumulation layer beneath the strips. This leads to a short-circuit between n^{++} strips so that the interstrip resistance and therefore spatial resolution as well as signal efficiency would be lost. A p-implant between the strips is implemented to prevent the formation of an accumulation layer. In figure 2.11 three realisations of implants are displayed. This issue is not occuring for p-in-n sensors.

2.6.2. p-Type Strip Sensor Design

A sketch of the general structure of a silicon strip sensor is presented in figure 2.12. The aluminum strips are coupled to the bias ring and further surrounded by the guard ring and the edge implant. Beneath the aluminum strips, isolated by a SiO_2 layer, highly doped n-type strip implants are introduced in the p-type bulk. This capacitive readout of the strips over the *Alternating Current* (AC) pads prevents the leakage current in every strip from being amplified in direct coupling. The operating voltage is applied through the aluminum backplane, where a p^{++} layer is prohibiting a schottky barrier. The bias ring is used to ground the sensor. Current can flow through the *Direct Current* (DC) pads and the polysilicon resistor (marked in white) to the bias ring. Contrary to the AC pads, the DC-pads are directly connected to the strip implants. The passivation layer on top of the sensor surface provides openings for electrical contacting. A usually floating guard ring and a highly p-doped edge structure is implemented to provide a shaped electric field with minimised edge effects.

2.7. Irradiation of Silicon Strip Sensors

Surface Damage

By describing the effects of irradiation in a strip sensor, it has to be differed between surface and bulk damage. The term *surface* of a sensor mainly refers to the SiO_2 layer on top of the sensor and between the strips. In SiO_2 the mobility of electrons ($20\,cm^2/(Vs)^{-1}$) exceeds the mobility of holes by six orders of magnitudes ($2 \cdot 10^{-5}$ $cm^2/(Vs)^{-1}$) [Har17]. When an ionising particle crosses the devices, it creates electron-hole-pairs in the bulk as well as in the surface. Since electrons are approximately 1 000 000 times more mobile than holes, they reach the electrodes comparably faster. The holes can be trapped inside the surface, leading to an effective positive oxide charge. This positive charge attracts electrons of the bulk which are then forming an electron accumulation layer.

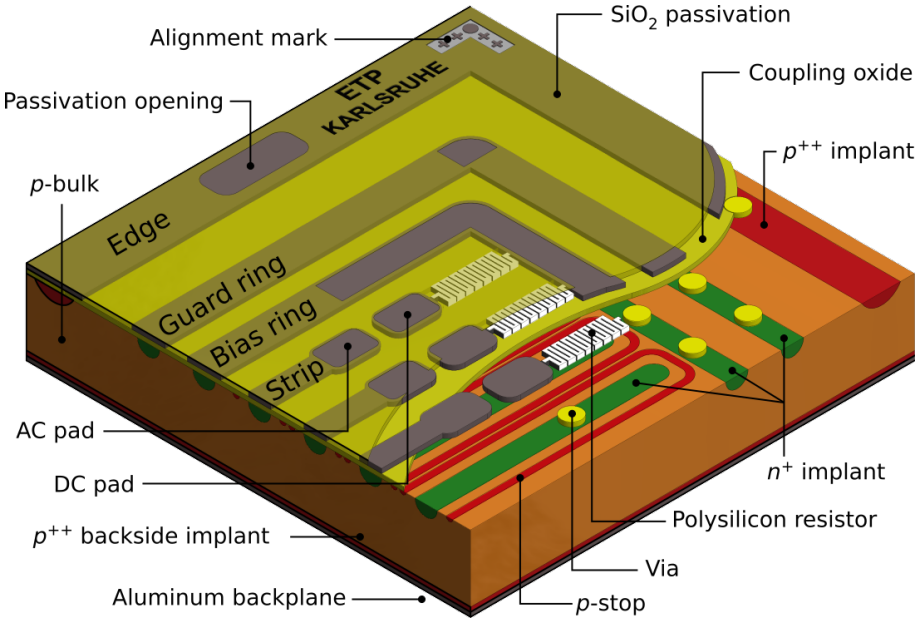

Figure 2.12.: Silicon strip sensor design for Phase-2 of CMS. Marked in green are the n-doped implants in a p-type bulk. To prevent leakage current from amplifying, the signal readout over the aluminum strips is capacitive, through an insulating layer of SiO_2. The DC- and AC-pads are used for probing and therefore uncovered from any passivation. The operating voltage is applied over the backplane, wherefore the bias ring has to be grounded. Outer structures are shapening the electric field and defining the active detector volume.

Bulk Damage

A normalised quantity is required to compare irradiations and their effects of different particle types. Following the NIEL (*Non Ionising Energy Loss*) hypothesis, the damage of all particles can be rescaled by a hardness factor κ.

This factor is dependent on the displacement damage cross section $D(E)$ and the energy spectra $\Phi(E)$

$$\kappa = \frac{\int D(E)\Phi(E)\mathrm{d}E}{D(n) \cdot \int \Phi(E)\mathrm{d}E} \quad . \tag{2.3}$$

The *fluence* can then be calculated by

$$\Phi_{\mathrm{eq}} = \kappa\Phi = \kappa \int \Phi(E)\mathrm{d}E \quad , \tag{2.4}$$

which is the particle flux per area scaled by a specific factor and normalised to 1 MeV neutron equivalent.

The displacement damage cross section is plotted over the particle energy for different particles in figure 2.13 . Some lattice defects due to displacement are presented in figure 2.14. Vacancies are empty places in the lattice. Their counterpart is called interstitial and

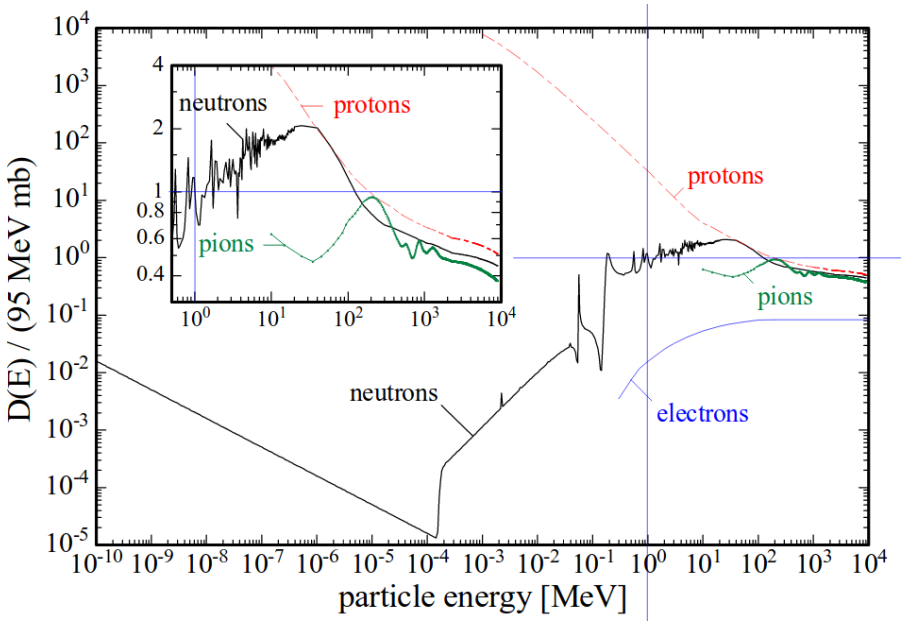

Figure 2.13.: Displacement damage cross section dependency on the particle energy for different particles, following the NIEL hypothesis [Fre+02].

the combination of both is called frenkel pair. It is also possible that due to irradiation, defects interact with impurities like carbon or oxygen. Therefore further defects can be formed.

The defects illustrated in figure 2.14 are mainly caused by a small energy deposit of charged particles due to coulomb force. If a neutral particle interacts with an atom via strong force, an atom will be knocked out of the lattice (therefore called *Primary Knock on Atom*). This atom is receiving high momentum and pushing further atoms out of their position, which is called *clustering*.

Figure 2.15 shows the difference between charged and neutral particles interacting with a silicon lattice. The fluence for all simulations is about $\Phi = 10^{14} \mathrm{n_{eq}/cm^2}$. The amount and position of vacancies was simulated with 1 MeV protons on the left side, 24 GeV protons in the middle and 1 MeV neutrons on the right side.

A huge amount of point vacancies occur, distributed homogeneously all over the volume for the comparably low energy protons. At higher energies there are still some point defects but the ratio of cluster defects to vacancies increases. If the crossing particle is uncharged, cluster defects dominate over point defects.

2.7.1. Irradiation Effects on Sensor Properties

The irradiation defects result in additional levels in the energy gap of silicon in the band scheme. Dependent on the type and position of the generated state inside the energy gap, effects on the sensor properties occur, which are illustrated in figure 2.16. The first three effects in the picture can be discribed by the Shockley-Read Hall statistics [SR52].

Energy levels in the midgap result in a higher probability for the electrons of the valence band to reach the conduction band and therefore create higher current flow. Introducing new donor or acceptor states near the energy edges change the space charge. This leads to a higher depletion and therefore operating voltage. Electrons or holes can temporarily occupy states within the band gap from which they are released after a certain amount of time. This mechanism is called trapping. As a result the charge collection efficiency

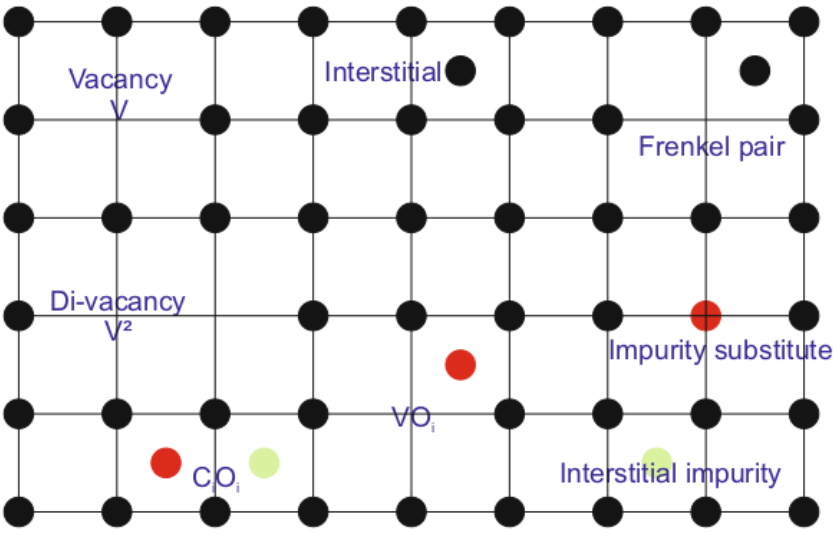

Figure 2.14.: Illustration of effects which can occur in the silicon lattice due to irradiation. There are also defects where the silicon react with impurities, or the impurities itself change their position in the lattice. This defects lead to a creation of new levels in the energy band scheme, visualised in figure 2.16. Impurities are labeled with their element symbol [Har17].

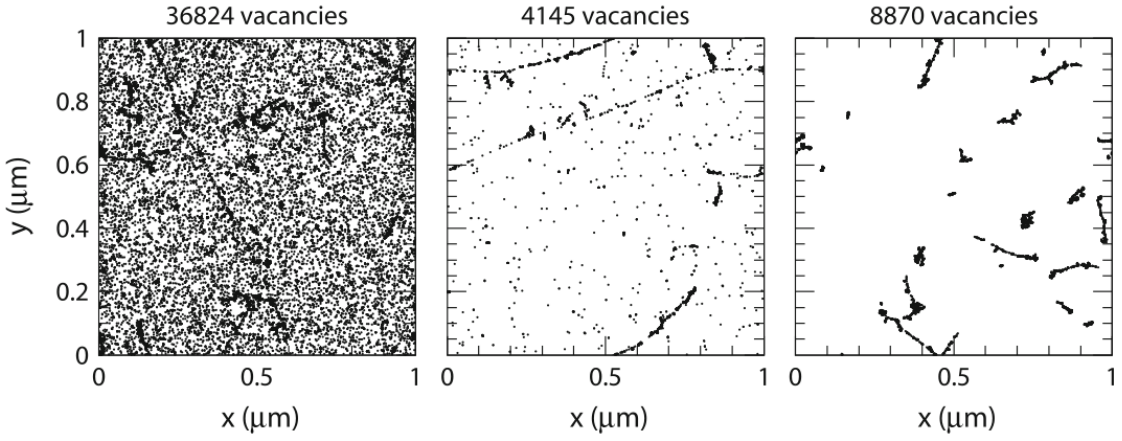

Figure 2.15.: Simulation of the vacancy distribution in a silicon device, caused by different particles. On the left side the material was irradiated with 10 MeV protons, which introduces a large amount of vancancies all over the material volume. The picture in the middle shows the vacancy generation with protons of 24 GeV. They still cause some point defects but the cluster to point defect ratio is a lot higher. Finally, in the last figure neutrons with an energy of 1 MeV were simulated. Since neutrons cannot interact electromagnetically, cluster defects predominate [Huh02].

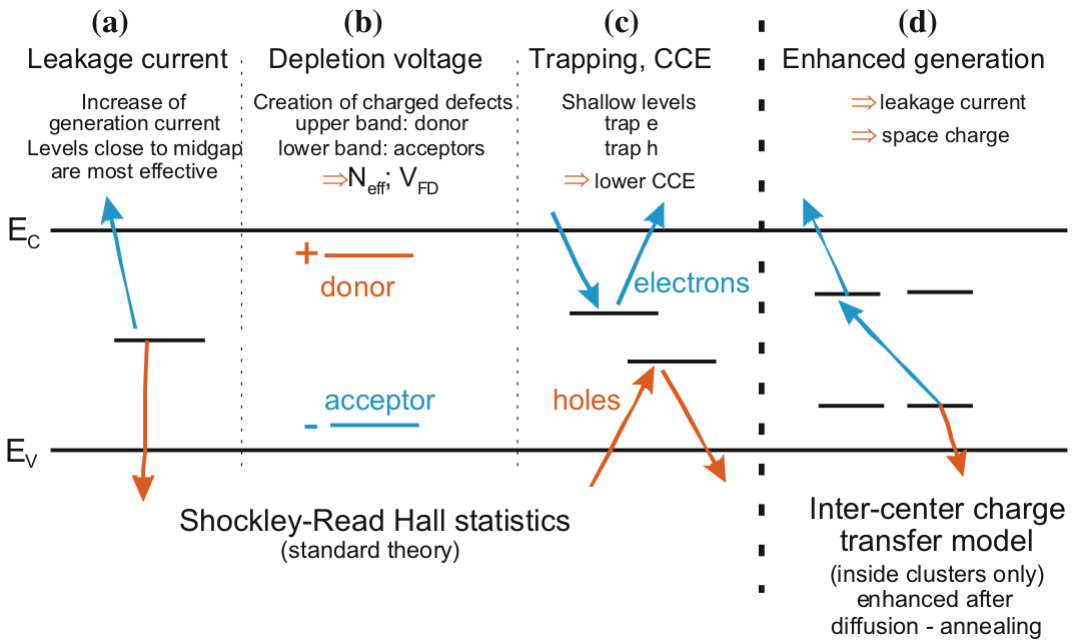

Figure 2.16.: Irradiation causes new levels in the energy gap of silicon in the band model. The according effects are displayed. New energy states in the middle of the band gap cause a higher leakage current. Donor and acceptor states affect the space charge and therefore depletion voltage. If an electron or hole gets trapped inside a deep level and later released again, it still cannot contribute to the signal since the de-trapping time is usually longer than the readout time. Therefore the signal (charge collection) decreases. The first three defects are well described by the Shockley-Read Hall statistic (see [SR52]). The enhanced generation is an additional combination of defects in clusters [Har17].

(signal) decreases, because trapped charge carriers cannot contribute to the signal. When the trapped charges are realeased the readout time of the electronics is already elapsed. The fourth example in the figure (enhanced generation) represents a mixture of new introduced levels. It is only relevant for clusters and causes a higher leakage current as well as depletion voltage.

Leakage Current

Due to the introduction of additional energy states inside the band gap of silicon, the leakage current I increases. A sensitive volume V of the detector is confined by the guard ring. The leakage current scales linearly with the fluence Φ_{eq} and the volume as indicated by equation 2.5. It is convenient to calculate the current density I/V and plot its dependence on the fluence. The slope α is referred to as current related *damage rate* and is a useful parameter to monitore the irradiation accuracy, because it is independent of the particle or sensor type [Col99]. This linear scaling for different materials is displayed in figure 2.17.

$$\frac{I}{V} = \alpha \cdot \Phi_{\text{eq}} \tag{2.5}$$

The leakage current scales also with temperature. If the temperature increases, the probability of electrons reaching the conduction band increases. The dependence is shown in

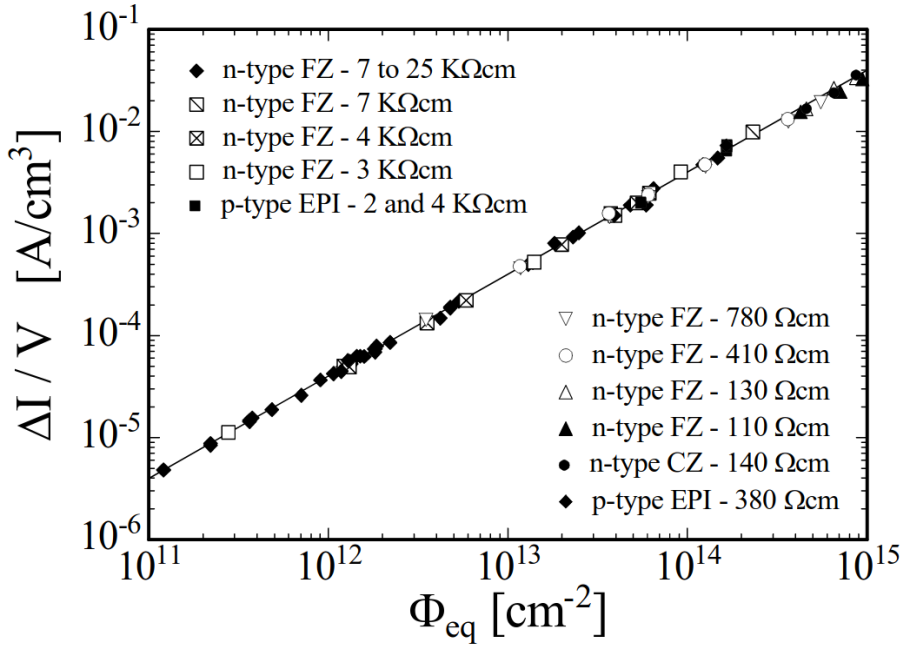

Figure 2.17.: Leakage current normalised on the volume over fluence. The linear scaling is independent of material or particle type. The slope α is called damage rate and is a useful tool to verify the fluence after irradiation procedures [Fre+02].

equation 2.6 with different energy levels like band energy and trap level energy summarised as effective energy E_{Eff} (1.21 eV [Chi13]) and the Boltzmann constant k_B

$$I(T) \propto T^2 \cdot \exp\left(-\frac{E_{\text{Eff}}}{2k_B T}\right) \quad . \tag{2.6}$$

The power consumption is scaling linearly with the leakage current as well as the bias voltage. Therefore this circular dependency of leakage current and temperature can result in a state that is called thermal runaway. Cooling down to -10°C reduces the current already by a factor of 20 [Col99].

Annealing

At low temperatures, for example below 0°C, crystal structures are usually frozen. At finite temperature a crystal structure can generally change. For this temperatures, atoms in the crystal lattice can alter their position, which is called *annealing*. The removal of crystal defects is called *beneficial annealing*, where the term *annealing* refers to the change of properties due to a certain temperature and time. The counterpart *reverse annealing* occurs after a rather long time of annealing for silicon sensors. It is mainly caused by the generation of acceptor levels. Annealing leads to a decrease in the leakage current. This is visualised in figure 2.18 for different temperatures and annealing times.

Charge Collection

As already indicated in figure 2.16, irradiation introduces shallow levels in the band gap, which are ionised at operation temperatures. These charge carriers cannot contribute to the signal anymore, wherefore the signal heigth decreases. Crucial for particle detection is a sufficient electric field which can accelerate charge carriers all over the detector. The

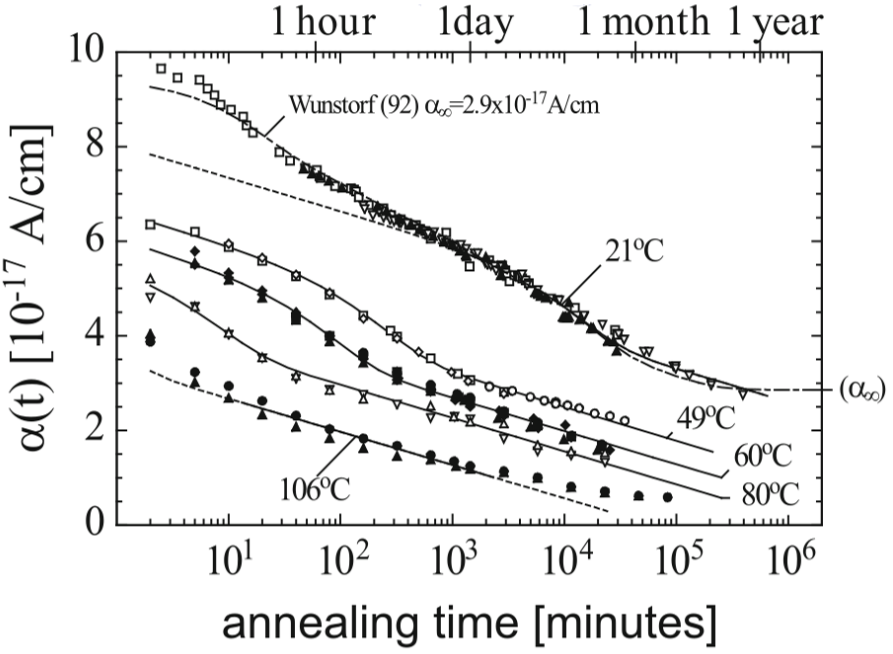

Figure 2.18.: Damage Rate as a representative of the leakage current over annealing time at different temperatures [Wun92].

effective doping concetration N_{eff} increases with fluence, which leads to an increase of the depletion voltage.

$$V_{\text{FD}} = \text{K} \cdot |N_{\text{eff}}|\, d^2 \tag{2.7}$$

The depletion voltage is dependent on a constant K, which basically consist of the electric permittivities, the effective doping concentration N_{eff} and the thickness d. Formular 2.7 also implies that the depletion voltage is expected to be significantly higher for thicker sensors. If the operating voltage does not exceed the depletion voltage, the electric field would not cover the whole detector volume. Electrons and holes, generated by a MIP in a region where the sensor is not depleted will be lost [Col99]. Moreover, the trapping probability of generated charge carriers increases with higher fluences. With the same operating voltage and therefore acceleration of the charges, still less charge will be accumulated at the strips due to the decreased effective lifetime. Therefore the charge collection decreases with increasing fluences.

Capacitance

For the capacitance of a sensor, the sensor can be approximated by a plate capacitor with the strips as one plate and the backside as the other. The corresponding formula of a plate capacitor is given by

$$C = \epsilon_0 \epsilon_{\text{Si}} \frac{A}{d} \qquad , \tag{2.8}$$

with the electric permittivities of vacuum and silicon ϵ_0 and ϵ_{Si}, the area of the plates A and the distance between the plates d. Although the plate capacitor formula is not valid

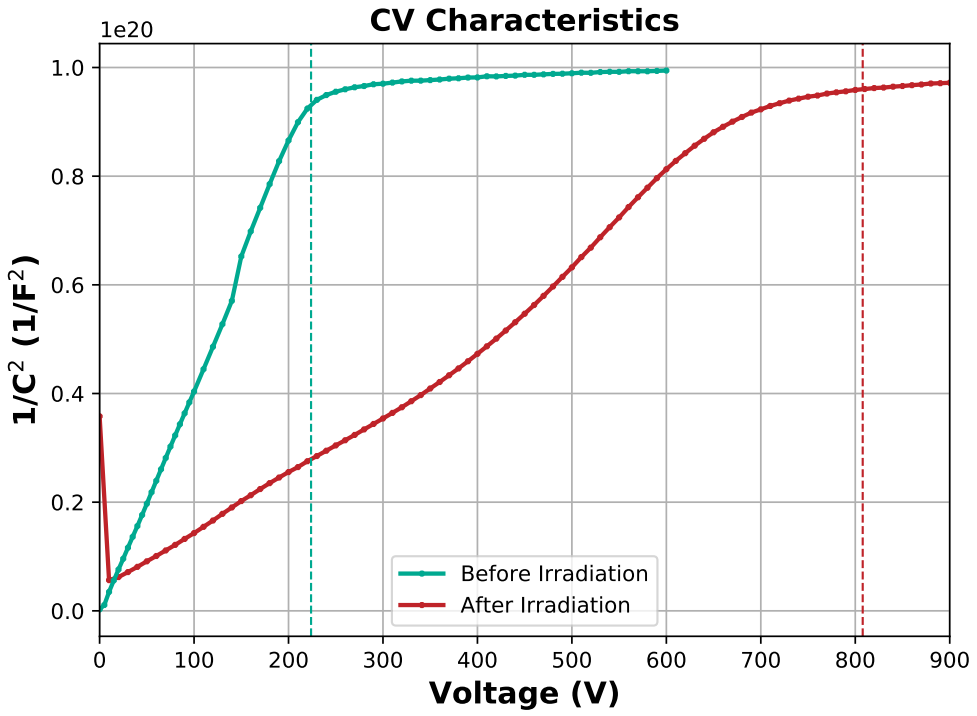

Figure 2.19.: Estimation of the depletion voltage by plotting $1/C^2$ over the voltage. The kink indicates the point where the sensor is fully depleted. At even higher voltage the capacitance and therefore $1/C^2$ stays constant. It is visualised, by the dashed lines, how the depletion voltage changes after irradiation of $\Phi = 3 \cdot 10^{14} \mathrm{n_{eq}/cm^2}$ with neutrons.

for sensors, the scaling with the area and inverse thickness is valid. As stated in section 2.6 (equation 2.2), the full depletion voltage V_{FD} is dependent on the thickness d. This leads to an expression for the thickness propotional to the square root of the bias voltage (2.9), which is valid for $V_{\mathrm{bias}} \leq V_{\mathrm{FD}}$.

$$C = A \cdot \sqrt{\frac{\epsilon_0 \epsilon_{\mathrm{Si}}}{2\rho\mu V_{\mathrm{bias}}}} \tag{2.9}$$

When the full depletion is reached so that the full width of the detector is depleted, the depletion zone and therefore the capacitance cannot grow anymore and is constant for $V_{bias} > V_{FD}$. This dependency of the capacitance on the bias voltage can be used to identify the full depletion voltage.

The term 2.19 $1/C^2$ is plotted over V in figure 2.19. The kink shows where the sensor is fully depleted and the capacitance becomes constant. The dashed lines indicate the corresponding depletion voltage of $V_{\mathrm{FD}} \approx 220\,\mathrm{V}$ before and $V_{\mathrm{FD}} \approx 810\,\mathrm{V}$ after $\Phi = 3 \cdot 10^{14} \mathrm{n_{eq}/cm^2}$ neutron irradiation.

Strip Parameters Affected by Irradiation

Insulated strips and low noise are crucial for the detection of charged particles with a specific spatial resolution. The *interstrip resistance* R_{int} is an indicator for the interstrip insulation. It should be roughly 100 times higher than the resistance of the polyresistor to provide a sufficient isolation structure between the strips. Measuring the interstrip

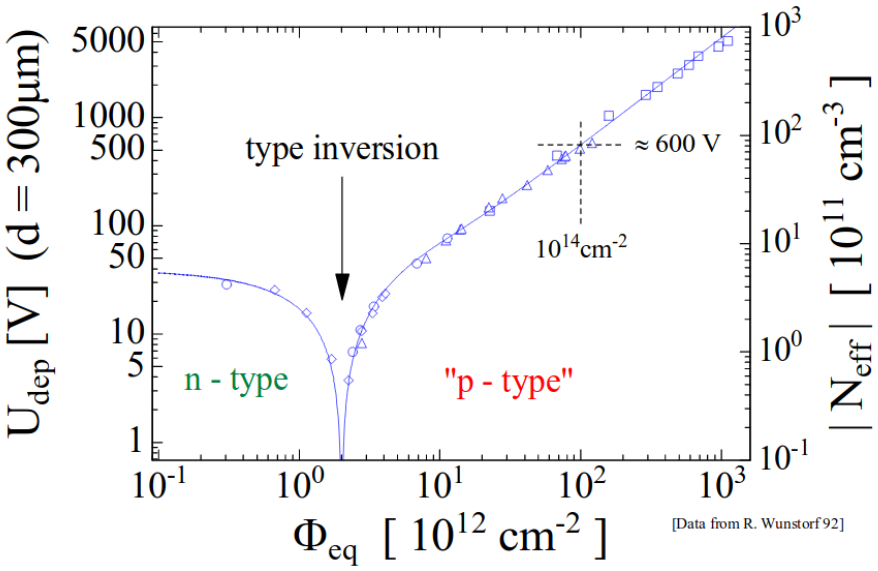

Figure 2.20.: Type inversion of n-type sensors. Donors are constantly getting removed in an irradiation environment. Additional acceptors are also generated by irradiation. After a fluence of roughly 10^{12}cm^{-2} the n-type bulk becomes a p-type bulk. The operating voltage sign stays unchanged, because the p-type doping concentration in the strips is still considerably above the effective space charge density in the bulk [Fre+02].

resistance is performed by placing two needles on the DC pads of two neighbouring strips, while grounding the sensor with a bias needle. The same configuration can be used to measure the *interstrip capacitance*. The interstrip capacitance C_{int} is not expected to change due to irradiation.

As a result of the general introduction of midgap energy levels and the increasing leakage current the *strip leakage current* also increases. It can be determined by contacting the DC pad and the bias ring and measuring the current flow. Because the leakage current is basically composed of the strip leakage currents of all strips together, this can be calculated and used as a consistence verification.

2.7.2. Differences of n-in-p and p-in-n Sensors

Beside the fact that for n-in-p sensors usually a specific interstrip insulation structure is required, regarding irradiation other differences between n-in-p and p-in-n sensors occur. As displayed in figure 2.20 the type of the n-bulk changes for fluences above $\Phi \approx 10^{12}\text{cm}^{-2}$ due to the constant donor removal and acceptor creation. The appropriate term is *type inversion*. Although the type of the bulk is changed from n-type to p-type the sign of the bias voltage stays the same, as well as the readout mechanism, because the strips implants are still higher doped than the bulk.

Regarding the signal height there is also another difference between the two materials. In a p-type sensors electrons are the charge carriers which are accelerated to the strips and holes for n-type sensors. Since the mobility of electrons in the silicon device is higher than the mobility of holes, the probability of being trapped is less. In figure 2.21 the seed signal in electrons, which is the signal of one strip, is plotted over the fluence for n-type and p-type sensor bulks. The signal of the n-type material, marked in green, generally decreases faster with fluence, than the p-type material, marked in purple. Hence, for irradiation environments where high fluences are expected, p-type material (n-in-p) is superior.

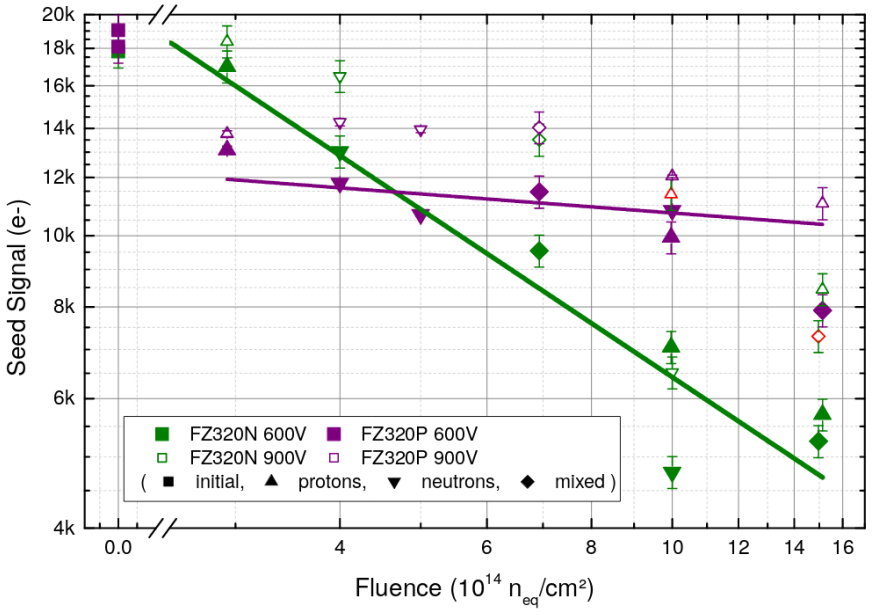

Figure 2.21.: Comparison of the seed signal of n-type (green) and p-type (purple) material. The material with a p-type bulk and n^+-strips performs better for high fluences independent of the particle type or operating voltage [Die13].

3. LHC and the CMS Phase-2 Upgrade

3.1. The LHC at CERN

One of the largest and most commonly known experiments in physics is the circular particle accelerator *Large Hadron Collider* LHC at CERN[1] in Geneva. The particles, which are energetic enough to almost reach the speed of light, are brought to collisions. Detectors were built to study the reactions happening in the vertex.

An overview of the accelerator and its detectors is displayed in figure 3.1. The acceleration of protons, ending up in a collision in one of the yellow spots (CMS, ALICE, ATLAS or LHCb), is briefly explained in the following. First of all, the isolation of protons is achieved by separating the electron of a hydrogen atom from its nucleus. The protons are then accelerated to 50 MeV in the LINAC2 and injected into the BOOSTER. Before getting injected into the PS, the protons reach an energy of 1.4 GeV. Inside the PS they are accelerated to 25 GeV. They are further accelerated by the SPS where the energy increases to 450 GeV. Finally, the protons reach the nominal energy of 6.5 TeV after 20 minutes of accelerating in the LHC. Before the protons are led to a collision, they can be conserved over many hours inside the LHC [Lop17].

The announcement of the discovery of a Higgs-like particle in July 2012 was one of the greatest achievements at CERN [CER]. A candidate for such a Higgs-like event, recorded with the CMS experiment (see section 3.3) is displayed in figure 3.2. The proton-proton collision had a centre of mass energy of 8 TeV and led to the production of a Higgs boson, which decayed into two Z bosons. Those further decayed into a pair of electrons and muons, marked in the figure with green and red lines, respectively [MT12].

3.2. The Concept of Integrated Luminosity

For accelerator physics two parameters are of prime importance. To provide that new particles (for example with higher masses) can be generated in collisions, a certain energy has to be achieved. However, it is also essential to reach sufficient statistics, since a new particle discovery or new mechanisms are accepted with a statistical significance of 5σ. To reach these statistical requirements the particle interaction rate should be as high as possible. The number of events per second $\frac{\mathrm{d}R}{\mathrm{d}t}$ scales linearly with the interaction cross section σ_p. The *luminosity* $\mathcal{L}$ is the slope of this characteristic:

[1] CERN: **C**onseil **E**uropéen pour la **R**echerche **N**ucléaire

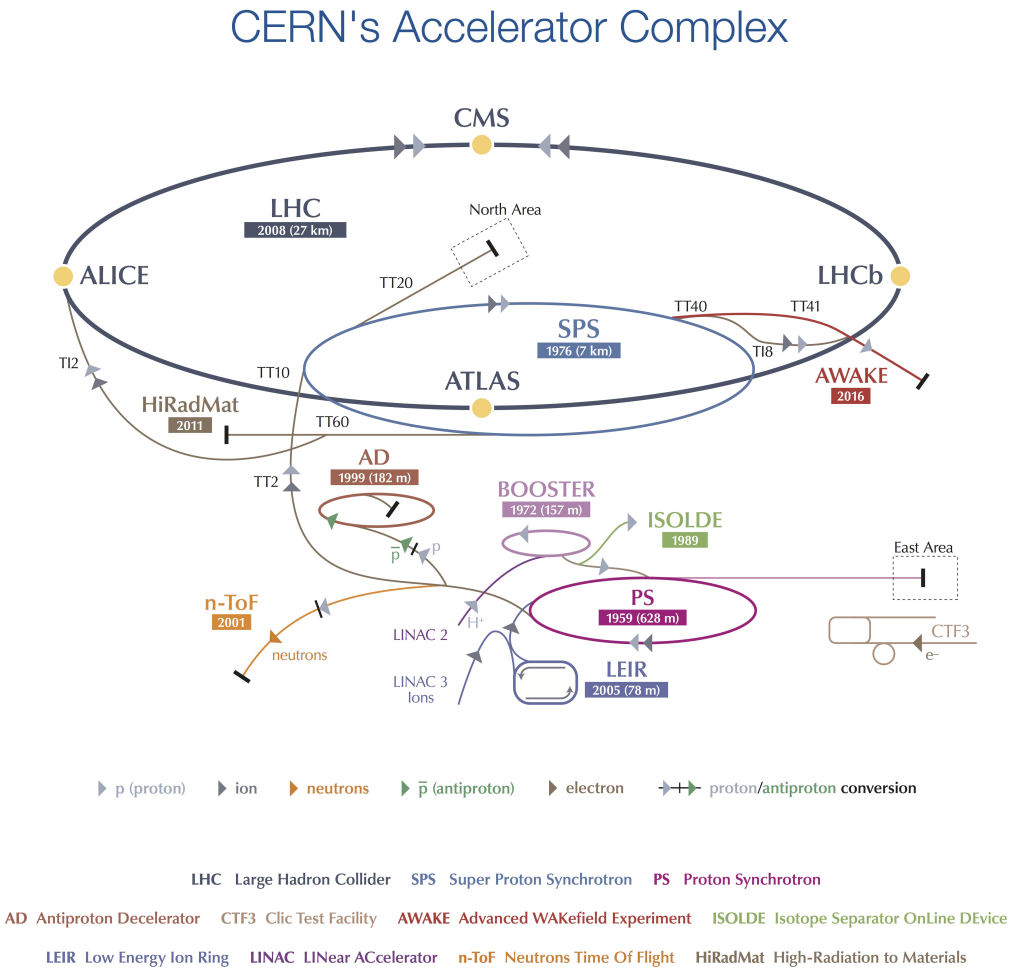

Figure 3.1.: Illustration of accelerators and detectors at CERN. Protons starting in the LINAC2, getting further accelerated in the BOOSTER, PS and super SPS, before finally reaching the nominal energy of 6.5 TeV after 20 minutes inside the LHC ring [Haf13].

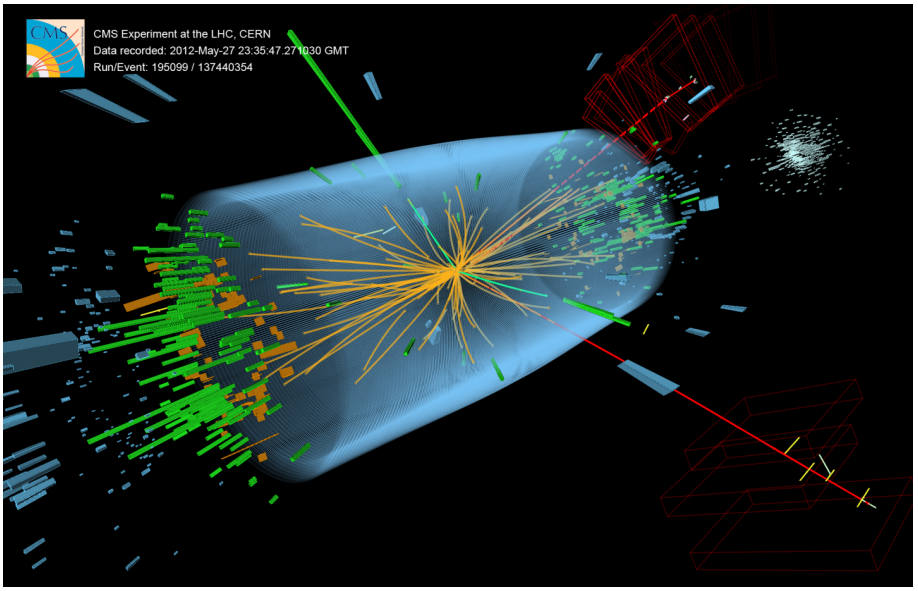

Figure 3.2.: Illustration of a Higgs-like event in the CMS detector. The Higgs boson decayed into two Z bosons, which further decayed into two electrons (green lines) and two muons (red lines) [MT12].

$$\frac{\mathrm{d}R}{\mathrm{d}t} = \mathcal{L} \cdot \sigma_p \qquad . \tag{3.1}$$

Calculating the luminosity of two colliding equal bunched Gaussian beams leads to

$$\mathcal{L} = \frac{N_1 N_2 f N_b}{4\pi\sigma_x\sigma_y} \qquad ,$$

with the number of particles per bunch N_1 and N_2, the circulation frequency f, the number of bunches N_b and the cross sections perpendicular to the beam σ_x and σ_y.

For the design of an accelerator experiment and to evaluate the potential of discoveries, the total amount of collisions over the runtime is a fundamental property. With the (time) *integrated luminosity* (3.2) the total number of events can directly be determined.

$$\mathcal{L}_{\mathrm{int}} = \int_0^T \mathcal{L}(t')\mathrm{d}t' \tag{3.2}$$

The total number of events N is then given by

$$N = \mathcal{L}_{\mathrm{int}} \cdot \sigma_p \qquad .$$

The integrated luminosity is used as an important comparable property for accelerator experiments. Since the number of events is huge, the integrated luminosity is usually expressed in units of inverse femtobarns (fb^{-1}; $1\,\mathrm{b} = 10^{-28}\,\mathrm{m}^2$) instead of SI-units[2] (m^{-2}) [HM06].

3.3. The CMS Experiment

The CMS[3] experiment is one of the main detector complexes at CERN. It houses the most powerful superconducting solenoid ever made to generate a magnetic field of 3.8 T and it is in total 21 m long, 15 m high and 15 m wide with a weigth of 14 000 t [Col].

The location of the subdetectors in the CMS detector is visualised in figure 3.3. The silicon tracker is located in the centre of the detector surrounding the beam. Particle trajectories and momenta can be reconstructed. The energy of electromagnetic interacting particles and hadrons can be determined with the electromagnetic calorimeter (ECAL) and the hadronic calorimeter (HCAL), respectively. Since muons are *minimum ionising particles* (MIPs), the energy loss due to ionisation, even in dense matter is low and therefore a detection can be realised outside the solenoid.

3.4. Current CMS Tracker

The CMS tracker, how it is currently installed, is schematically visualised in figure 3.4. Visible is a quarter of a cross section in r-z direction, where z is the axis of the beampipe. The inner tracker, marked in green, has a radius of roughly 200 mm and consists of pixel modules. Displayed in blue and red are the single-sided and double-sided modules of the tracker which contain strip sensors. The tracker is designed to cover a pseudorapidity up to $|\eta| \approx 2.4$, which is directly correlated to the forward angle.

[2] french: **S**ystème **I**nternational, english: International System [NISb]
[3] CMS: **C**ompact **M**uon **S**olenoid

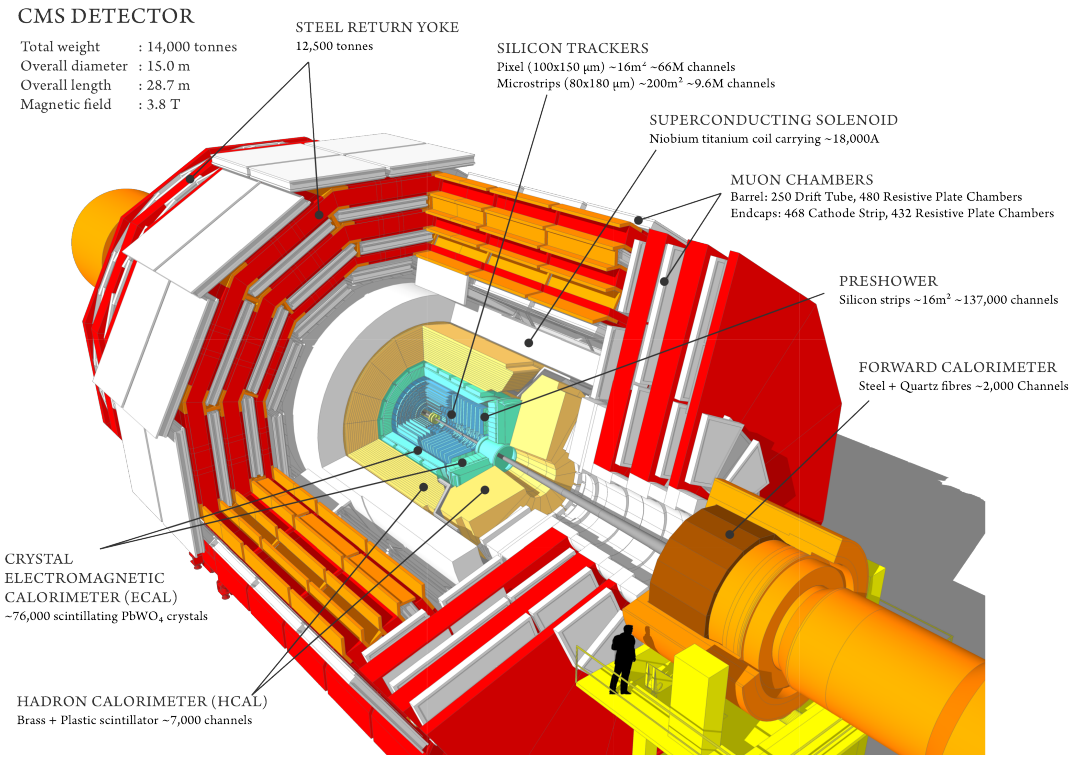

Figure 3.3.: Schematic illustration of CMS and its subdetectors. From outside to inside: Muon chambers, a superconduction solenoid, the hadronic calorimeter (HCAL), the electromagnetic calorimeter (ECAL) and the silicon trackers [Tay11].

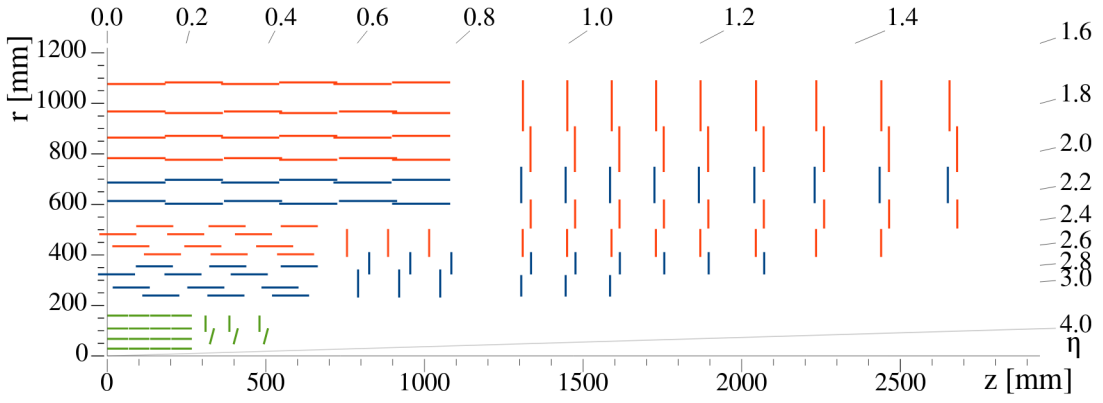

Figure 3.4.: Schematic illustration of the modules inside one quarter of a r-z cross section of the Phase-1 tracker. At low radii pixel modules are marked in green. Single-sided modules are coloured in red, double-sided in blue [Col17].

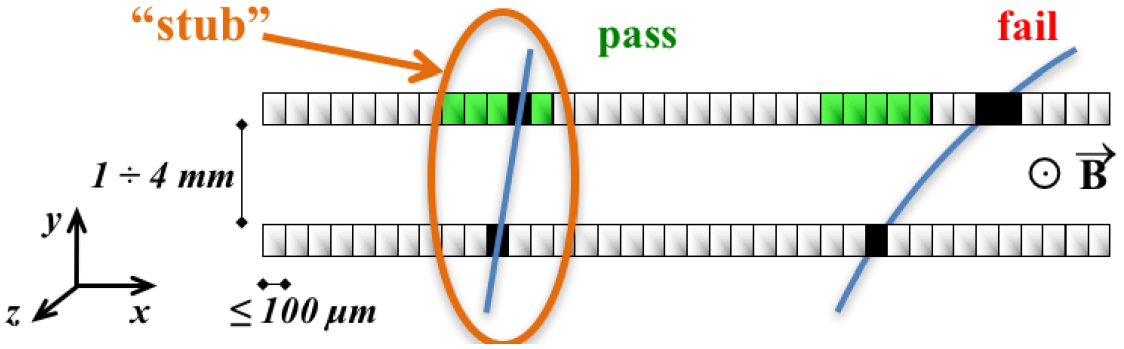

Figure 3.5.: Schematic illustration of the stub finding for triggering in Phase-2[Col17].

3.5. Outer Tracker in Phase-2

The current tracker was designed for an integrated luminosity of 500 fb^{-1}. In Phase-2, after an operating time of roughly 10 years, the integrated luminosity will be approximately 3000 fb^{-1}. This leads to a higher reaction rate of up to 200 collisions per bunch crossing which requires an advanced pattern recognition and increased granularity [Col17]. One crucial physical parameter which is estimated with the tracker is the traverse momentum p_T of charged particles. It is dependent on the trajectory radius r, the charge q and the magnetic field B

$$p_T = r \cdot q \cdot B \quad . \tag{3.3}$$

The p_T-modules in Phase-2 will constrain the accepted orbit radius for high momentum particles. An overall and an explosion view of these modules can be found in the appendix (A.2) In short, those modules consist of two back-to-back strip sensors (2S) or one macro pixel and one strip sensor (PS). Because of the increased reaction rate, the data generation increases as well. A binary readout of the signal will decrease the data rate and speed up the acquisition. The traverse momentum can also be used as a trigger condition. If a certain value of $p_T > 2$ GeV is exceeded, the information will be adjoined to the first (L1) trigger stage at 40 MHz. The technical realisation is illustrated in figure 3.5. One module is schematically indicated with its upper and lower sensor. A traversing particle hits the first sensor in a specific area. The green area marks the window were the second hit in the top sensor has to be detected, to accept trajectory as a high momentum particle. The traverse momentum threshold can be adjusted by the width of the according window.

A sketch of the tracker design for Phase-2 is displayed in figure 3.6. The inner tracker consists of pixel modules with two and four readout chips, marked in green and yellow, respectively. Blue coloured, partially tilted segments represent PS modules, which house pixel and strip detectors. The red 2S modules consist of two back-to-back mounted strip sensors [Col17].

Estimations of the radiation environment are given by CMS FLUKA[4] simulations. The fluences were simulated under the frame conditions of proton-proton collisions after an integrated luminosity of 3000 fb^{-1}, a center of mass energy of 14 TeV and a total cross section of $\sigma_p = 80$ mb. The maximum fluences and doses under this conditions for the different regions are shown in table 3.1. Figure 3.7 illustrates the expected fluences in the range of 10^{14} n_{eq}/cm^2 to 10^{16} n_{eq}/cm^2. The corresponding illustration of the distribution of the dose can be found in the appendix (A.1). Dependent on the radial position inside

[4]german: FLUktuierende KAskade, english: Fluctuating Cascade

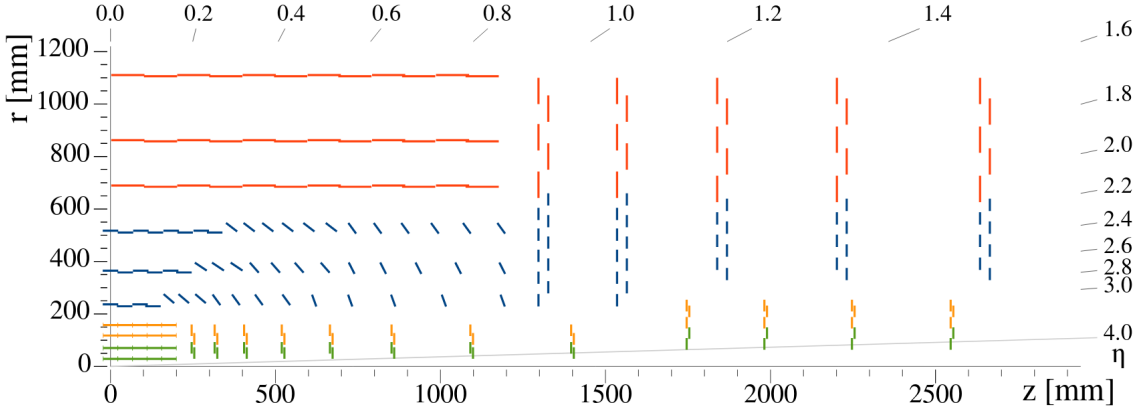

Figure 3.6.: Schematic illustration of the tracker design for Phase-2. Next to the beampipe in the inner tracker, the pixel modules are placed. Marked in green and yellow are modules with two and four readout chips, respectively. In the outer tracker the blue segments are the PS modules, where a silicon strip- and a pixel sensor are housed. The red coloured markings represent the 2S modules with two strip sensors [Col17].

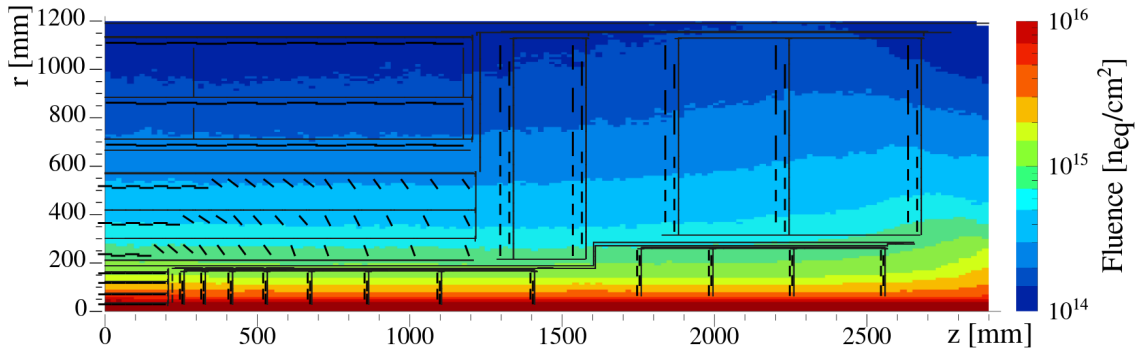

Figure 3.7.: FLUKA based simulation of the expected fluences after the runtime of 10 years in Phase-2[Col17].

Table 3.1.: Expected fluence and ionisating dose for different regions of the tracker [Col17].

Region or component	Max. fluence (n_{eq}/cm^2)	Max. Dose (MGy)	r (mm)	z (mm)
IT barrel layer 1	$2.3 \cdot 10^{16}$	12.1	28	0
IT barrel layer 2	$5.0 \cdot 10^{15}$	2.90	69	0
IT barrel layer 4	$1.5 \cdot 10^{15}$	1.04	156	89
IT forward, ring 1	$1.0 \cdot 10^{16}$	9.25	51	252
IT service cylinder	$1.3 \cdot 10^{15}$	0.70	170	260
OT PS modules	$9.6 \cdot 10^{14}$	0.56	218	129
OT 2S modules	$3.0 \cdot 10^{14}$	0.09	676	2644

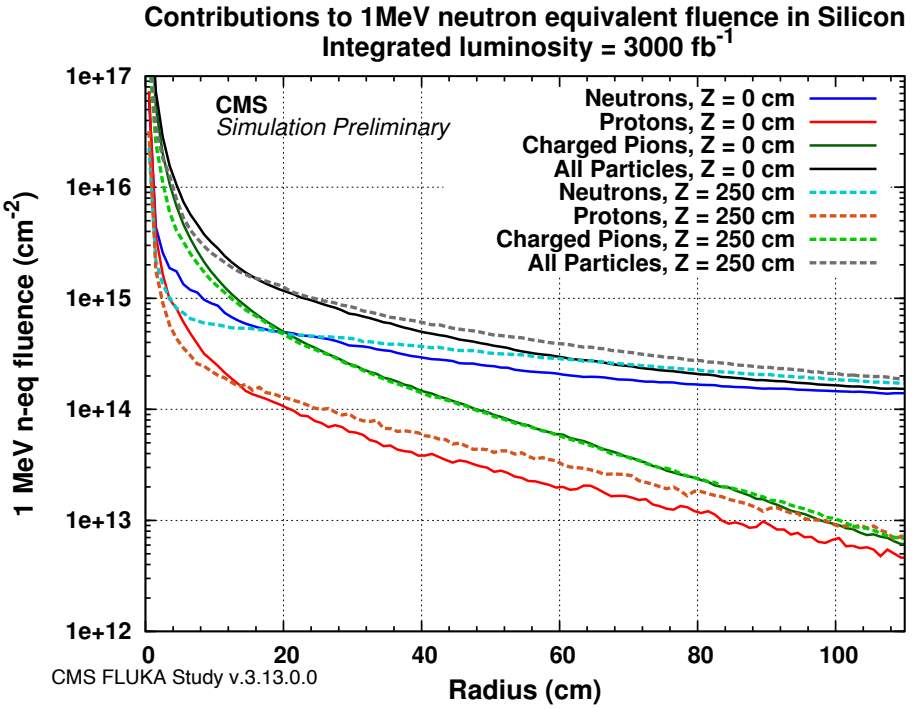

Figure 3.8.: FLUKA simulated particle contribution to the total fluence. With higher radii the neutron to charged particle fraction gets higher. For the 2S modules in the outer tracker neutron irradiation dominates over protons and pions [Col15].

the tracker, the particle composition of the fluence varies. An according simulation for Z= 0 cm and Z= 250 cm is displayed in figure 3.8. Above a distance of roughly 50 cm the neutron fraction starts to predominate over charged particles. In the region of the 2S modules in the outer tracker ($r \geq 60$ cm), the fluence is dominated by neutrons with a charged particle fraction of roughly 20 to 30%.

4. Experimental Setups

4.1. Probe Station

Two probe stations are available at ETP to measure the electrical characteristics of sensors and diodes. The temperature can be controlled from -30°C to 60°C via peltier elements and dry air. An aluminum box provides a shielding from the environment. In figure 4.1 the interior is displayed. Measurement devices which are placed oustide of the box are listed in B.1. Samples are placed on a metal jig and fixated via vacuum holes. The jig is set to high voltage up to 1000 V for biasing. Grounding is usually done with the bias needle over the bias ring. This enables measuring the electrical properties of the sample like IV and CV characteristics with just a bias needle. Strip measurements are performed with strip needles of a smaller tip radius (2 µm) than the bias needle (7 µm). The needle adjustments are monitored by a microscope and a camera which is connected to a monitor. The setup is controlled with a dedicated LabVIEW program [Ins]. More detailed information can be found in [Erf09]

4.2. ALiBaVa Setup

The electrical properties of a sample can be determined with one of the probe stations. However, for the qualification of silicon strip sensor the outcoming signal is also a crucial parameter. The determination of the signal is performed with an ALiBaVa[1] system. It consists of a daughterboard, which incorporates the read-out chip, a motherboard to process the data and control the data acquisition, a scintillator for triggering and a PC for general monitoring and controlling. A picture of the daughterboard is presented in figure 4.2. It is placed inside an aluminum box. Using irradiated sensors requires a cooling system, which includes dry air, temperature sensors and peltier elements. In the figure the basic components are indicated with numbers from 1 to 4. Number 1 marks the connection to the motherboard outside the aluminum box. Two Beetle chips with 128 channels each are used for the signal readout (number 2) [Hei]. It is connected with wire-bonds over a pitch adapter (number 3) to a sensor. The sensor is fixated on a copper block to ensure sufficient thermal contact. Finally, a radioactive source holder is indicated with number 4. A strontium-90 source was used for signal measurements. The holder can be positioned via a xyz-stage over the sensor so that the emitted electrons traverse the sensor. A scintillator is placed below the copper block to trigger the readout.

[1] A Liverpool Barcelona Valencia system [SYS]

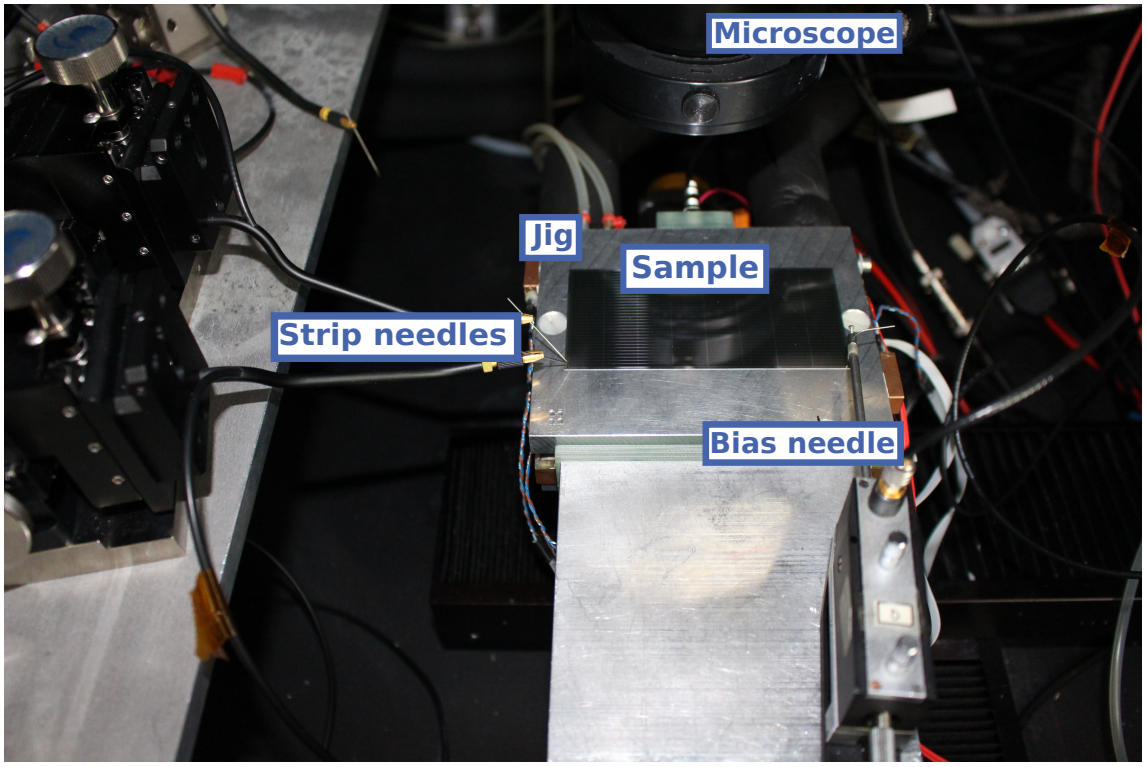

Figure 4.1.: Interior of the probe station at ETP. A sample is fixated on the jig and is biased with a bias needle. Strip needles are used to perform interstrip measurements or to bias smaller structures.

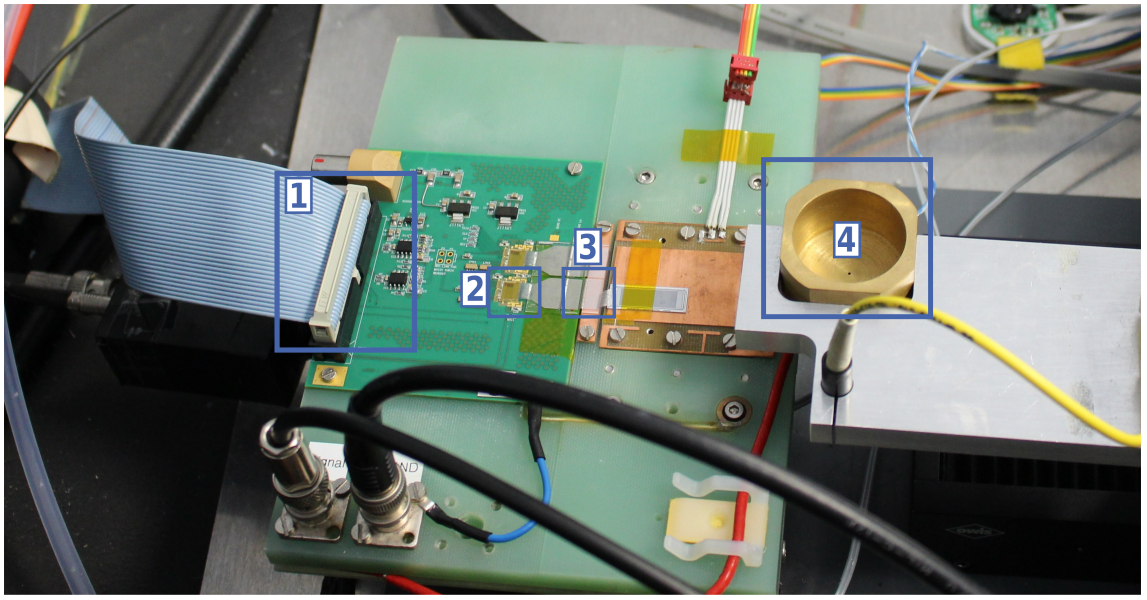

Figure 4.2.: ALiBaVa daughterboard with basic components. Connection to the motherboard (1), Beetle readout chip (2) connected to a sensor on the copper block via a pitch adapter (3). The radioactive source can be positioned right above the sensor with a moveable holder (4).

The setup can also be used to study the annealing of the signal. Typical annealing temperatures are between 60°C and 80°C, while measurements are performed at -20°C. IV characteristic and charge colletion are taken per annealing step (see appendix B.1).

Pedestal Run

First, a pedestal run is performed to estimate the noise per strip and to exclude noisy channels from the analysis. In general, the counts in ADCs are composed of the pedestal $P(s,e)$, the common mode $D(e)$ and the signal Signal(s,e).

$$ADC(s,e) = P(s,e) + D(e) + \text{Signal}(s,e) \tag{4.1}$$

Those parameters are dependent on the channel number s (every channel is connected to exactly one strip) and events e (e.g. trigger). The pedestal per channel $P(s)$ is estimated by repeatedly and randomly reading-out the chip. This method yields the average signal offset per channel in absence of a traversing particle.

$$P(s) = \frac{1}{N}\sum_{e=1}^{N} ADC(s,e) \qquad . \tag{4.2}$$

External noise is respected by a common mode noise correction. The external noise affects all strips in a smiliar manner. Therefore the pedestal as a specific offset for one strip has to be subtracted from the ADC counts. The common mode is then given by the mean over all strips

$$D(e) = \frac{1}{N_\text{s}}\sum_{s=1}^{N_\text{s}} (ADC(s,e) - P(s)) \qquad , \tag{4.3}$$

where N_s is the number of channels (strips), which is 128 for the Beetle chip of the ALiBaVa daughterboard. The common mode is distributed around zero as visible in figure 4.3. To calculate the noise per strip, the common mode has to be subtracted from the pedestal for each strips to exclude external sources. This is called the corrected pedestal [Eur14]

$$P_c(s) = P(s) - D(e) \qquad . \tag{4.4}$$

Finally, the noise per strip is the standard deviation of the corrected pedestal distribution

$$\text{Noise}(s) = \sqrt{\frac{1}{N-1}\sum_{e=1}^{N} (P_c(s) - \overline{P}_c(s))^2} \qquad . \tag{4.5}$$

The noise per strip in ADCs is presented in figure 4.4 for every channel. On the left side, marked in green (channel 0 to 128), the first chip is not bonded to any sensor. On the second chip an 'Irradiation' sensor is bonded, where the strip for channel 210 to 249 are included into the analysis. Channels of the used chip, which are not bonded to a sensor show a high noise as an artefact which excludes the non-bonded strips.

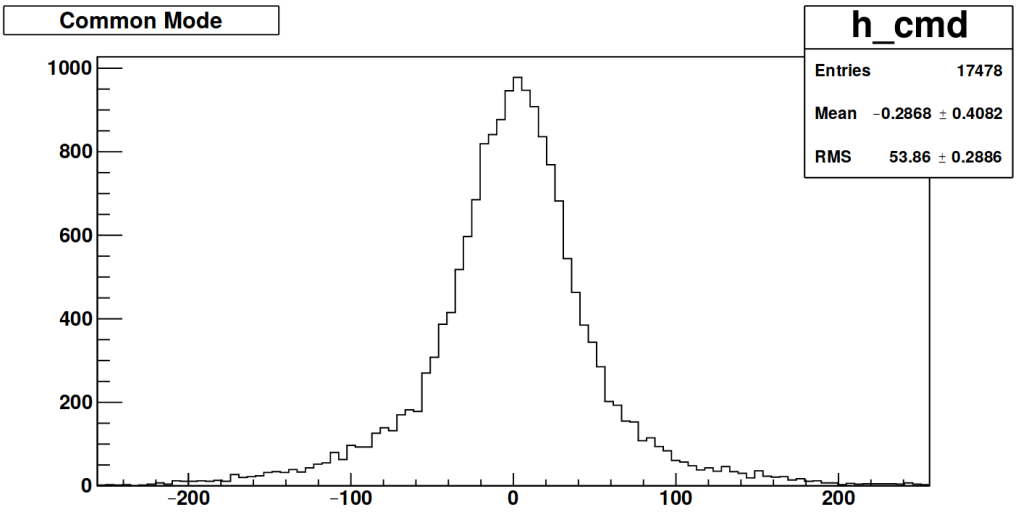

Figure 4.3.: Exemplary plot of the common mode distribution.

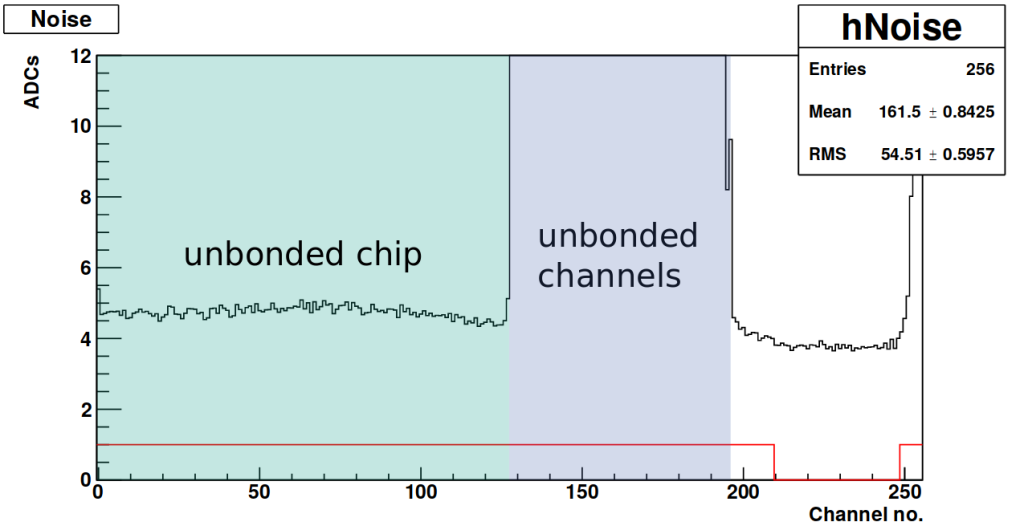

Figure 4.4.: Exemplary plot of the noise per strip for an irradiated sensor. The sensor is bonded on the right side of the second chip. Strips between channel 210 and 249 are included in the analysis. Masked channels are indicated by the red line.

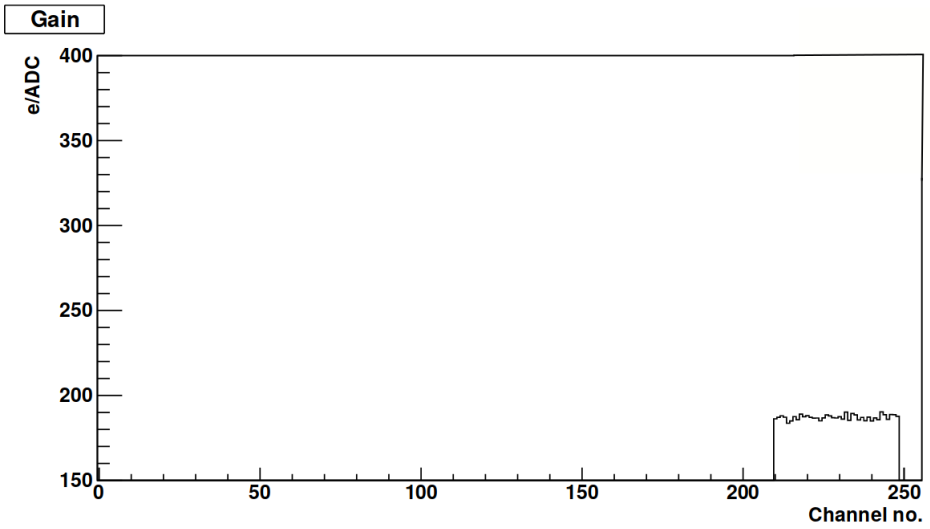

Figure 4.5.: Gain for every unmasked channel for the same measurement as in figure 4.4.

Calibration Run

In general the readout chip yields an output in units of ADC counts. The conversion factor from ADC counts into electrons is called gain. This factor can change according to the input capacitance. Therefore a calibration run is performed before every signal measurement.

Every channel of the Beetle chip has its own capacitor. All capacitors are charged with 15 000 electrons for the calibration run. After discharging them, a time delay scan is performed, where the maximum yields the gain in electrons/ADCs. This procedure is done 100 times for one calibration run and the resulting gain for each strip is given by the mean of the runs. An exemplary plot of the gain is shown in figure 4.5. As visible only the unmasked sensors are taken into account for the analysis. The variation of the gain from channel to channel is expected to be approximately 1.9% [Löc06].

A more precise evaluation of the gain is carried out by performing a charge scan [Sys14]. The delay of the maximum discharge is given by the delay scan. If the signal after this delay is plotted over the charge, the gain can be determined by using the inverse slope of this characteristic. This additional scan leads to an increased accurancy of a few percent. However, it is time consuming and the chip to chip variations of 19.1% [Löc06] are more significant. These variations occur due to the uncertainities on the capacity of the capacitors in the production. A signal calibration with one standardised sensor design is required if different chips are used within an irradiation campaign. Otherwise the results of the campaign are not comparable.

Radioactive Source Run

The ALiBaVa system provides two operating modes, resulting from two available clocks. A TDC[2] provides a time resolution of 1 ns within a 100 ns time window. Therefore the signals pulse shape can be resolved. With the system wide 25 ns clock, the readout is faster but a pulse shape reconstruction is not possible anymore [Eur14]. A scheme of the two clocks and the triggered readout is displayed in figure 4.6.

The TDC is used for studies within this thesis to resolve the signal shape. A signal measurement with the radioactive source (RS run) includes 100 000 triggered events. Figure

[2]TDC: **T**ime **D**igital **C**onverter

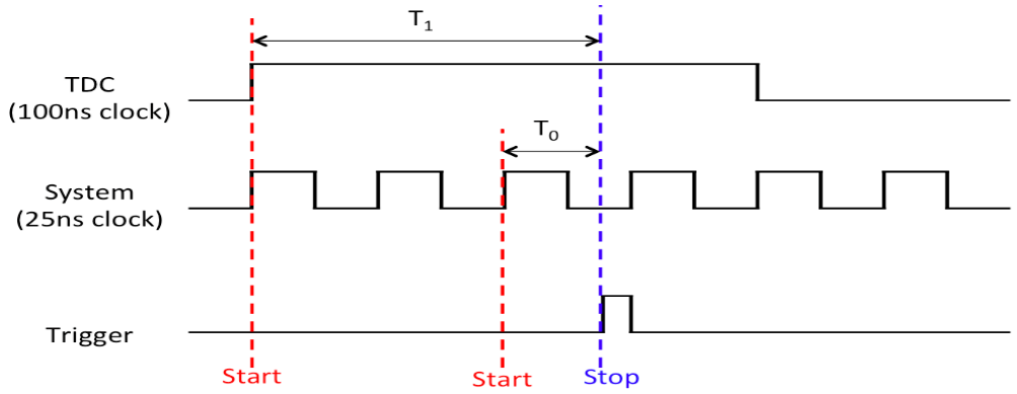

Figure 4.6.: Clocks of the ALiBaVa system. The TDC provides a 100 ns second clock with a time resolution of 1 ns. This provides a pulse shape reconstruction. The readout is faster with the system clock but the pulse shape is lost [Eur14].

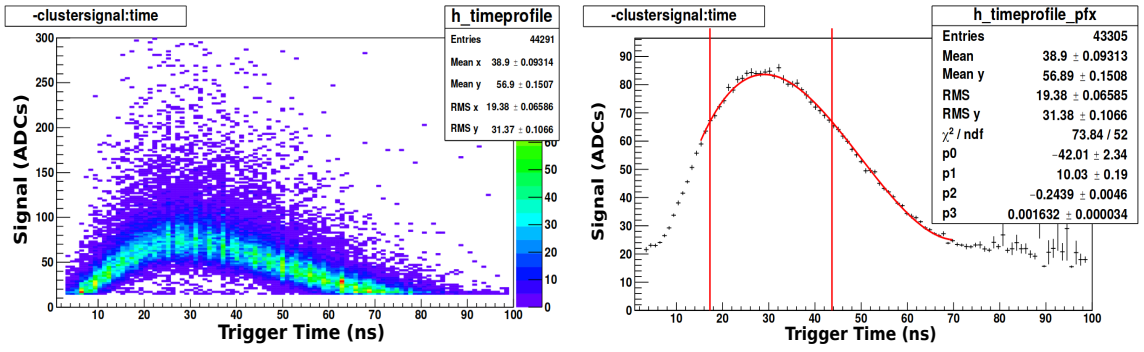

(a) (b)

Figure 4.7.: Signal entries for all events (a) and averaged (b) dependent on the timing. In (a) the colour code indicates the entry numbers. The green pulse shape already emerges. In (b) the pulse shape of the signal is visible. For the analysis a time window around the maximum is defined (red vertical lines) in which entries are accepted. This ensures that the maximum signal is taken into account and noise is further excluded.

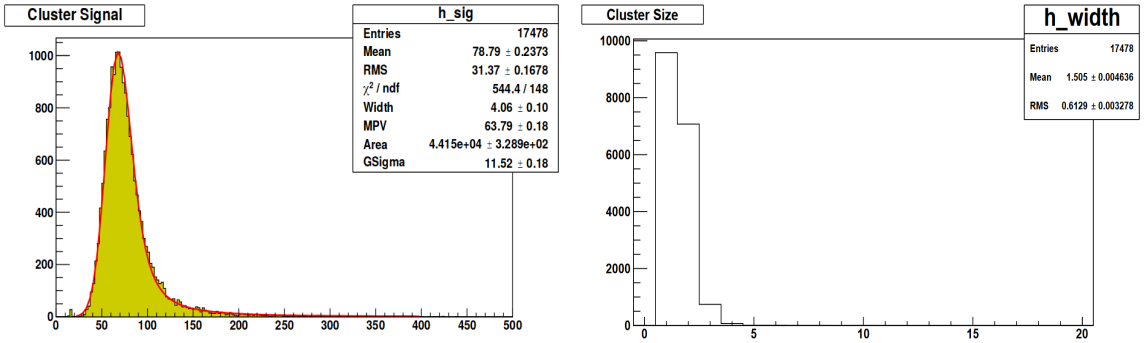

(a) (b)

Figure 4.8.: Cluster signal with a Landau-Gaussian fit (a). The requirement of a signal-to-noise-ratio above four leads to a cut-off at low signals. Otherwise a second noise peak would be visible and distort the analysis. Cluster size displayed in (b). Events with a cluster size above 4 are not occuring.

4.7a is an exemplary illustration of the signal entries over time. The number of entries is indicated by the colour code. A pulse shape emerges in green. This plot can be used as a verification of the latency adjustments. If those adjustments are not fitting, the pulse shape would be cutted of. It could also happen that the maximum of the signal is not visible. If this is the case, most of the signal would not be taken into account which would lead to unreliable results. The mean values of all events at a certain time are displayed in figure 4.7b. A fit is indicated with a red line. Around the maximum of the fit a time window is defined, which is illustrated with vertical red lines. Only signals which arrive inside this time window are taken into account for the analysis. This procedure reduces the statistics, but improves the quality of the signal. If higher statistics is required, the window can be broadened.

An additional requirement, which is applied before the correct timing, is a sufficient SNR[3]. When an electron, emitted by a radioactive source, traverses the sensor, generated charge is collected by a set of strips. This set of strips is called cluster. The seed of a cluster is defined as the strip with the highest signal and a SNR ≥ 4. Neighbouring strips are accepted to contribute to the cluster if SNR ≥ 2. An example of the cluster signal is shown in figure 4.8a. The expected Landau-Gaussian shape is visible and additionally indicated with a corresponding fit (red line). Since the cluster signal represents the amount of electrons which is generated in the material, it is used for material classification.

Figure 4.8b indicates the distribution of the cluster size. The most probable cluster size is one, which means that no additional strip is taken into account for the analysis. Cluster sizes of four are already rare and greater than five is not occuring. Since the radioactive source is placed above the sensor with a relatively small collimator, the electrons traverse the sensor mainly perpendicularly. A higher cluster size implies a higher incoming angle or delta-electrons. Cluster sizes of two can also occur if a particle traverses the sensor between to strips.

Since the readout in Phase-2 is binary, it has to be ensured that at least one particular strip can reach a certain threshold. Therefore the signal of the seed is used for sensor qualification within this thesis. The seed signal is visualised in figure 4.9. Due to the definition of the seeds SNR≥ 4, the cut at roughly 16 ADCs is visible, indicated with a blue dashed line. Otherwise a comparable high noise peak would appear at less signal heights. The MPV[4] of the signal distribution is calculated by the Landau fraction of a

[3]SNR: **S**ignal-to-**N**oise-**R**atio
[4]MPV: **M**ost **P**robable **V**alue

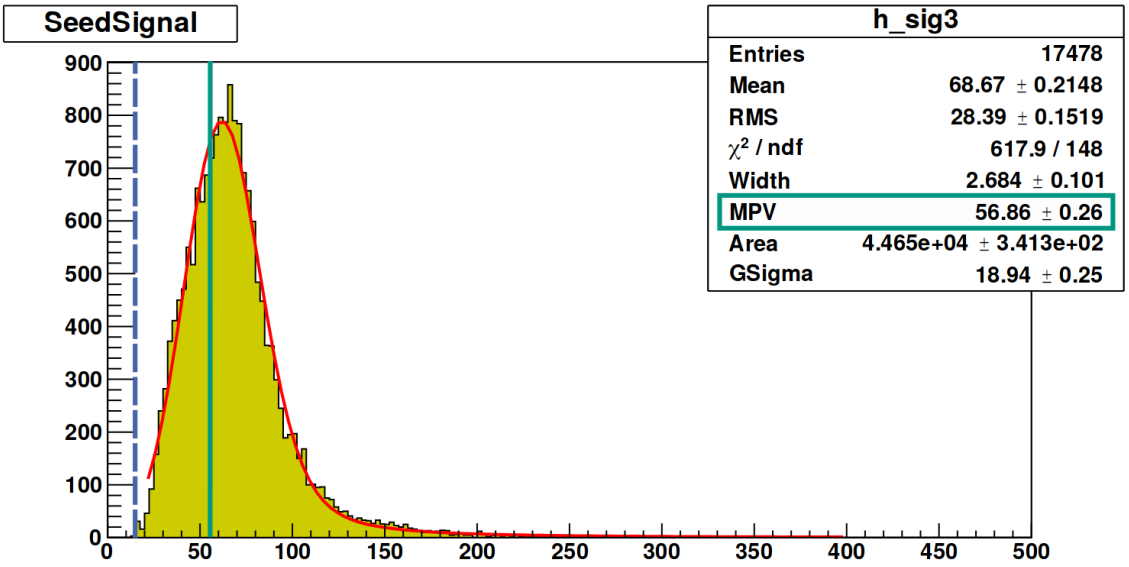

Figure 4.9.: Seed signal with a Landau-Gaussian fit. The blue dashed line indicates the cut-off below four times the noise. The green line represents the MPV calculated by the Landau fraction of the fit.

Landau-Gaussian fit[Off96]. The MPV, which is marked with a green line, is therefore slightly below the peak of the gaussian broadened Landau distribution. The rule of thumb

$$\mathrm{MPV}/3 \geq 4 \cdot \sigma_{\mathrm{readout}} \quad , \tag{4.6}$$

where the noise of the readout chip CBC is $\sigma_{\mathrm{CBC}} \approx 1\,000$ electrons, leads to a qualification limit of MPV $\geq 12\,000$ electrons for the 2S sensors in Phase-2.

Another qualification parameter is the efficiency displayed in figure 4.10. The efficiency can be determined by integrating over the signal. It corresponds to the entries which are above a certain signal threshold. The amount of entries above this threshold divided by the total entries yields the efficiency. To qualify the signal an efficiency of for example 95% at a certain threshold can be demanded.

4.3. Irradiation Facilities

X-ray irradiations were carried out with the x-ray setup at ETP [Exp]. A picture of the basic devices inside the lab is shown in 4.11. The x-ray tube itself is placed inside an aluminum and lead cover to protect the environment from radiation. A generator outside of the shielding provides electrical power for the x-ray tube. It can be adjusted to a maximum voltage of 60 kV and current of 33 mA. The sample position can be automatically adjusted with a xy-stage. This is done by software or manually with the MCL[5]. A high voltage power supply is used to bias a diode and to readout the current. With a pin-diode the intensity of the beamspot profile can be scanned.

The lambda low voltage power supply controls peltier elements which were used for cooling of sensors while irradiating. The cooling apparatus is displayed in figure 4.12. A humidity sensor measures the humidity which can be decreased by flushing the box with dry air. Two temperature sensors monitore the precooling and the jig temperature. A red laser

[5]MCL: **M**otor **C**ontrol **L**ogic

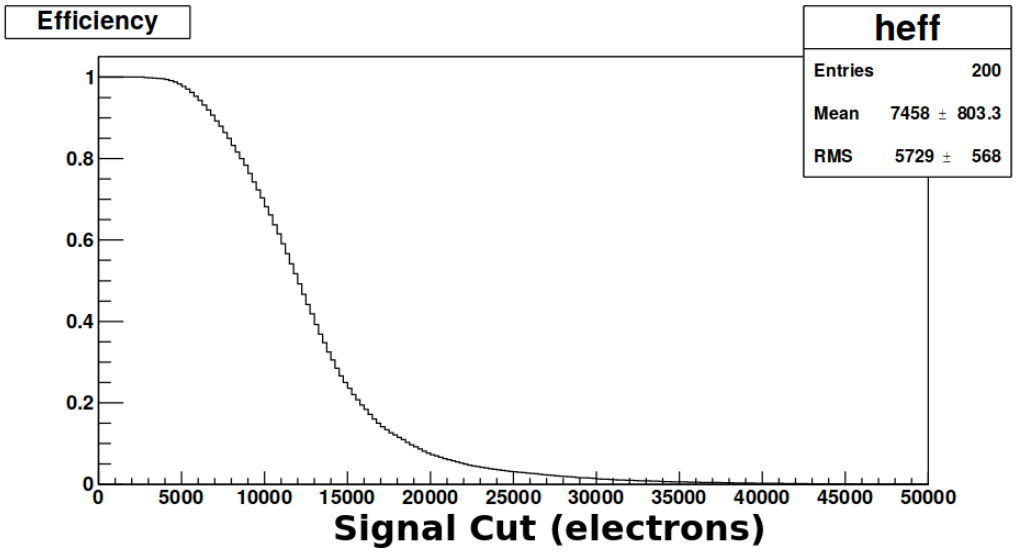

Figure 4.10.: Relative number of seed events as a function of the applied cut.

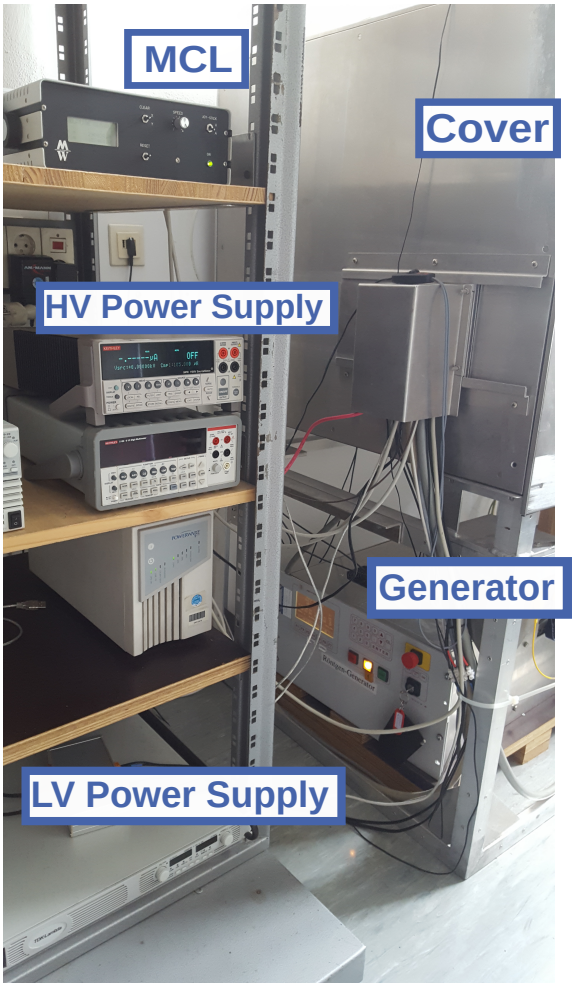

Figure 4.11.: Devices in the irradiation lab at ETP. The main devices outside the cover are a MCL for the motor control of the xy-stage, a high voltage power supply to bias and readout a pin-diode, a generator to drive the x-ray tube and a low voltage power supply to control the peltier elements for cooling.

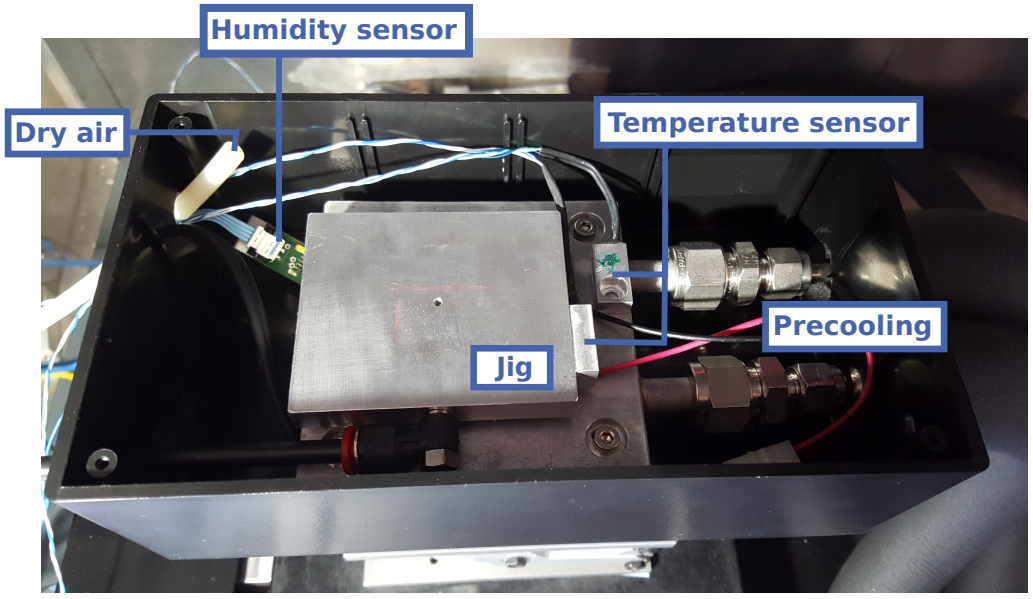

Figure 4.12.: Opened cooling system for irradiation containing sensors for humidity and temperature at the precooling and the jig. It is flushed with dry air to provide a sufficiently low dewpoint. The sensor is placed on the jig and its position is adjusted with a laser crosshair.

crosshair for positioning is slightly visible on top of the jig as well. The cooling reaches at least -12°C, which prohibits annealing during the irradiation procedure. Avoiding uncontrolled annealing is especially important for samples which are irradiated with heavy particles, since bulk damage annealing is already significantly visible after one day at room temperature.

Samples investigated in these studies were also irradiated with neutrons and protons. Neutron irradiation (1 MeV) is performed in a spallation reactor in Ljubljana at Jozef Stefan Institute (JSI) in the frame of AIDA-2020[6] [AIDb]. While irradiating, the samples cannot be cooled and heating-up a few degrees. Therefore an annealing equivalent of 20 h room temperature is expected. Samples were irradiated with protons (23 MeV) at the cyclotron at KIT by the Zyklotron AG (ZAG) [AIDc][AG]. With a proton beam the samples are scanned in a meander-like pattern, which provides homogeneous irradiation. While the irradiation procedure is ongoing, the samples are cooled down to at least -30°C. Therefore annealing is not expected besides the handling time of roughly 1 h. The uncertainity for both irradiation procedures is demanded to be less than 15%.

[6] AIDA: **A**dvanced European **I**nfrastructures for **D**etectors at **A**ccelerators [AIDa]

5. Sensor Properties after Irradiation

5.1. Quality Assurance of Sensor Properties after Irradiation

Before charge collection measurements and annealing studies can take place, it has to be ensured that the sensor properties as well as the fluences are in the expected range. This quality assurance is done by calculating the current related damage rate α. The normalised leakage current over the fluence is presented in figure 5.1a at an operating voltage of 600 V for all sensors used in this chapter. Since the leakage current for sensors at the same fluence is fluctuating, the mean is taken with the appropriate standard deviation. Properties of sensors with a fluence of $\Phi = 1 \cdot 10^{15} \mathrm{n_{eq}/cm^2}$ are not further presented in this chapter but the data for the leakage current is taken to provide a better fit through three instead of two points. The resulting uncertainity on the fit is indicated with a blue band. The term *without annealing* or *before annealing* refers to an additional uncontrollable annealing as low as reasonably achievable. The samples are insufficiently cooled during transportation, irradiation and activity measurements after irradiation. Moreover, for neutron irradiation in spallation reactors no cooling is possible as well. A concervative estimation for samples that were irradiated at JSI is about 20 h room temperature and 1 h for irradiations at ZAG [AG]. Therefore the approriate damage rate is expected to be $\alpha = 8 \cdot 10^{-17}\mathrm{A/cm}$ for an annealing of 60 min at 21°C. The fit yields a damage rate of $\alpha = 8 \pm 0.7 \cdot 10^{-17}\mathrm{A/cm}$. After an annealing of 80 min at 60°C the damage rate is expected to be $\alpha = 4 \cdot 10^{-17}\mathrm{A/cm}$ [Mol99]. The corresponding data with a linear fit is presented in figure 5.1b. Compared to the expected damage rate, the fit yiels a 20% higher value of $4.8 \pm 0.56 \cdot 10^{-17}\mathrm{A/cm}$. However, the fluctuations are even higher, since the IV characteristics were taken within the annealing studies in the ALiBaVa setup. It shall also be mentioned that the damage rate, evaluated by Moll, is valid for diodes or simpler structures. The leakage current per volume unit of a strip sensor is generally higher. Its electric field is more sophisticated and higher surface currents occur.

Basic quality assurance regarding other properties like strip leakage current, coupling capacitance, bias resistance and interstrip capacitance as well as resistance were also performed on some sensors. It was observed that the interstrip resistance decreases with the fluence and the strip leakage current increases, as expected. The other parameters were not chaning after irradiation. Therefore the results are not further presented.

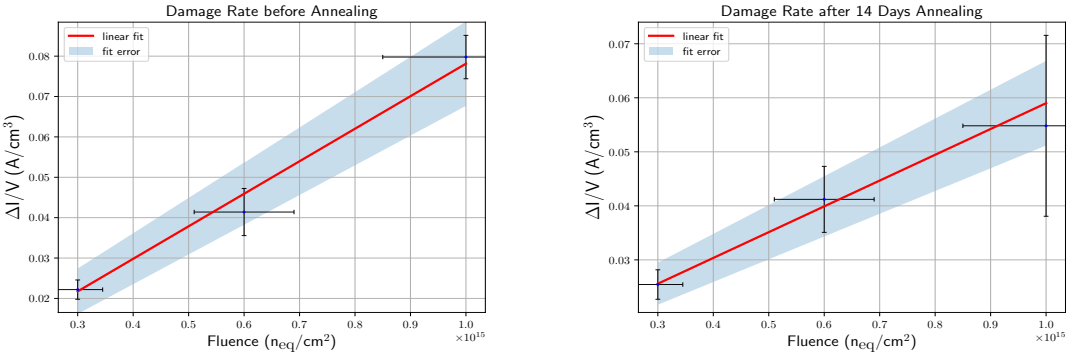

(a) (b)

Figure 5.1.: Damage rate at an operating voltage of 600 V and T≈ −20°C before (a) and after 14 days annealing (b).

5.2. Validation of Optimal Sensor Thickness for 2S Sensors

The sensor thickness is one of the crucial paramters which mainly defines the leakage current, operating voltage and therefore power consumption as well as the charge collection. The leakage current is expected to scale linearly with the thickness. Regarding the leakage current sensors should be as thin as possible. However, to provide a sufficient signal, a certain amount of detector volume is required in which charged particles can deposit their energy and generate electron-hole pairs. It was observed that higher thicknesses result in a stronger reverse annealing of the signal [Col17]. The aim of this chapter is therefore to find an optimal sensor thickness with which the sensors provide a sufficient signal with respect to annealing. Investigated sensors have an active thickness of 200 µm and 240 µm and are manufactured by HPK in respect to the 2S sensor design. Sensors with an active thickness of 300 µm stem from the initial HPK campaign [Hof11]. The original nomenclature of the samples was changed to a plot label, where the first three numbers mark the active thickeness. The following letters and numbers are just an enumaration of the sensors. Sensor 300S1 refers to a sensor with an active thickness of 300 µm. An overview of the plot labels with their according sensor names can be found in C.2. The measurement procedure to estimate the seed signal as well as the annealing were performed with the ALiBaVa setup, which is further explained in section 4.2. A MPV $>$ 12 000 is required to label the seed signal as sufficient. In the following, the 12 000 electrons margin is indicated with a red layer.

All signal measurements were performed at T $\approx$ −20°C. Since these investigations are focused on the 2S region in Phase-2, the operating voltage is 600 V and the maximum fluence is $\Phi = 3 \cdot 10^{14} \mathrm{n_{eq}/cm^2}$. The target fluence of $\Phi = 3 \cdot 10^{14} \mathrm{n_{eq}/cm^2}$ does reflect the sample fluence, approximately. Reference measurements were occasionally performed during the irradiation process, which yield the real sample fluence. A general uncertainity of 15% on the fluence is expected. Deviations of more than 15% according to reference measurements are explicitly mentioned in the plots. A summary of all reference measurements results can be found in C.2. A conservative estimation of the signal uncertainity is 1000 electrons. Error bars are not included in the plots, since the individual uncertainities cannot be accurately quantified.

The annealing behaviour of the seed signal for the three thicknesses in question is presented in figure 5.2. Sensors with an active thickness of 200 µm can hardly meet the requirements. Material with a thickness of 240 µm and 300 µm behave similar to each other and are both able to generate a signal above the qualification limit. Therefore samples with an active thickness of 200 µm are not further presented.

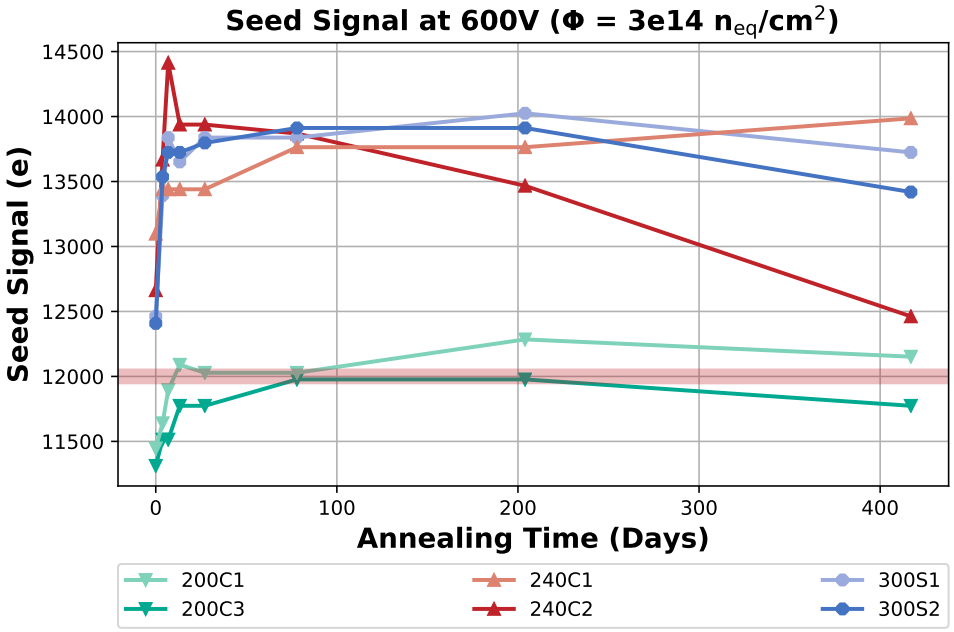

Figure 5.2.: Seed signal annealing behaviour of sensors with the three thicknesses in question. The signal of the 200 µm material is below the other materials and can hardly meet the requirement, indicated by a red line at 12 000 electrons.

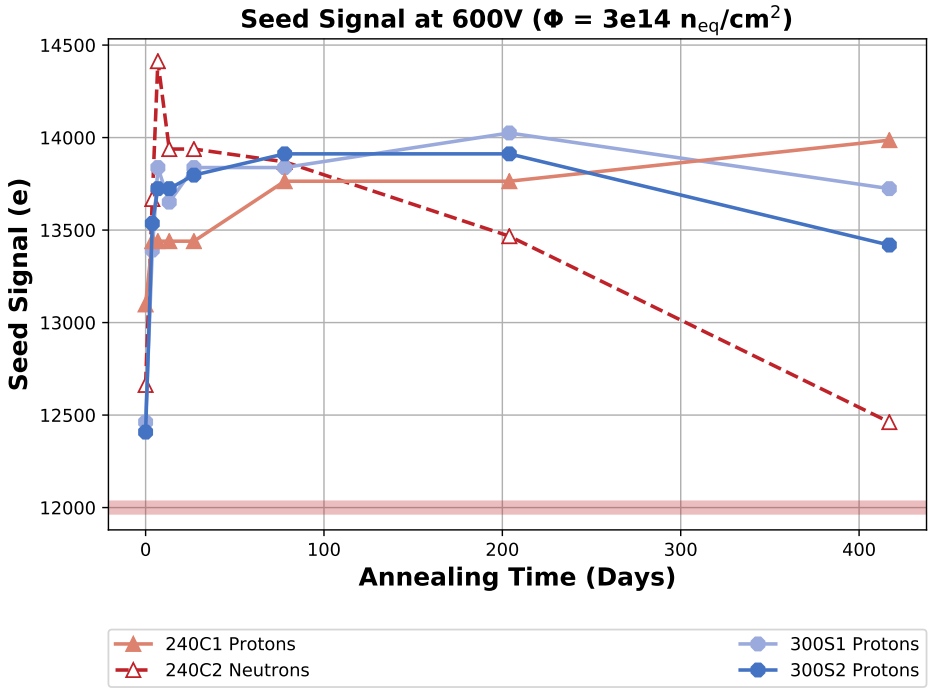

Figure 5.3.: Seed signal of sensors with an active thickness of 240 µm and 300 µm. The dashed line indicates one sensor irradiated with neutrons whereas the other three sensors were irradiated with protons. The neutron irradiated sensor shows the strongest reverse annealing.

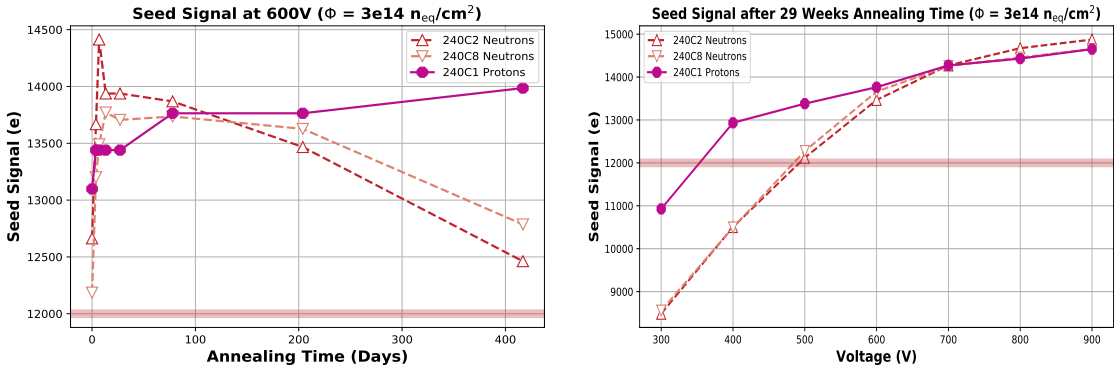

(a) (b)

Figure 5.4.: Annealing behaviour of 240 µm material irradiated with protons and neutrons (a). Neutron irradiated samples show a stronger reverse annealing. Voltage dependency of the signal after 29 weeks annealing (b). The proton irradiated sensor reaches the sufficiency region at an operating voltage 150 V less than neutron irradiated sensors.

A new visualisation of the signals from 240 and 300 µm material is presented in figure 5.3. Sensors of both thicknesses satisfy the requirements for all annealing conditions. For proton irradiation the signal of the 300 µm material drops slightly at high annealing times, where the 240C1 still shows beneficial annealing. In contrast, the 240C2 shows a significantly stronger reverse annealing. The different annealing characteristic can only stem from different irradiation particle types. Since the sensors were manufactured by the deep diffused technology, an oxygen enrichment is expected. Till now no difference in proton and neutron irradiation was observed (following the NIEL hypothesis) for sensors without oxygen enrichment. This leads to the assumption that the oxygen concentration may affect the annealing behaviour. However, more statistics is required in order to validate this hypothesis. Therefore it is further investigated in the following.

5.3. Neutron versus Proton Irradiation

Recent irradiation campaigns generated a large amount of data. However, the data often lacks comparability. The signal can be affected by many parameters: sensor type, operating voltage, annealing time, measurement procedure, fluence and thickness. Comparability is the key in order to acceptably visualise the differences of neutron and proton irradiation. Therefore it is attempted to verify the hypothesis of a stronger reverse annealing due to neutron irradiation by the best comparable data set available.

The annealing behaviour of three 240 µm thick sensors, which were all irradiated with a fluence of $\Phi \approx 3 \cdot 10^{14} \mathrm{n_{eq}/cm^2}$, are compared at the nominal operating voltage of 600 V in figure 5.4a. The two samples, marked with red dashed lines, were irradiated with neutrons and the purple continuous with protons. Contrary to the proton irradiated sample, the neutron irradiated sensors show strong reverse annealing. The voltage dependency at an annealing time of approximately 29 weeks (203 days) room temperature equivalent is presented in figure 5.4b. It is indicated that the proton irradiated sensor reaches higher signals in the lower voltage region till 600 V. The 12 000 electrons requirement is already satisfied at an operating voltage of 350 V which is about 150 V less than for neutron irradiated sensors. Above 600 V the signal dependency of the voltage is the same for proton and neutron irradiation in this case.

The annealing behaviour of sensors irradiated with a higher fluence of $\Phi = 6 \cdot 10^{14} \mathrm{n_{eq}/cm^2}$ is illustrated in figure 5.5a. This fluence respresents the most conservative approximation

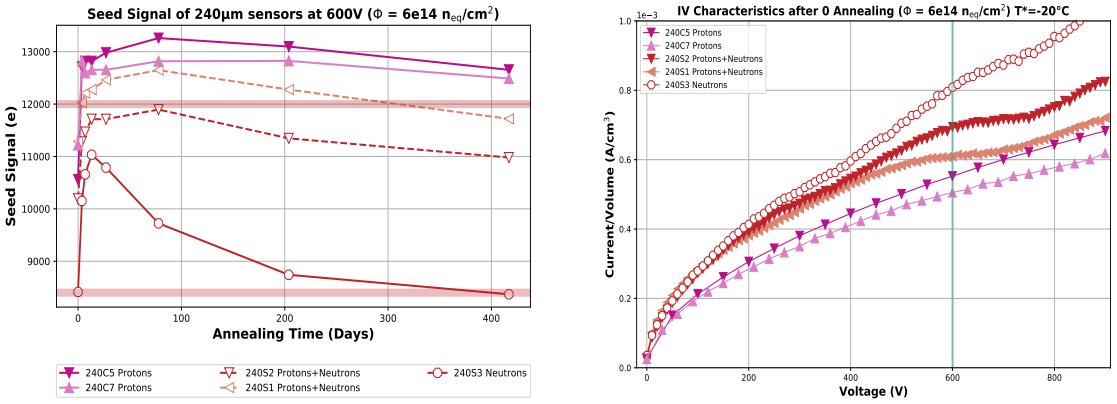

(a) (b)

Figure 5.5.: Annealing behaviour of 240 µm material at a fluence of $\Phi = 6 \cdot 10^{14} \mathrm{n_{eq}/cm^2}$ (a). A neutron fraction in the irradiation is indicated with hollow markers, pure irradiation with continuous lines. The hypothesis that neutron irradiation causes a stronger reverse annealing is visibly confirmed. The fan-out of the signal can be explained by a similar inverted fan-out of the leakage current (b). The vertical green line indicates the operating voltage of 600 V.

for the 2S region including 50% safety margin and 4000 $\mathrm{fb^{-1}}$ extension in respect to a potential run-time elongation of CMS. Sensors with pure proton irradiation are coloured in purple with filled markers. Hollow markers with red dashed lines indicate an irradiation with neutrons and protons with a fluence of $\Phi = 3 \cdot 10^{14} \mathrm{n_{eq}/cm^2}$ each. The red continuous line represents the only 240 µm thick sensor irradiated with pure neutrons. A fluence of $\Phi = 6 \cdot 10^{14} \mathrm{n_{eq}/cm^2}$ is expected for strip sensors of the PS region (PS-s). The rule of thumb MPV $> 12\sigma_{\mathrm{readout}}$ can be applied, accordingly. With the noise of the respective read-out chip SSA[1], it yields an efficiency margin around 8 400 electrons. Sensors irradiated with a higher neutron fraction show a stronger reverse annealing, consistent with the hypothesis. However, an overall fan-out of the signals is visible, independent of the annealing behaviour. A possible explanantion would be a different fluence. All samples were demanded to be irradiated with $\Phi = 6 \cdot 10^{14} \mathrm{n_{eq}/cm^2}$ but no reference measurements are available. Since the leakage current scales linearly with the fluence, it could be used as a tool to estimate differences in the fluences. The according leakage current directly after irradiation is presented in figure 5.5b with the same colour code and marker shape. A vertical green line indicates the corresponding operating voltage of 600 V. The fan-out occurs in a similar manner but inverted, since the signal drops with the fluence and the leakage current increases. For the two proton irradiated sensors the order is reversed, but the signal and the leakage current are not significantly different. Therefore different fluences are a possible explanation. Nevertheless, it is not possible to directly refer quantitatively from the leakage current to an expected signal. Moreover, slightly different uncontrolled annealing strongly affects the leakage current at this annealing stage and sensors might be not fully depleted yet at 600 V.

A comparison of 240 µm and 300 µm material as well as neutron and proton irradiation is presented in figure 5.6a at 600 V. This finally illustrates that the thicker 300 µm has a stronger reverse annealing than the 240 µm material but at the same time neutron irradiation leads to a higher reverse annealing as well. The sensor 300S6 was irradiated with a slightly lower fluence of $\Phi = 5 \cdot 10^{14} \mathrm{n_{eq}/cm^2}$ neutrons, wherefore the signal in the beneficial annealing region is higher than the others. Since 300 µm sensors are not fully

[1]SSA: **S**hort **S**trip **A**SIC

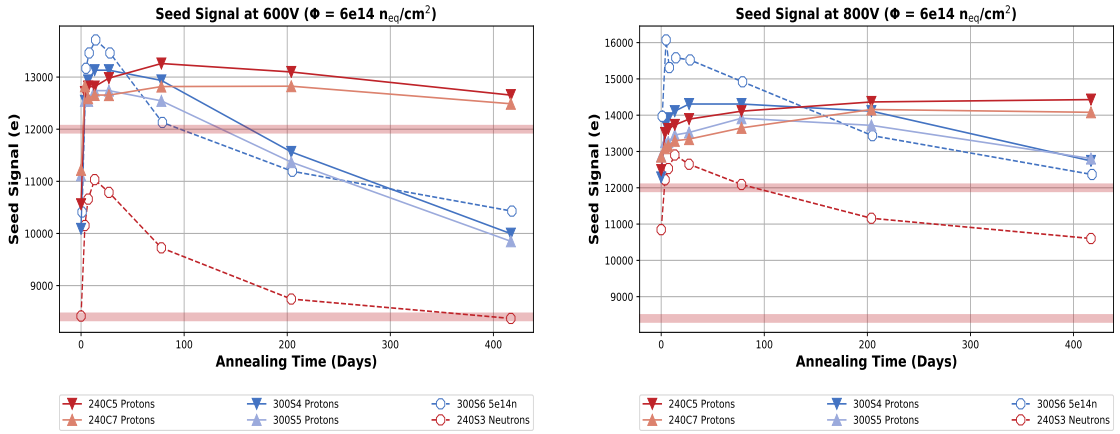

(a) (b)

Figure 5.6.: Annealing behaviour of 240 µm and 300 µm material for proton and neutron irradiation at 600 V (a). The higher operating voltage of 800 V (b) leads to a significant boost of the signal.

depleted at $\Phi = 6 \cdot 10^{14} \mathrm{n_{eq}/cm^2}$ and 600 V, the signal boost with 800 V is presented in figure 5.6b. The stronger reverse annealing due to neutron irradiation is better visible as well.

5.4. Neutrons vs Protons of n-type Strip Sensors

The investigation of deep diffused n-in-p sensors with active thicknesses of 240 µm and 300 µm indicated a difference in the annealing behaviour of the signal. Besides a higher reverse annealing of the thicker material, neutron irradiated samples tend to have a stronger annealing behaviour than proton irradiated sensors. This was further validated with all available data. However, the available data was obtained under varying frame conditions and is usually not comparable. The assumption is that oxygen enrichment in the deep diffused material causes an annealing behaviour dependency on the particle type. A new irradiation study was started with samples of the NitroStrip campaign[2] to further investigate the annealing behaviour of different material types. The samples of the NitroStrip campaign are n-type, wherefore the signal is expected to be less than the recently presented signals. Used material types with their respective oxygen concentration and the deep diffsued material for comparison are presented in tabular 5.1. The magnetic Czochralski material (MCZ) has the highest oxygen concentration, but also diffusion oxygenated float zone (DOFZ) and the deep diffused (DD) material are oxygen enriched of a similar amount. Only the float zone (FZ) material has a significantly lower oxygen concentration. Therefore, if the hypothesis that the oxygen concentration affects the annealing behaviour is valid, the float zone material is expected to behave different than diffusion oxygenated and magnetic Czochralski material.

5.4.1. Pure Irradiations

This part focusses on sensors irradiated with a fluence of $\Phi = 6 \cdot 10^{14} \mathrm{n_{eq}/cm^2}$ pure protons and neutrons. Measurements are performed at a temperature of $\mathrm{T} \approx -20°\mathrm{C}$ and the signal is presented for 800 V operating voltage. This operating voltage is necessary to provide a sufficient signal with n-type material. The annealing behaviour of MCZ material is

[2] Charge collection irradiation study of different materials [RD5]

Table 5.1.: Oxygen concentrations of the four materials investigated within signal studies [Pel+05].

Material	Label	Oxygen ($1/\mathrm{cm}^3$)
Diffusion oxygenated float zone	DOFZ	$1.7 \cdot 10^{17}$
magnetic Czochralski	MCZ	$4.6 \cdot 10^{17}$
Float zone	FZ	$< 9 \cdot 10^{15}$
Deep diffused	DD	$\approx 10^{17}$

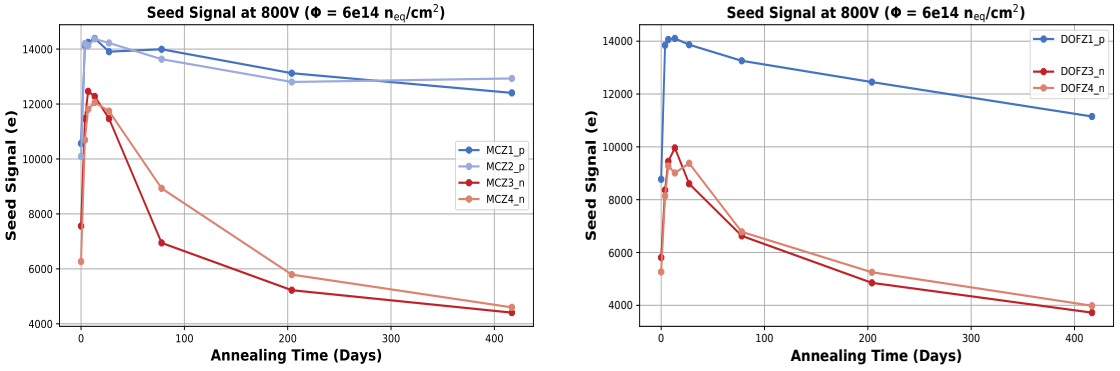

(a) (b)

Figure 5.7.: Annealing behaviour of magnetic Czochralski (a) and diffusion oxygenated float zone material (b). Proton irradiated sensors are indicated in blue, neutron irradiated sensors in red. Neutron irradiation causes a stronger reverse annealing for both materials. Additionally, a signal offset between neutron and proton irradiation occurs.

illustrated in figure 5.7a. Proton irradiated sensors (blue) have significantly less reverse annealing than neutron irradiated samples. Moreover, a signal offset between the two particle types is visible. The annealing behaviour of DOFZ silicon sensors is displayed in figure 5.7b. Similar to magnetic Czochralski material, the neutron irradiated sensors show a stronger reverse annealing than the proton irradiated sensor. A signal offset is visible as well.

The corresponding CV characteristics of the sensors presented in figure 5.7a and 5.7b are displayed in figure 5.8. Proton irradiated sensors are again coloured in blue and neutron irradiated samples in red. On the left side (a), for the magnetic Czochralski material, the saturation of $1/\mathrm{C}^2$ is visible for the proton irradiated sensors. The depletion voltage is at roughly 800 V. However, for the neutron irradiated samples no saturation is visible. A lower depletion voltage of the proton irradiated sensors supports the result of the signal measurement, although the full annealing behaviour cannot be explained by it. Similarly, for diffusion oxygenated material, the neutron irradiated sensors are not depleted up to a bias voltage of 1000 V. The proton irradiated sensors deplete at 1000 V. Therefore it is again consistent with the expectations.

So far the hypothesis that oxygen enrichment leads to a suppressed reverse annealing in a proton irradiation environment is validated. The annealing behaviour of float zone material, whose oxygen concentration is significantly below the other materials is presented in figure 5.9a. Again, proton irradiated sensors are coloured in blue and neutron irradiated samples in red. The signal of the FZ1 is slightly higher than the others but no significant difference between neutron and proton irradiation occurs. Irradiation with both particle types cause a similarly strong annealing behaviour than for neutron irradiated magnetic

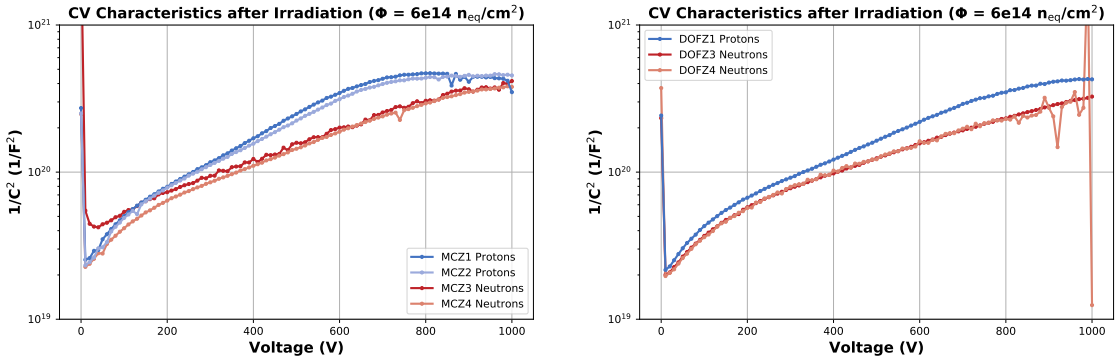

(a) (b)

Figure 5.8.: CV characteristics for magnetic Czochralski (a) and diffusion oxygenated (b) material dependent on the particle type. Proton irradiation leads to a lower depletion voltage which is consistent with signal measurements.

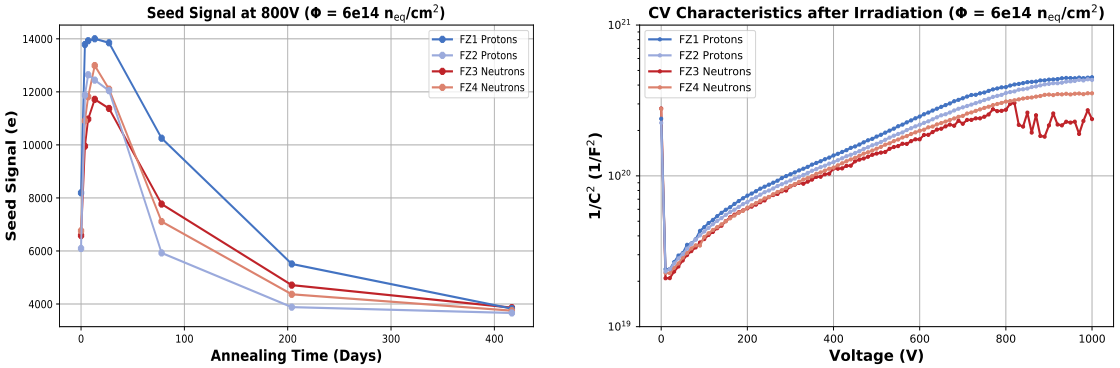

(a) (b)

Figure 5.9.: Seed signal of float zone silicon sensors (a) for pure proton (blue) and neutron (red) irradiation. No significant difference occurs in the annealing behaviour of all four samples. CV characteristics of float zone silicon sensors (b) after pure proton (blue) and neutron (red) irradiation. The depletion voltage is not dependent on the particle type of the irradiation.

Czochralski or diffusion oxygenated float zone silicon sensors. Therefore the conclusion is that oxygen enrichment of silicon strip sensors leads to a suppressed reverse annealing behaviour for proton irradiation. A corresponding visualisation of the CV characteristics is presented in figure 5.9b. The curves tend to saturate at rougly 1000 V operating voltage, which is not clearly visible. However, there is no difference in proton or neutron irradiation as expected.

5.4.2. Mixed Irradiation

CV characteristics

The CV characteristics of three HPK sensors are displayed in figure 5.10. They were irradiated with $\Phi = 3 \cdot 10^{14} \mathrm{n_{eq}/cm^2}$ neutrons which results in the curves marked with dark colours. After further irradiating with $\Phi = 3 \cdot 10^{14} \mathrm{n_{eq}/cm^2}$ protons, the depletion voltage stays unchanged. This is a significant disagreement with the expectations due to the NIEL hypothesis. Irradiating two times with the same fluence should give the same result as irradiating one time with the total fluence. This behaviour was further investigated within the irradiation campaign. All samples were irradiated with a fluence

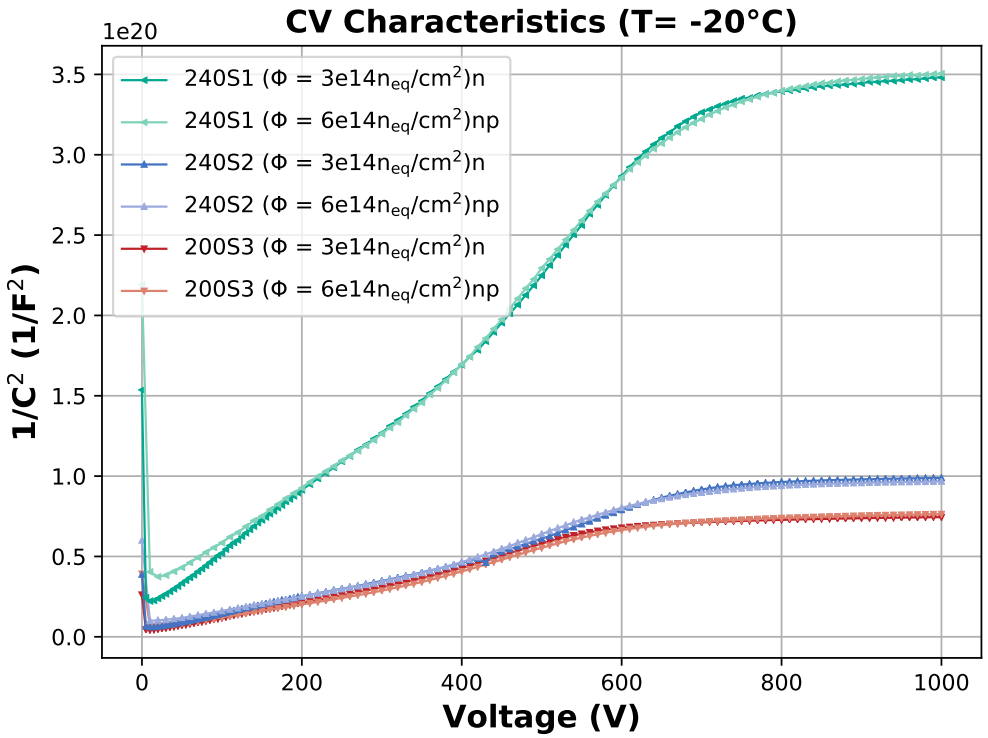

Figure 5.10.: CV characteristics of deep diffused material. The depletion voltage reaches a certain value after the first irradiation. Further irradiating with the same fluence of protons did not change the depletion voltage anymore. Moreover the CV characteristic itself is unchanged.

of $\Phi = 6 \cdot 10^{14} \mathrm{n_{eq}/cm^2}$ in total. For each material type two sensors were irradiated with $\Phi = 3 \cdot 10^{14} \mathrm{n_{eq}/cm^2}$ protons and with $\Phi = 3 \cdot 10^{14} \mathrm{n_{eq}/cm^2}$ neutrons afterwards. Additionally, two sensors per material type were irradiated first with $\Phi = 3 \cdot 10^{14} \mathrm{n_{eq}/cm^2}$ neutrons and afterwards with $\Phi = 3 \cdot 10^{14} \mathrm{n_{eq}/cm^2}$ protons. The result for magnetic Czochralski material is visualised in figure 5.11. On the left side the samples were irradiated with protons first and afterwards with neutron. The increase of the depletion voltage is visible after the second irradiation with light red and blue for the two sensors. This represents the expected behaviour of the depletion voltage scaling with fluence. However, on the right side the sensors were irradiated with protons after the neutron irradiation, which leads to an unchanged depletion voltage. In principle the depletion voltage is even decreasing, but it is just a slight effect. Therefore for the magnetic Czochralski material the irradiation sequence is of significant importance.

Similar measurement were performed for diffusion oxygenated float zone material. The results are presented in figure 5.12. Again the depletion voltage after the second irradiation is significantly dependent on the irradiation order. Although the curve is fluctuating a bit more after the second irradiation on the right side, a slight decrease in the depletion voltage is visible. The irradiation order is therefore crucial for diffusion oxygenated float zone material as well.

The CV characteristics of standard float zone material are presented in figure 5.13. On the left side the two samples were irradiated again first with protons and afterwards with neutrons, which leads to a visible increase in the depletion voltage. The irradiation order neutron before proton irradiation results in an unchanged depletion voltage. It slightly decreases similar to magnetic Czochralski and diffusion oxygenated float zone material.

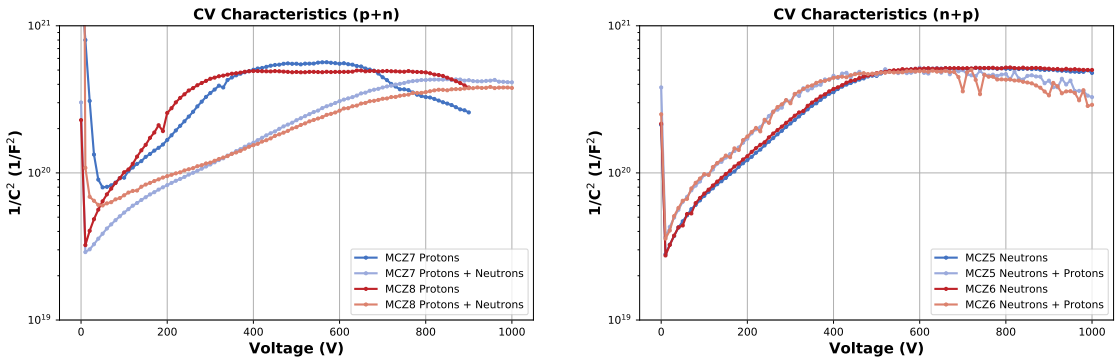

(a) (b)

Figure 5.11.: CV characteristics of magnetic Czochralski material for proton with additional neutron irradiation (a) and for proton after neutron irradiation (b). The evolution of the depletion voltage is affected by the irradiation order.

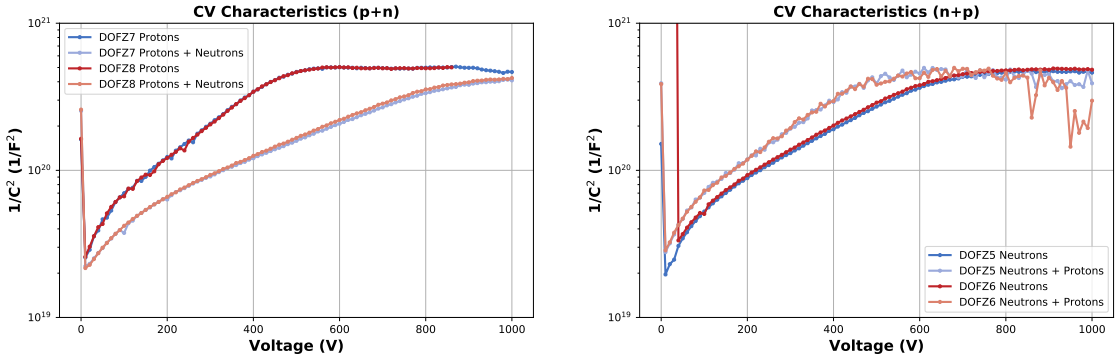

(a) (b)

Figure 5.12.: CV characteristics of diffusion oxygenated float zone material for proton with additional neutron irradiation (a) and for proton after neutron irradiation (b). The evolution of the depletion voltage is affected by the irradiation order.

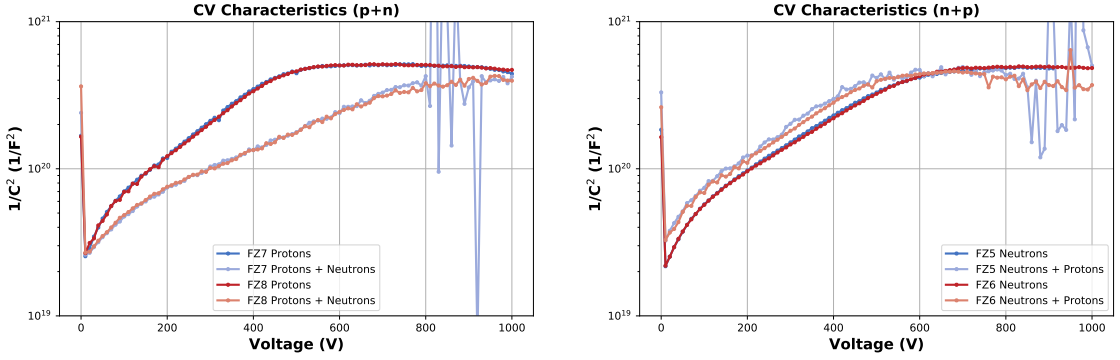

(a) (b)

Figure 5.13.: CV characteristics of float zone material for proton with additional neutron irradiation (a) and for proton after neutron irradiation (b). The evolution of the depletion voltage is affected by the irradiation order.

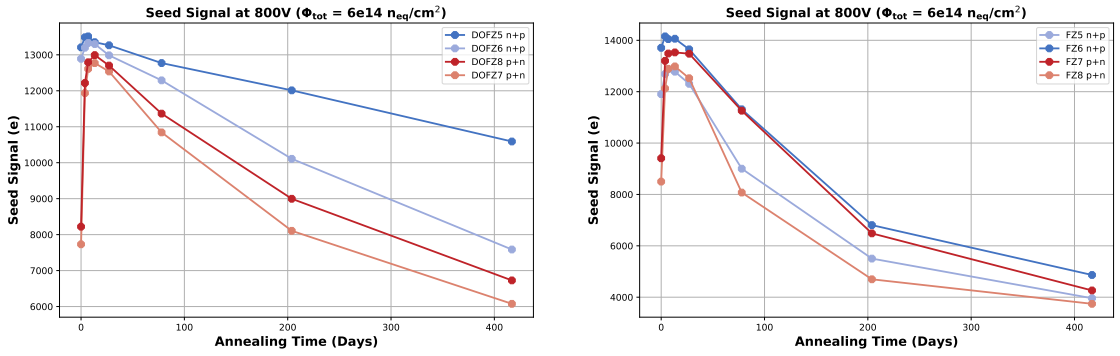

(a) (b)

Figure 5.14.: Signal annealing behaviour of diffusion oxygenated float zone (a) and standard float zone (b) material. The float zone material behaves similar.

Signal Behaviour

Seed signal measurements were performed additional to the CV measurements of mixed irradiated samples. The annealing behaviour at 800 V operating voltage of diffusion oxygenated float zone is presented in figure 5.14a. Sensors irradiated by neutron first and protons afterwards are indicated with blue. Compensation effects were visible for those sensors in the CV characteristics. The inverted irradiation order is indicated with red lines. The sensor DOFZ5 shows less reverse annealing than the others. In figure 5.14b the signal of float zone material is illustrated with the same frame conditions. No significant difference in the annealing behaviour is visible as well. This result is unexpected compared to the CV characteristics, since a different depletion voltage was indicated dependent on the irradiation order. Nevertheless, an offset in the signals is visible without annealing, which would satisfy the expectations due to the CV characteristics.

The voltage dependency of the signal is presented before annealing in figure 5.15a. A significant difference in the signals is visible, consistent with the CV measurements. The irradiation order neutrons before protons leads to a lower depletion voltage and also a higher signal at a certain voltage. The compensation effects are not dominant anymore after annealing as indicated in figure 5.15b. Any differences in the signal dependent on the voltage vanished.

The signals dependency on the bias voltage without annealing for float zone material is presented in figure 5.16a. A difference in the signal is indicated by the sensor FZ6, but the behaviour of FZ5 is somewhere in between the other three. After an annealing time of 14 days room temperature equivalent any difference vanished as visualised in figure 5.16b. It is also indicated that the sensor FZ5 has generally less signal than the others at operating voltages below 600 V. This could explain the behaviour in figure 5.16a. Nevertheless, the results of the signal measurements are consistent with the expectations due to the CV characteristics. Vanishing compensation effects can be observed just like they were for the diffusion oxygenated float zone material.

The annealing behaviour of float zone material for pure irradiation compared to mixed irradiation is displayed in figure 5.17a. The data show a relatively high spread, but all in all no significant difference occurs. The same comparison for the diffusion oxygenated float zone material is presented in figure 5.17b. It is indicated that the higher neutron fraction causes a higher reverse annealing. However, the sensor DOFZ5 which was irradiated with neutrons first and protons afterwards shows a similar annealing behaviour than the pure proton irradiated DOFZ1. Contrary to that, DOFZ6 shows a similar annealing behaviour than the samples irradiated by neutrons after proton irradiation.

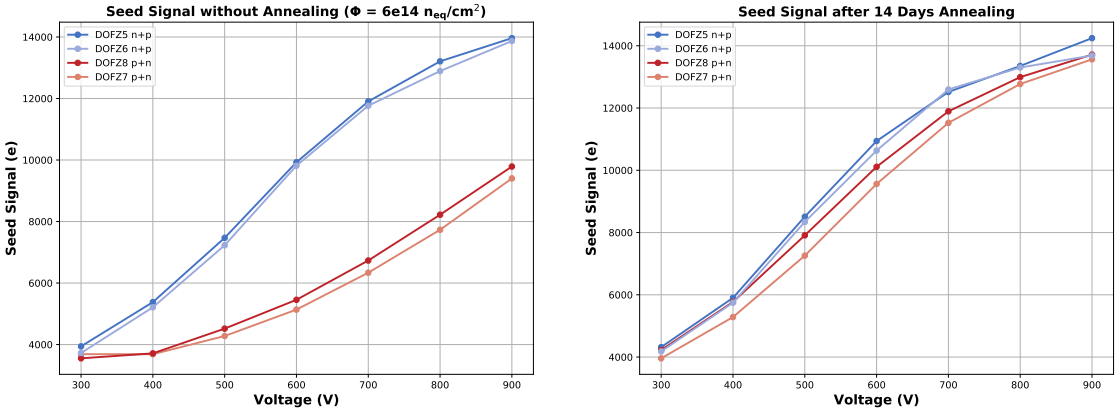

(a) (b)

Figure 5.15.: Voltage dependency of DOFZ material before (a) and after 14 days annealing (b). Without annealing the signal of sensors irradiated by neutrons first are stronger than the others. After annealing of 14 days the effect vanishes.

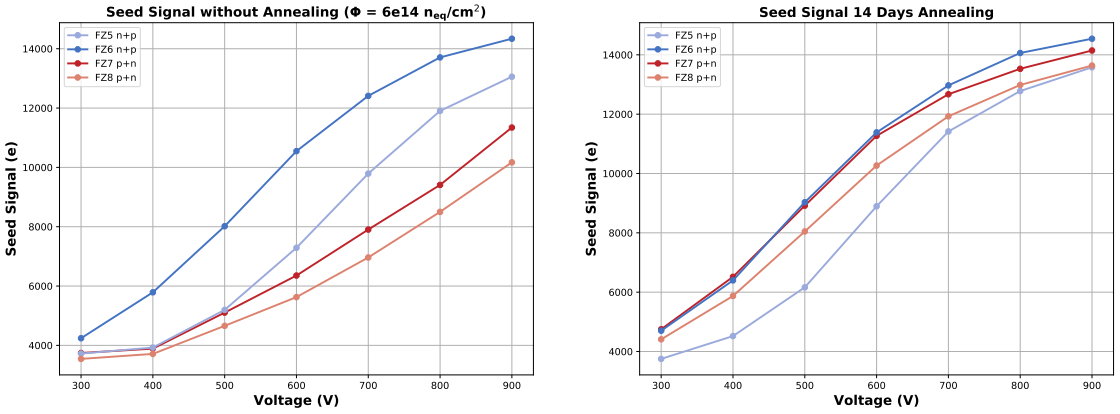

(a) (b)

Figure 5.16.: Voltage dependency of FZ material before (a) and after 14 days annealing time (b). The sensor FZ5 shows a higher signal than the others. The other sensor for the same irradiation order FZ6 has a lower signal.

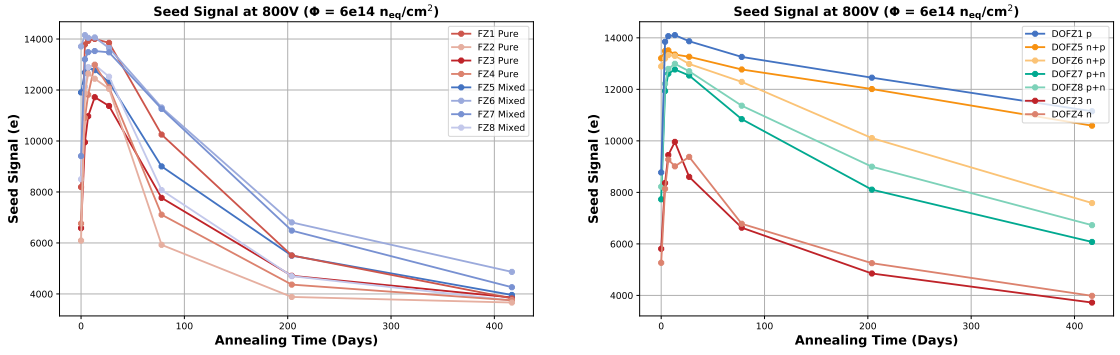

(a) (b)

Figure 5.17.: Mixed irradiation compared to pure irradiation for float zone (a) and diffusion oxygenated material (b). No difference occurs for the float zone material. By comparing the signals of diffusion oxygenated sensors, the differen impact of pure neutron and proton irradiation has to be taken into account.

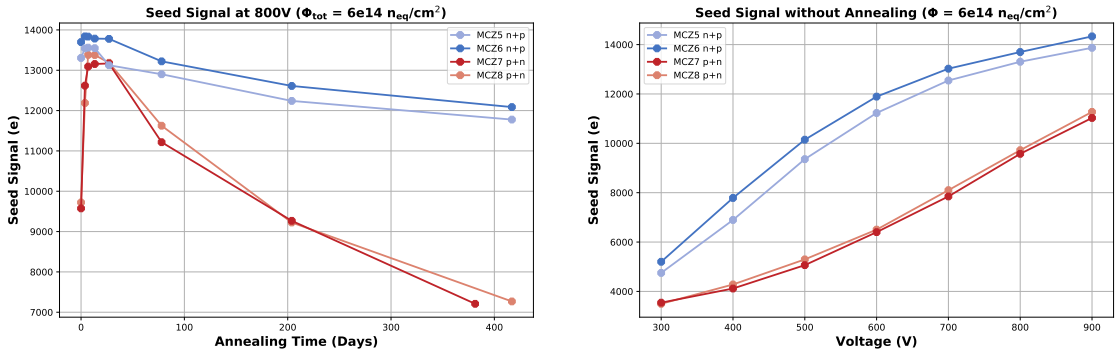

(a) (b)

Figure 5.18.: Annealing characteristics of magnetic Czochralski material in an mixed irradiation environment (a). Corresponding voltage dependency before annealing (b). The irradiation order protons after neutrons results in a higher signal.

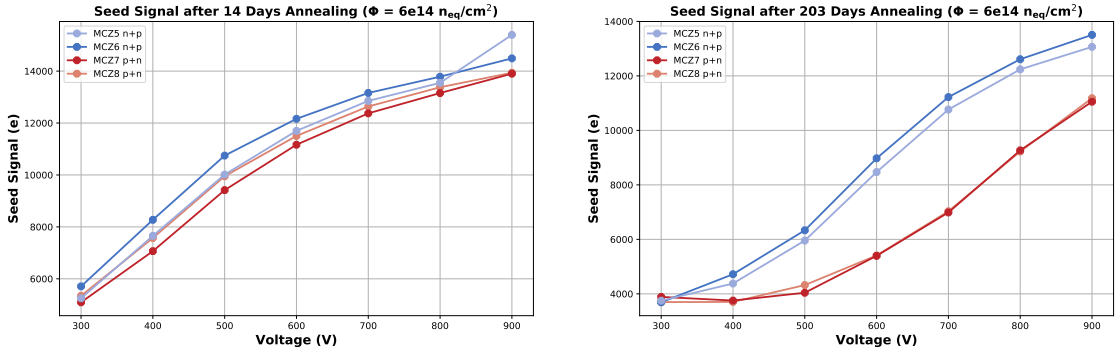

(a) (b)

Figure 5.19.: Seed signals voltage dependency for magnetic Czochralski material after 14 days (a) and 203 days (b) annealing time. After 14 days no difference for the irradiation order is visible, contrary to the behaviour after 203 days annealing.

The annealing behaviour for magnetic Czochralski material is presented in figure 5.18a dependent on the irradiation order. Contrary to the float zone material, a significant difference occurs. The irradiation order protons after neutrons led to a lower depletion voltage, visible in the CV characteristics and also in a less reverse annealing of the signal. Similiar to the other materials, the voltage dependency without annealing is displayed in figure 5.18b. The higher signal of the samples irradiated by protons after neutrons is visible. In figure 5.19a the signal is displayed for an annealing of 14 days over the operating voltage. The differences between the irradiation order vanished again. However, after further annealing to 203 days in total, illustrated in figure 5.19b, the samples which were irradiated with neutrons first are superior to the other samples.

5.5. Summary of Chapter 5

Studies of this chapter can be put in a nutshell as follows:

- The seed signal of sensors with 200, 240 and 300 µm active thickness was investigated regarding the 2S requirements in Phase-2.
- Samples of 240 µm and 300 µm thickness can both meet the 12 000 electron qualification limit.

- Moreover, a difference in the annealing behaviour after neutron and proton irradiation was observed.
- This led to the hypothesis that the annealing behaviour is dependent on the oxygen concentration.
- A suppressed reverse annealing was observed for proton irradiated oxygen enriched samples for n-type and p-type sensors.
- No difference was observed for float zone material which validates the hypothesis.
- The different effects were further supported by CV characteristics (depletion voltage).
- In mixed irradiations, compensation effects dependent on the irradiation sequence were indicated by CV characteristics of all materials.
- Those effects were supported by signal measurements before annealing but vanish after annealing for FZ material. On the other hand a different annealing behaviour was observed for magnetic Czochralski material.
- The impact and cause of this compensation effects is not fully understood yet.

6. Interplay of Surface and Bulk Damage

In n-in-p silicon strip sensors impurities or irradiation damage generate positively charged defects in the silicon oxide layer (surface). Those attract electrons from the bulk, which leads to the formation of an electron accumulation layer and decrease in the interstrip resistance. If the interstrip resistance falls below the critical value of approximately 100 times the bias resistance, strips are short-circuited which decreases the spatial resolution. An interstrip isolation structure is introduced to break the accumulation layer and provide a sufficient interstrip resistance before and after irradiation. Common structures are p-stop, p-spray, or p-common implants (see chapter 2.6.1).

Irradiation with x-rays generates mainly surface and negligible bulk damage since the energy is too low to create bulk defects. Proton and neutron irradiation mainly induces bulk defects. Since protons are charged particles, they also induce charges in the surface. In fact, neutron irradiation also causes surface defects due to gamma background in the radiation inside a spallation reactor. Therefore irradiation with all particle types induces positive oxide charges and the interstrip resistance (R_{int}) is expected to be lost without any strip isolation structure [Dal+14].

On the other hand, an unexpected high interstrip resistance was observed for proton irradiated n-in-p sensors without an isolating implant. There were attempts to simulate and explain the situation. By introducing bulk defects, electrons are trapped near the surface, where an effective negative charge is built up. This fixed negative charge compensates the positive oxide charge in the surface, which leads to a suppression of the electron accumulation layer. A comparison of simulated radiation damage by protons to sensors with a usual p-stop implant is shown in figure 6.1. The interstrip resistance is plotted over the bias voltage for different positive oxide charge concentrations Q_F. On the left side a usual p-stop isolation structure is used. For the right side no isolation implant is implemented. No significant difference in the interstrip resistance can be observed at the fluence of $1 \cdot 10^{15} n_{eq}/cm^2$. Therefore the bulk defects of the proton irradiation are able to preserve a similar interstrip resistance than the p-stop implant. However, a sufficient isolation cannot be reached in both cases for $Q_F > 1.2 \cdot 10^{12} cm^{-2}$ [Dal+14].

A new irradiation study was started to further investiage the impact of irradiation on the interstrip resistance and possible compensation effects by bulk defects. In order to do so, sensors without any interstrip isolation structure of the 'No_Pstop' design were used. The nomenclature for plots are shortened with 'NPX', where X is the number of the sensor, for example NP4. A full list of used sensors with their corresponding abbreviation can be

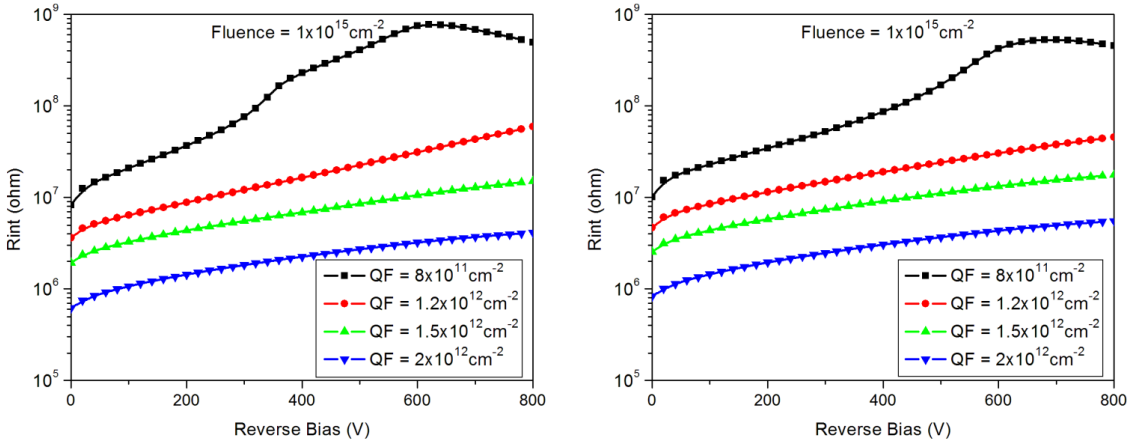

Figure 6.1.: Simulated interstrip resistance over bias voltage dependent on the positive oxide charge. On the left side a usual p-stop structure is used. The right side shows the interstrip resistance without any isolation structure. After a fluence of 1e15 n_{eq}/cm^2 the resistances scale similarly, which is explainable by compensation effects of bulk defects [Dal+14].

found in D.4. The sensors stem from the 2S wafers of the HPK campaigns. Irradiation with x-rays, neutrons and protons were performed as well as mixed irradiation of neutrons and x-rays. The following questions are the basis of this study:

- Is the interstrip resistance sufficient before irradiation?
- In general, how does it depend on the bias voltage?
- If it is sufficient before irradiation, for which irradiation does it become insufficient?
- What is the temperature dependency?
- How much does annealing affect the strip isolation?
- If compensation effects are visible, are they strong enough to preserve the interstrip isolation?
- Is there a difference in the compensation effects of neutron and proton irradiation?

6.1. X-Ray Tube Characterisation

A characterisation of the x-ray tube is required in order to calibrate the irradiation procedure. The beamspot was scanned with a pin-diode[1] on a moveable xy-table. A collimator with 1.5 mm diameter was placed above the diode to increase the resolution. While moving to scan the profile shape in 1 mm steps, the current was read out. Before every measurement, the dark current was taken and subtracted from the measured current afterwards. The conversion factors of the diode current into equivalent dose are calculated by a Geant4 simulation [Gut+12].

The beamspot profiles for 60 kV tube voltage, 30 mA tube current and a vanadium filter are shown in figure 6.2. On the left side the profile map was scanned at 100 mm distance away from the opening window (with a collimator) of the x-ray tube. This tube voltage, current, filter and distance is a typical configuration which is used for the measurement procedure. The maximum dose is approximately 11900 Gy/h and the mean value roughly 8830 Gy/h. Data points with a dose $D < D_{Max}/3$ are excluded to avoid that the regions

[1] **pin**: **p**ositive **i**ntrinsic **n**egative

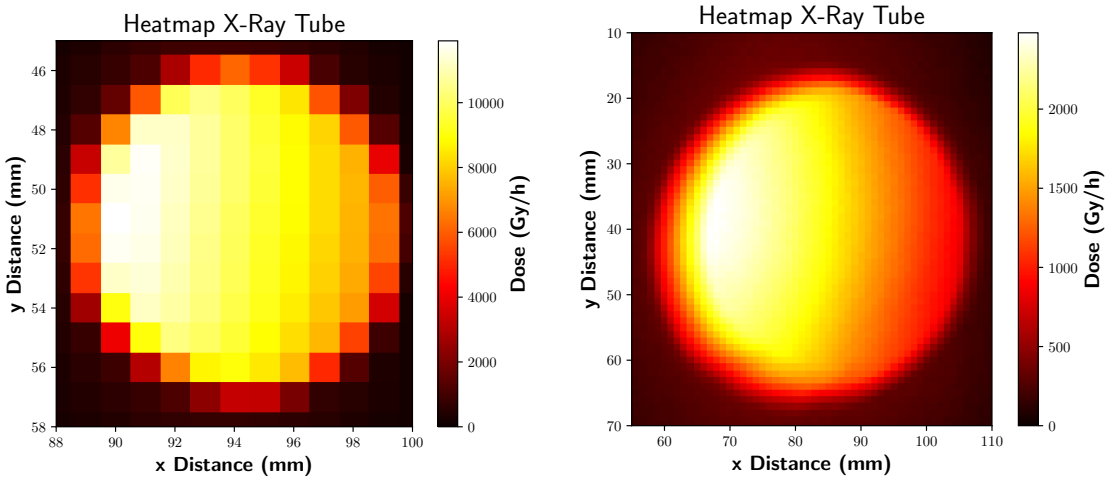

(a) (b)

Figure 6.2.: Beamspot profile for 60 kV tube voltage and 30 mA current with a vanadium filter. On the left side at the distance of 100 mm for practical use. On the right side at a distance of 300 mm, where the beamspots area is increased. The shape is inhomogeneous, wherefore a scanning procedure is required to provide homogeneous irradiation.

outside of the beamspot distort the mean calculation. On the right side the collimator of the x-ray opening window was removed and the distance was increased to 300 mm. This leads to a larger beamspot and a higher relative resolution, which results in a better visibility of the inhomogeneity. Three dimensional illustrations of both profiles can be found in D.4.

In figure 6.2a the inhomogeneity is visible in the x direction. For a fixed x value the y dependency seems to be constant within the beamspot. A cross section of the dose rate as a function of the x and y position is shown in figure 6.3. For figure 6.3a the cut is at $x \approx 94$ mm. The dose is nearly constant inside the beamspot and drops rapidly at the border. A cut through the y-axis at $y = 51$ mm is displayed in 6.3b. Inside the beamspot the dose scales approximately linearly with the x distance. A similar behaviour occurs for the increased distance. According plots can be found in D.3. To eliminate systematic errors in the measurement procedure, a set of tests were performed:

- Altering the tube voltage and current
- The scanning procedure was reversed in order to check for saturation effects inside the diode
- Altering the diode voltage to ensure depletion
- A potential tilt of the diode collimator was evaluated by altering the diodes orientation

None of those tests provide an explanation for the inhomogeneous beamspot profile. A similar x-ray tube was used at CERN. The characterisation of it yielded an inhomogeneous beamspot profile as well [CER17]. This supports the assumption that the inhomogeneity is caused by the x-ray tube itself and is not an artefact due to the measurement procedure. In order to maintain a homogeneous irradiation profile, the sample is moved through the beamspot in a meander-like pattern.

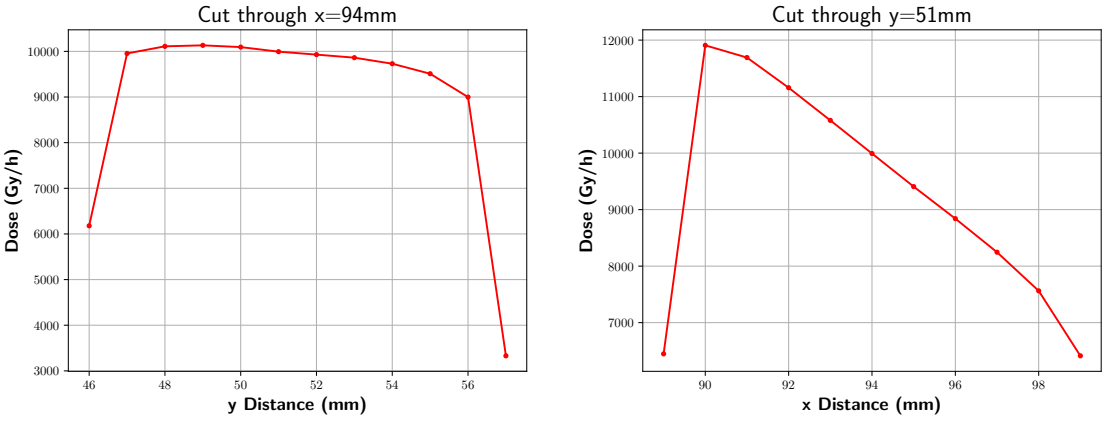

(a) (b)

Figure 6.3.: Cut through the x-axis in the middle of the beamspot on the left side. The profile is nearly homogeneous. The cut through the y-axis on the right side indicates the inhomogeneity of the profile in the x direction. The dose decreases linearly within the beamspot. This inhomogeneity is not negligible for irradiation procedures.

6.2. Measurement Procedure

The study incorporates measurements of the interstrip resistance and interstrip capacitance as well as IV characteristics of the sensor. A normalised quantity is used to compare the interstrip parameters of sensors with different strip lengths. Since the capacity scales linearly with the strip length, it is divided by it to cancel the dependence out. The interstrip resistance is multiplied by the strip length, since it scales inversely proportional with it. Although the interstrip capacitance is not expected to change due to irradiation, it is a good tool to monitore the needle contact while measuring the interstrip resistance. The normalised interstrip capacitance is in the order of 0.5 pF/cm. Insufficient contact results in a value below 0.01 pF/cm.

The standard interstrip resistance measurement is performed by applying a low voltage ramp between two neighboring strips, from 0 V to 1 V. The inverse slope of the interstrip current plotted over the voltage yields the interstrip resistance. Such a low voltage ramp is done for every bias voltage step on several strips. For the analysis one datapoint represents the mean of five to ten strips. If strip measurements are identified as corrupted, e.g. indicated by interstrip capacitance measurements, the strips are excluded from the analysis. Additional to the low voltage ramp, a bias voltage ramp is also performed to get the dependence of the interstrip resistance on the operating voltage.

A neutron or proton irradiated sensor shows an increased leakage current due to bulk damage. This current flows through all strips. When the low voltage ramp is performed, this current is additionally induced to the leakage current. A typical leakage current after irradiation with a fluence of $\Phi = 6 \cdot 10^{14}\,\mathrm{n_{eq}/cm^2}$ is in the region of $I_{\mathrm{leak}} \approx 10^{-7}\,\mathrm{A}$. If the interstrip resistance is in the region of 100 MΩ, applying 1 V between two strips would result in an induced current of $I_{\mathrm{int}} = 10^{-8}\,\mathrm{A}$. Therefore if the leakage current significantly exceeds the interstrip current, visible fluctuations may occur. A higher voltage ramp to 10 V was tested, to avoid that the interstrip current disappears in leakage current. The difference of measurements with both ramps is indicated in figure 6.4. The 1 V and 10 V low voltage ramp are performed to measure the interstrip resistance of a sensor, irradiated with protons of $\Phi = 6 \cdot 10^{14}\,\mathrm{n_{eq}/cm^2}$. The ratio of leakage current to interstrip current increases with increasing bias voltage, which leads to fluctuations of the measurement with

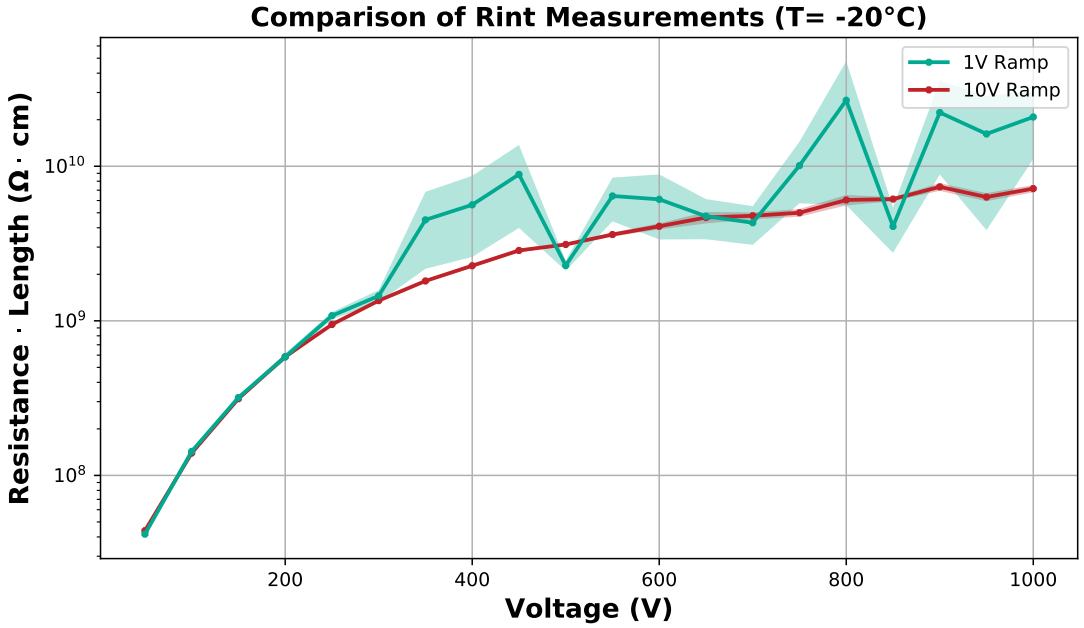

Figure 6.4.: Comparaison of 1 V and 10 V low voltage ramps for the interstrip resistance measurement procedure. Till 300 V no difference is visible. At higher bias voltages the 1 V ramp measurements start to fluctuate due to leakage current fluctuations in the magnitude of the low voltage induced current.

a 1 V ramp above 300 V. In contrast, the 10 V ramp is able to induce a sufficient interstrip current to keep fluctuations reasonable. No difference between the two ramps is visible for voltages below 300 V, which legitimates the 10 V ramp.

6.3. Interstrip Properties Before Irradiation

The interstrip capacitance at an usual operating voltage of 300 V for ten sensors with a strip length of 1.45 cm is displayed in figure 6.5a. A red bar marks the region where the interstrip capacitance is expected. All sensors have a similar interstrip capacitance slightly below the expected value. The corresponding interstrip resistance at 300 V is presented in figure 6.5b. For the analysis the mean of five to ten strips was taken per data point. Marked with a green bar is the range of the bias resistance. The lower limit is marked with a red band. These two bands are the same for the following plots.

The dependence of the interstrip resistance on the bias voltage is presented in figure 6.6. A significant increase in the resistance is observed between 100 V and 150 V. Above 150 V it stays constant at a sufficient level independent of the bias voltage. From 0 V to 100 V the interstrip resistance rises exponentially from roughly $10^4\,\Omega$cm to $10^6\,\Omega$cm. Therefore below 100 V the interstrip isolation structure is insufficient. Simulations of the interstrip resistance without irradiation are illustrated in figure 6.7. On the left side a usual p-stop implant is implemented and on the right side no isolation structure is taken into account. Since no irradiation effects are existing, the impurities inside the oxide layer are the only cause of positive oxide charges (QF). Dependent on those, the interstrip resistance disappears for both structures at QF$= 5 \cdot 10^{11}/\mathrm{cm}^2$. With a p-stop implant a higher resistance is mainly achieved for low bias voltages. The measurement results are comparable to QF$= 5 \cdot 10^{10}/\mathrm{cm}^2$ and QF$= 1 \cdot 10^{11}/\mathrm{cm}^2$, where the shape is similar. However, for low bias voltages the simulated interstrip resistance is smaller than the measured resistance. The assumption is that the electron accumulation layer beneath

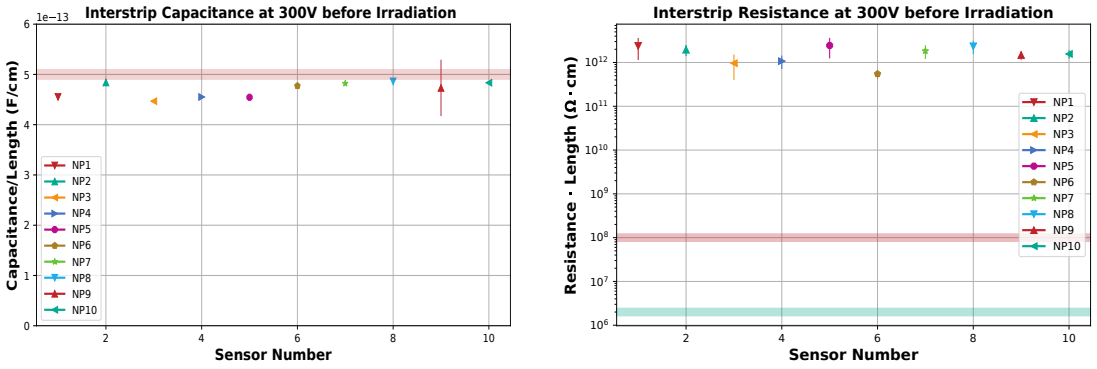

(a) (b)

Figure 6.5.: Interstrip capacitance before irradiation (a). Expected region is indicated with a red layer. Interstrip resistance at 300 V (b) compared to the bias resistor (green layer) and sufficiency region (red layer).

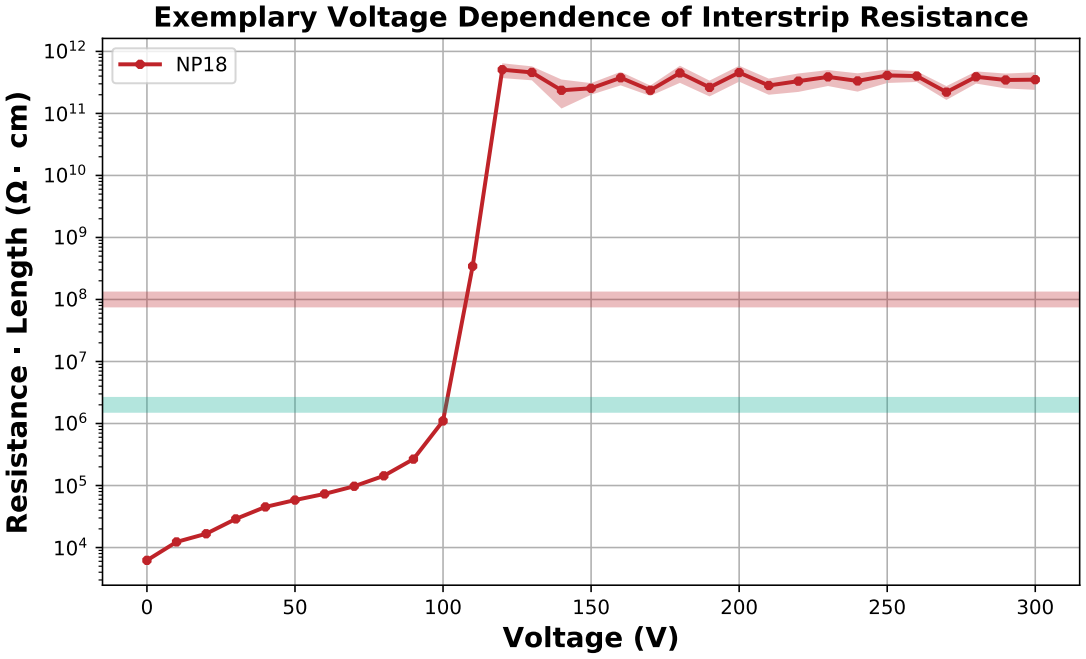

Figure 6.6.: Voltage dependency of the interstrip resistance before irradiation. A large increase in the resistance usually occurs between 100 and 150 V. Above 150 V the interstrip resistance is constant at a sufficient level. Below it is rising exponentially to 10^6 Ωcm where the isolation is insufficient to provide a spatial resolution.

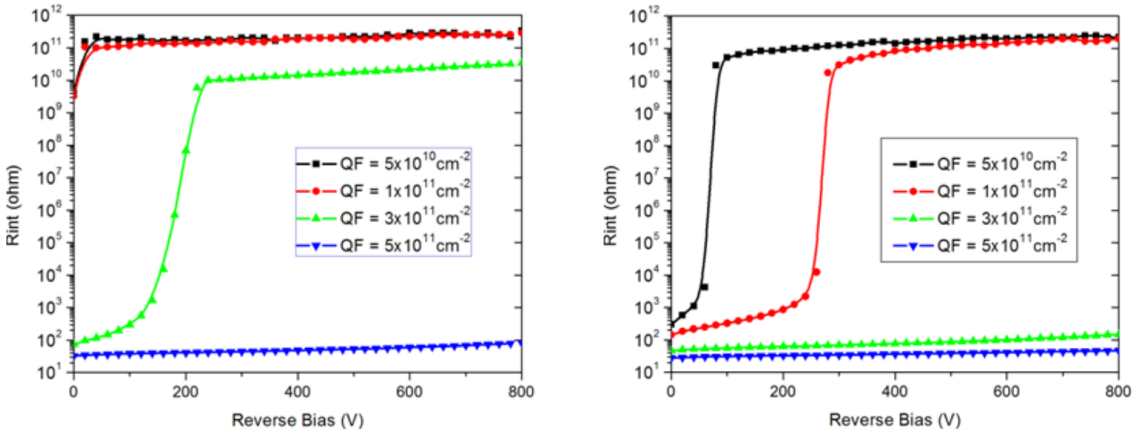

Figure 6.7.: Interstrip resistance before irradiation dependent on the positive oxide charge concentration QF. On the left side a typical p-stop isolation structure is implemented between the strips. On the right side no specific implant is used. The similarity between measurement data and simulations is most prominent for $\mathrm{QF} = 5 \cdot 10^{10}/\mathrm{cm}^2$ [Dal+14].

the strips is partially removed with an increasing electrical field. This layer is finally dismantled at a certain bias voltage which leads to a significantly increased interstrip resistance. Therefore for higher bias voltage the situation is not changing anymore, since the accumulation layer is already removed.

6.4. X-Ray Induced Surface Damage

An initial test was performed to investigate the general effect of x-rays on the interstrip resistance and the impact of annealing effects. The sensor NP6 was irradiated with 4 kGy x-rays. In figure 6.8a the red curve shows the interstrip resistance measured at T= 20°C. It scales exponentially and reaches the sufficiency region at 870 V. The sensor was then annealed for 80 minutes at 60°C (A1). After measuring the interstrip resistance the sensor was again annealed at the same temperature and for the same time (A2). Annealing leads to an increase of the resistance. The effect is less pronounced after the second annealing step.

The impact of x-ray irradiation on the interstrip resistance is displayed in figure 6.8b up to a dose of 2 kGy. Higher doses lead to a decreased resistance as expected. For 0.5 kGy it scales exponentially with bias voltage and starts to saturate above 400 V. The slope of the curves become flatter and the saturation voltage increases with increasing dose.

The interstrip resistance for higher doses is displayed in figure 6.9. Measurements were performed at T= 20°C and T= −20°C. The degeneration of the interstrip resistance saturates at 30 kGy. Only in the high voltage region a slight decrease is visible. At T= −20°C the sufficiency region of $10^8\,\Omega$cm is reached at 450 V. The behaviour of the resistance at T= 20°C is similar but with an offset of approximately one order of magnitude. Therefore it does not reach a sufficient region anymore, even for a bias voltage up to 1000 V.

6.5. Combination of Surface and Bulk Damage

Proton Irradiation

The interstrip resistance after irradiation with $6{\cdot}10^{14}\,\mathrm{n_{eq}}/\mathrm{cm}^2$ is displayed in figure 6.10a. For comparison the interstrip resistance before irradiation is illustrated as well. Fluctuations of the graph are occuring because the interstrip resistance measurements were

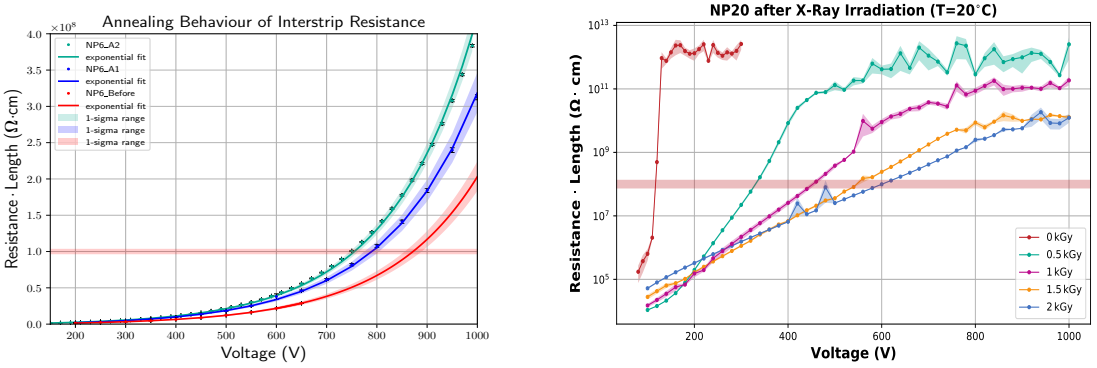

(a) (b)

Figure 6.8.: Interstrip resistance normalised by the strip length of a x-ray irradiated NP sensors with a dose of D ≈ 4kGy (a) without annealing (red), after annealing step A1 (blue) and further annealing A2 (green). The two annealing steps A1 and A2 lead to an increase in the interstrip resistance. Interstrip resistance after irradiation with x-rays in 0.5 kGy steps (b). For every step the resistance decreases and the sufficiency region is reached at higher voltages.

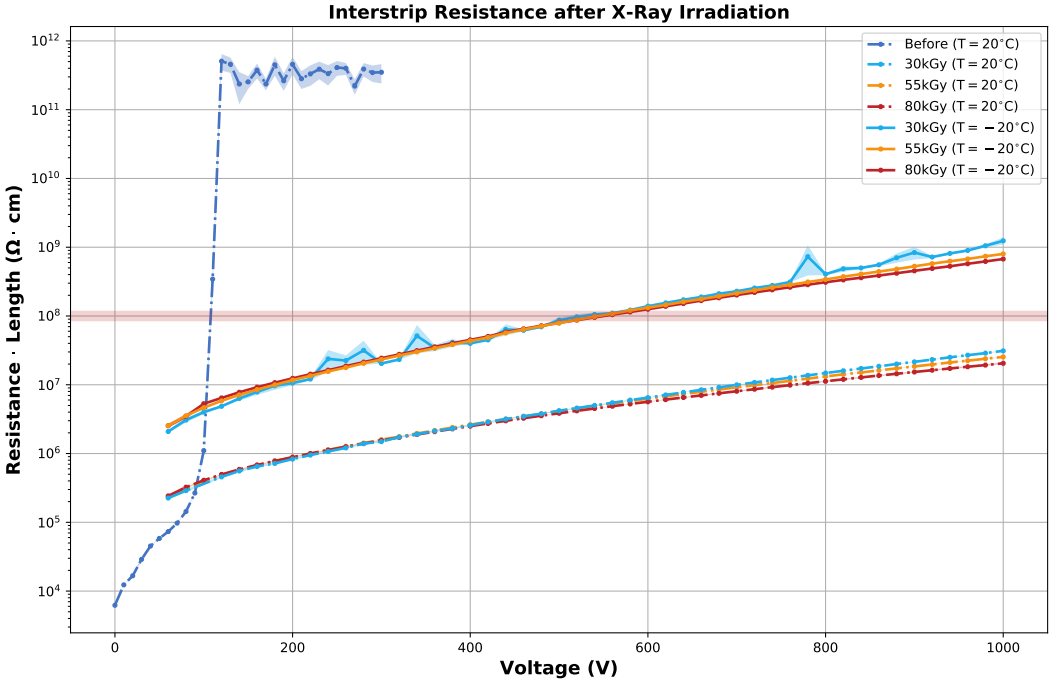

Figure 6.9.: NP sensor irradiated with pure x-rays. Dashed lines indicate measurements performed at T= 20°C, continuous lines at T= −20°C. Above 30 kGy the interstrip resistance is only changing for high bias voltages with further irradiation.

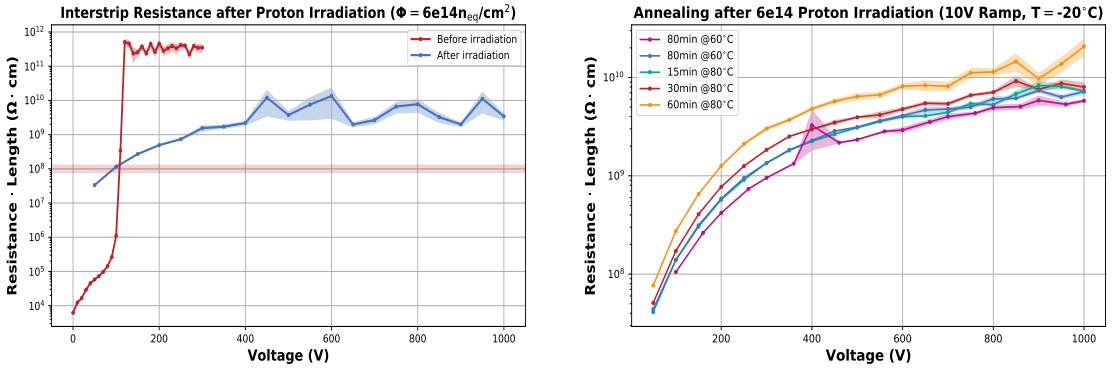

(a) (b)

Figure 6.10.: Interstrip resistance behaviour after $6{\cdot}10^{14}\,\mathrm{n_{eq}/cm^2}$ proton irradiation of a NP sensor. The sufficiency region is reached already at 100 V (a). Annealing is investigated in (b) for standard annealing steps similar to bulk annealing studies. The legend is ordered chronologically.

performed before the investigation of the 10 V ramp approach. The deposited dose inside the surface due to the proton irradiation is 900 kGy (calculated by [NISa]). Therefore, without taking compensation effects of the bulk damage into account, the interstrip resistance would be expected to be clearly below the sufficiency region for every bias voltage up to 1000 V. Contrary to the expectation, the interstrip resistance exceeds the minimum requirement already at 100 V. This results supports the assumption that compensation effects due to the bulk damage of proton irradiation occur.

Since it was observed that annealing affects surface defects, this behaviour was investigated as well. The usual annealing steps regarding signal studies (bulk annealing) were used to yield comparable results. This annealing dependence is presented in figure 6.10b. The legend is ordered chronologically so that the highest interstrip resistance in yellow belongs to a measurement after the last annealing step. Reverse annealing effects are not observerd. Measurements were performed using the 10 V ramp approach. The first two measurements after annealing are excluded from the plot, since they were measured with 1V ramps and show severe fluctuations.

Neutron Irradiation

Sensors were irradiated with neutrons of a fluence of $3{\cdot}10^{14}\,\mathrm{n_{eq}/cm^2}$ and $6{\cdot}10^{14}\,\mathrm{n_{eq}/cm^2}$. The expected dose is about 3 kGy and 6 kGy, respectively, due to impurities inside the spallation reactor [AZS17]. This dose is over a factor 100 lower than for proton irradiation (900 kGy). However, the interstrip resistance of neutron compared to proton irradiation is similar as illustrated in figure 6.11. Neutron irradiation is indicated in red and purple, proton irradiation in blue. The resistance of the $3{\cdot}10^{14}\,\mathrm{n_{eq}/cm^2}$ neutron irradiated and the $6{\cdot}10^{14}\,\mathrm{n_{eq}/cm^2}$ proton irradiated sensor is similar. Both reach the sufficiency region at 100 V bias voltage. After $6{\cdot}10^{14}\,\mathrm{n_{eq}/cm^2}$ neutron irradiation this region is reached at 50 V. Therefore the interstrip resistance is higher the more bulk defects are present. The saturation is similar for the three irradiations.

A comparison of the $3{\cdot}10^{14}\,\mathrm{n_{eq}/cm^2}$ neutron irradiated sample with additional x-ray irradiation to pure x-ray irradiation is presented in figure 6.12. The sensor was further irradiated with x-rays till 80 kGy. Above 55 kGy the interstrip resistance becomes constant and is no longer affected by increasing dose. Comparing $3{\cdot}10^{14}\,\mathrm{n_{eq}/cm^2}$ neutrons with additional 80 kGy x-rays to pure 80 kGy x-rays, the difference of interstrip resistance of about one order of magnitude is visible. This supports the assumption about compensation effects

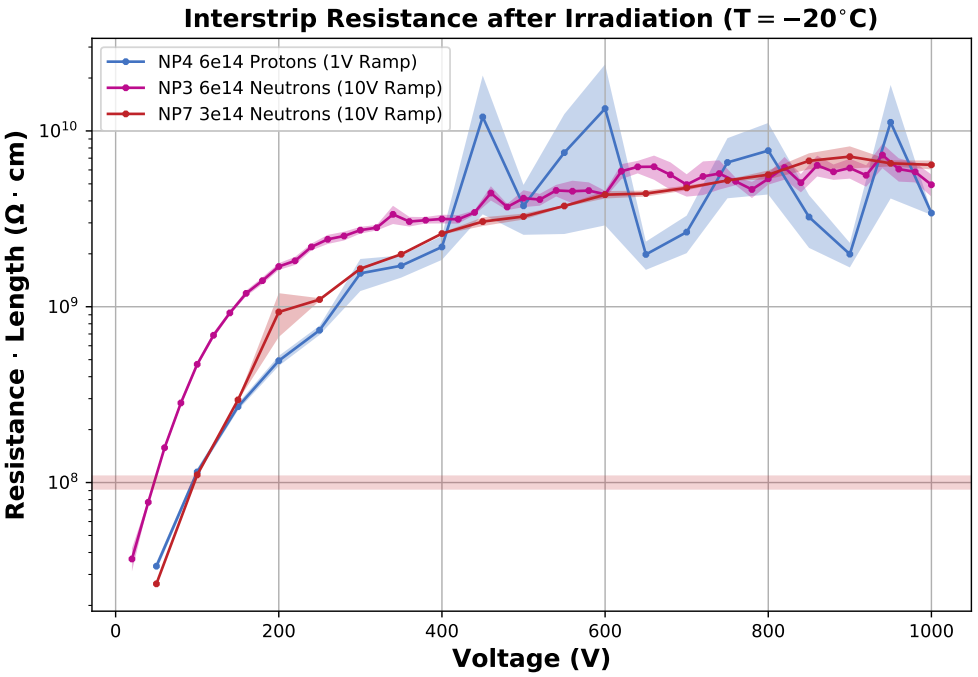

Figure 6.11.: Interstrip resistance compared for proton and neutron irradiation. The behaviour after proton irradiation (blue) fluctuates more due to the 1 V ramp measurement procedure.

due to the bulk defects introduced by the neutron irradiation. The red band is reached at 200 V for the NP7, even when the surface defects are saturated. This is about 250 V less compared to pure x-rays without bulk defects.

A neutron irradiated sensor with a higher fluence of $6{\cdot}10^{14}\,\mathrm{n_{eq}/cm^2}$ and therefore increased bulk defect concentration was irradiated further with x-rays as well. The corresponding interstrip resistance behaviour is displayed in figure 6.13. Similarly to $3{\cdot}10^{14}\,\mathrm{n_{eq}/cm^2}$, the resistance behaviour saturates at significantly lower voltages than for pure x-ray irradiation. After 80 kGy additional irradiation, the interstrip resistance is already sufficient at 100 V operating voltage. This is approximately 350 V less than for pure x-ray irradiation. Additional to the fact that compensation effects are directly visible, it is also visible that the effects scale with the fluence. This results explain why the proton irradiated sensor shows a similar interstrip resistance behaviour than the neutron irradiated sensors. The deposited dose in the surface is over a factor 100 higher, but higher doses are not affecting the isolation anymore, since the oxide charge concentration cannot increase further.

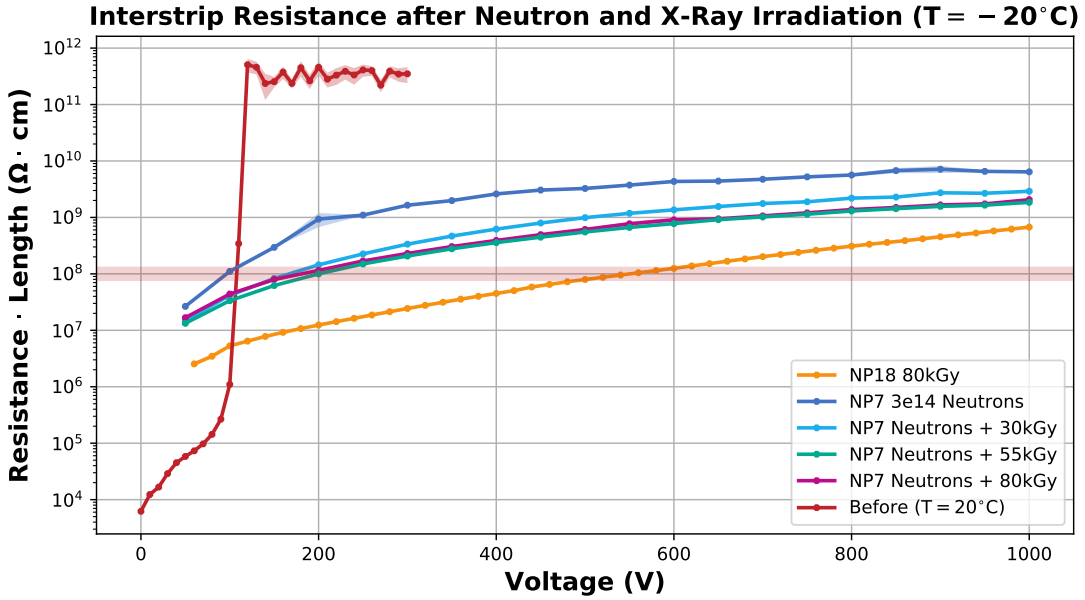

Figure 6.12.: Interstrip resistance after $3{\cdot}10^{14}\,\mathrm{n_{eq}/cm^2}$ neutron and additional x-ray irradiation compared to pure x-ray irradiation. The resistance of the neutron irradiated sample is higher, even after additional x-ray irradiation.

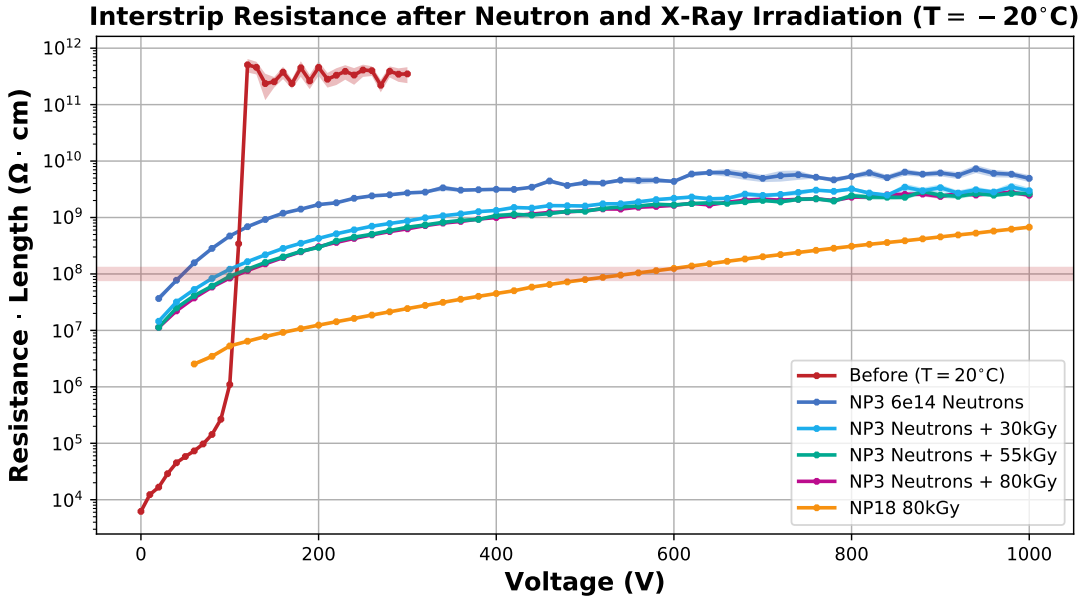

Figure 6.13.: Interstrip resistance after $6{\cdot}10^{14}\,\mathrm{n_{eq}/cm^2}$ neutron irradiation and further x-ray irradiation. With a dose of 80 kGy and pure x-ray irradiation the resistance reaches $10^8\,\Omega$cm at 450 V. Compensation effects due to the neutron irradiation lead to the same resistance with a bias voltage of 100 V.

7. Conclusion

In the course of the HL-LHC the integrated luminosity will increase to $3000\,\mathrm{fb}^{-1}$. This results in a harsh radiation environment for the detectors, especially for the tracker near the beampipe. The CMS detector will therefore require increased radiation hardness and further general improvements through the Phase-2 Upgrade.

One crucial requirement for sensors in the 2S modules of the Outer Tracker in Phase-2 is a sufficient signal after the maximum expected fluence of $\Phi \approx 3 \cdot 10^{14}\,\mathrm{n_{eq}/cm^2}$. Since the readout will be binary, the single channel signal height should exceed a qualification limit of 12 000 electrons. Within this thesis it was shown that 240 µm and 300 µm thick material can reach the requirement with the nominal operating voltage of 600 V. Material with a thickness of 200 µm can be excluded for the 2S region, since its signal is below the specified margin. While investigating the sensors regarding the thickness, a difference in neutron and proton irradiation was observed. Neutron irradiated material tends to have a stronger reverse annealing than proton irradiated sensors. This results in a lower signal of about 1 500 electrons after effective 60 weeks at room temperature for 240 µm material at the nominal operating voltage of 600 V and irradiation with a fluence of $\Phi = 3 \cdot 10^{14}\,\mathrm{n_{eq}/cm^2}$. The effect is more pronounced for higher fluences as well as thicker material. The investigated sensors were manufactured via deep diffusion technology. While processing, the material is heated-up to push dopants from the backside further into the bulk. Moreover, oxygen is diffusing from the environment into the sensors as well. A dependence of the annealing behaviour on the irradiation type was not observed for standard float zone material. This led to the hypothesis that the oxygen concentration causes less reverse annealing in a proton irradiation environment.

An new study with n-type sensors of 300 µm thickness was started to further investigate the annealing behaviour regarding neutron and proton irradiation of different materials. The stronger reverse annealing of neutron irradiated samples could be validated with magnetic Czochralski and diffusion oxygenated material. For float zone material, no difference was observed in the annealing behaviour after neutron and proton irradiation. Therefore the hypothesis that oxygen enrichment leads to a suppressed annealing behaviour of proton irradiated samples is strongly supported.

Samples of the four material types, n-type magnetic Czochralski, diffusion oxygenated float zone, float zone, and p-type deep diffused material were also irradiated with both protons and neutrons. The deep diffused p-type material was irradiated with $3{\cdot}10^{14}\,\mathrm{n_{eq}/cm^2}$ neutrons first and $3{\cdot}10^{14}\,\mathrm{n_{eq}/cm^2}$ protons afterwards. It was observed that the depletion

voltage was unchanged after the second irradiation. This indicates strong compensation effects caused by proton induced defects in a neutron irradiated bulk. Compensation effects were observed in a similar way on all n-type materials. Therefore, these effects are independent of the oxygen concentration. They did not occur when a proton irradiated sample was further irradiated by neutrons. The compensation effects are independent of the material type, n-type or p-type, as well as the oxygen concentration, because similar effects were visible for the four investigated materials. Regarding the signal of mixed irradiation the annealing behaviour of both irradiation orders were similar for float zone material. Less reverse annealing showed up for diffusion oxygenated material just for one out of two sensors. However, prior to any annealing, a significant difference in the voltage dependency was observed dependent on the irradiation order. As expected due to the CV characteristics, proton irradiation after neutron irradiation results in a higher signal than the other way round. This signal offset disappears after annealing. On the other hand, as indicated by measurements on the diffusion oxygenated material, magnetic Czochralski material shows significantly less reverse annealing for the irradiation order protons after neutrons. The difference in the voltage dependency was visible as well without annealing and disappeared after 14 days annealing time. However, after 203 days of annealing the proton after neutron irradiated samples showed a higher signal again. This features have to be investigated further with measurements and simulations.

A new extensive irradiation study of 300 µm and thinned 240 µm material will finalise the material choice for Phase-2. The irradiations will be composed similarly to the expected fractions of neutrons and charged particles in the tracker. It is recommended to irradiate with protons before neutron irradiation for the mixed irradiation to avoid compensation effects, which might not be generated during operation. The actual irradiation in the Tracker could only be emulated by a beam of mixed particles which simultaneously and continuously generate their distinctive defects. Mixed irradiations as they were performed in this study are not able to realisticly mimic the radiation environment in the HL-HLC.

Strip isolation is another issue with p-type sensors after irradiation. Without a specific isolation structure, the interstrip resistance is expected to be lost after a certain fluence. A p-stop implant, which is a highly p-doped region between the strips, is implemented to prevent this from happening. However, the doping concentration has to be handled with care. If it is too high, the electric field at the strips after heavy irradiation will increase dramatically. Therefore a low doping concentration is favorable if it is still sufficient to preserve the spatial resolution.

A set of No_Pstop sensors was used to evaluate surface defects and compensation effects due to bulk damage. These sensor are n-in-p type without any specific isolation structure between strips. It is expected that an electron accumulation layer is formed due to impurities and radiation induced charge in the silicon oxide surface. This decreases the interstrip resistance and eventually short-circuits the strips, which corrupts the spatial resolution of the device. Despite these expectations, after pure x-ray irradiation with 80 kGy the samples still showed a sufficient interstrip resistance for 450 V bias voltage at −20°C. At 20°C the interstrip resistance becomes insufficient for every bias voltage after a certain dose < 30 kGy.

Irradiation with neutrons causes mainly bulk defects. A relatively small amount of oxide charge is also induced in the surface due to gamma background in a spallation reactor. After pure neutron irradiation the interstrip resistance is sufficient even for low bias voltages. An additional irradiation with x-rays to increase the surface damage results in saturation at roughly 55 kGy. The interstrip resistance is then sufficient above 100 V operating voltage for $6{\cdot}10^{14}\,\mathrm{n_{eq}/cm^2}$ neutrons and at 200 V for neutron irradiation with a fluence of $3{\cdot}10^{14}\,\mathrm{n_{eq}/cm^2}$.

Therefore strong compensation effects of surface damage due to bulk defects were observed. The dependence of these effects on the fluence is also illustrated.

In contrast to neutrons, low energy protons deposit a significant amount of dose in the silicon oxide layer (150 kGy per $1 \cdot 10^{14}\,\mathrm{n_{eq}/cm^2}$). However, as shown in this thesis, the surface defects tend to saturate already at doses of 55 kGy. Therefore additional charge deposit at the surface does not further decrease the interstrip resistance anymore. The interstrip resistance after proton and neutron irradiation with additional x-ray irradiation was compared. No hints of a different behaviour between neutron and proton irradiation were visible.

One more technically interesting question is how the interstrip isolation behaves for lower proton fluences. At fluences below $1 \cdot 10^{13}\,\mathrm{n_{eq}/cm^2}$, the bulk defect concentration is significantly lower because it scales linearly with the fluence. However, the surface damage is already saturated, wherefore it is not clear if the interstrip resistance is sufficient and for which bias voltage. This intermediate fluence range is where a p-stop concentration is beneficial to maintain the isolation and therefore spatial resolution.

The decreasing spatial resolution can be monitored by the cluster size of the signal additionally to the interstrip resistance. It is expected to significantly increase due to the charge sharing between the strips if the isolation is not sufficient . Therefore the cluster size of sensors, irradiated similarly to the samples within this thesis, will be investigated further to gain more information about the impact of surface damage.

Bibliography

[AG] Zyklotron AG. *ZAG-Uebersicht*. URL: http://www.zyklotron-ag.de/de/zag-uebersicht.

[AIDa] AIDA. *AIDA website*. URL: http://aida2020.web.cern.ch/.

[AIDb] AIDA. *JSI Transnational Access*. URL: http://aida2020.web.cern.ch/content/jsi.

[AIDc] AIDA. *KIT Transnational Access*. URL: http://aida2020.web.cern.ch/content/kit.

[AZS17] K. Ambrozic, G. Zerovnik, and L. Snoj. *Computational analysis of the dose rates at JSI TRIGA reactor irradiation facilities*. In: Applied Radiation and Isotopes 130 (2017), pp. 140–152. ISSN: 0969-8043. DOI: https://doi.org/10.1016/j.apradiso.2017.09.022.

[Ber+17] M.J. Berger et al. *Stopping-Power and Range Tables for Electrons, Protons, and Helium Ions*. July 2017. URL: https://www.nist.gov/pml/stopping-power-range-tables-electrons-protons-and-helium-ions.

[CER] CERNpress. URL: http://press.cern/backgrounders/facts-figures.

[CER17] CERN. *The CERN-ESE-ME X-ray irradiation system for TID studies in microelectronics*. Jan. 2017. URL: http://proj-xraymic.web.cern.ch/proj-XrayMIC/Xraycalibration_files/CalibrationJan2017.pdf.

[Chi13] A Chilingarov. *Temperature dependence of the current generated in Si bulk*. In: Journal of Instrumentation 8.10 (2013), P10003. URL: http://stacks.iop.org/1748-0221/8/i=10/a=P10003.

[Col] The CMS Collaboration. *CMS website*. URL: https://cms.cern/detector.

[Col15] CMS Collaboration. *1-D plot covering CMS tracker, showing FLUKA simulated 1 MeV neutron equivalent in Silicon including contributions from various particle types*. In: (July 2015). URL: https://cds.cern.ch/record/2039908.

[Col17] CMS Collaboration. *The Phase-2 Upgrade of the CMS Tracker*. Tech. rep. CERN-LHCC-2017-009. CMS-TDR-014. Geneva: CERN, June 2017. URL: http://cds.cern.ch/record/2272264.

[Col99] The ROSE Collaboration. *3RD RD48 STATUS REPORT*. Dec. 1999. URL: http://rd48.web.cern.ch/RD48/status-reports/rd48-3rd-status-report.pdf.

[Dal+14] R Dalal et al. *Combined effect of bulk and surface damage on strip insulation properties of proton irradiated n^+-p silicon strip sensors*. In: Journal of Instrumentation 9.04 (2014), P04007. URL: http://stacks.iop.org/1748-0221/9/i=04/a=P04007.

[Die13] Alexander Dierlamm. *Planar sensors for future Vertex and Tracking Detectors*. In: PoS Vertex2013 (2013), p. 027. DOI: 10.22323/1.198.0027.

[Erf09] Joachim Erfle. *Entwicklungen für neue Siliziumstreifensensoren und deren Qualitätskontrolle*. Sept. 2009. URL: http://www-ekp.physik.uni-karlsruhe.de/~thesis/data/iekp-ka2009-27.pdf.

[Eur14] Edifici Eureka. *Activity Book for Students*. Bellaterra, Barcelona, 2014. URL: https://www.alibavasystems.com/images/EASy-exercises/EASY-Exercise-Book.pdf.

[Exp] Institute of Experimental Particle Physics (ETP). *X-Ray Irradiation*. URL: https://www.etp.kit.edu/english/265.php.

[Fre+02] E. Fretwurst et al. *Radiation damage in silicon detectors caused by hadronic and electromagnetic irradiation*. In: *Radiation effects on semiconductor materials, detectors and devices. Proceedings, 4th International Conference, RESMDD'02, Florence, Italy, July 10-12, 2002*. 2002. arXiv: physics/0211118 [physics].

[G+17] Apollinari G. et al. *High-Luminosity Large Hadron Collider (HL-LHC): Technical Design Report V. 0.1*. CERN Yellow Reports: Monographs. Geneva: CERN, 2017. URL: https://cds.cern.ch/record/2284929.

[Gal14] Yuri M. Galperin. *Introduction to Modern Solid State Physics*. Sept. 2014. URL: http://folk.uio.no/yurig/fys448/f448pdf.pdf.

[Gut+12] M. Guthoff et al. *Geant4 simulation of a filtered X-ray source for radiation damage studies*. In: Nuclear Instruments and Methods in Physics Research Section A: Accelerators, Spectrometers, Detectors and Associated Equipment 675 (2012), pp. 118–122. ISSN: 0168-9002. DOI: https://doi.org/10.1016/j.nima.2012.01.029.

[Haf13] Julie Haffner. *The CERN accelerator complex. Complexe des accélérateurs du CERN*. In: (Oct. 2013). General Photo. URL: http://cds.cern.ch/record/1621894.

[Har17] Frank Hartmann. *Evolution of Silicon Sensor Technology in Particle Physics*. 2017. DOI: 10.1007/978-3-319-64436-3.

[Hei] ASIC Laboratory Heidelberg. *Beetle - a readout chip for LHCb*. URL: http://www.kip.uni-heidelberg.de/lhcb/.

[Hei07] Uni Heidelberg. *Picture of the Beetle Chip*. Apr. 2007. URL: http://www.kip.uni-heidelberg.de/lhcb/Pictures/Beetle13/Gallery/Beetle13on13board3.jpg.

[Hen06a] Markus A. Henning. *Dotierung im zweidimensionalen Siliziumkristallgitter mit Aluminium*. Jan. 2006. URL: https://upload.wikimedia.org/wikipedia/commons/0/0d/Schema_-_p-dotiertes_Silicium.svg.

[Hen06b] Markus A. Henning. *Dotierung im zweidimensionalen Siliziumkristallgitter mit Phosphor*. Jan. 2006. URL: https://upload.wikimedia.org/wikipedia/commons/2/22/Schema_-_n-dotiertes_Silicium.svg.

[HM06] Werner Herr and B Muratori. *Concept of luminosity*. In: (2006). URL: https://cds.cern.ch/record/941318.

[Hof11] K.-H. Hoffmann. *Campaign to identify the future CMS tracker baseline*. In: Nuclear Instruments and Methods in Physics Research Section A: Accelerators, Spectrometers, Detectors and Associated Equipment 658.1 (2011). RESMDD 2010, pp. 30–35. ISSN: 0168-9002. DOI: https://doi.org/10.1016/j.nima.2011.05.028.

[Huh02] M. Huhtinen. *Simulation of non-ionising energy loss and defect formation in silicon*. In: Nuclear Instruments and Methods in Physics Research Section A: Accelerators, Spectrometers, Detectors and Associated Equipment 491.1 (2002), pp. 194–215. ISSN: 0168-9002. DOI: https://doi.org/10.1016/S0168-9002(02)01227-5.

[Ins] National Instruments. *LabVIEW 2018*. URL: http://www.ni.com/de-de/shop/labview/labview-details.html.

[KK] Hamamatsu Photonics K.K. URL: https://www.hamamatsu.com/jp/en/index.html.

[Kup09] Tony R. Kuphaldt. *Lessons In Electric Circuits, Volume III – Semiconductors*. Mar. 2009. URL: https://www.ibiblio.org/kuphaldt/electricCircuits/Semi/SEMI.pdf.

[Löc06] Sven Löchner. *Development, Optimisation and Characterisation of a Radiation Hard Mixed-Signal Readout Chip for LHCb*. PhD thesis. Ruperto-Carola University of Heidelberg, 2006. URL: https://cernbox.cern.ch/index.php/s/OjZci0bAVlCLNBw.

[Lop17] Ewa Lopienska. *LHC Guide*. CERN-Brochure-2017-002-Eng. Mar. 2017. URL: http://cds.cern.ch/record/2255762.

[Mol99] Michael Moll. *Radiation damage in silicon particle detectors: Microscopic defects and macroscopic properties*. PhD thesis. Hamburg U., 1999. URL: http://www-library.desy.de/cgi-bin/showprep.pl?desy-thesis99-040.

[MT12] Thomas Mc Cauley and Lucas Taylor. *CMS Higgs Search in 2011 and 2012 data: candidate ZZ event (8 TeV) with two electrons and two muons: 3D perspective, r-phi and r-z views*. CMS Collection. July 2012. URL: https://cds.cern.ch/record/1606502.

[NISa] NIST. *PSTAR program*. URL: https://physics.nist.gov/PhysRefData/Star/Text/PSTAR.html.

[NISb] NIST. *SI Redefinition*. URL: https://www.nist.gov/si-redefinition.

[Off96] CERN Program Library Office. *CERN Program Library*. June 1996. URL: https://root.cern.ch/sites/d35c7d8c.web.cern.ch/files/cernlib.pdf.

[Oli+14] K.A. Olive et al. *Review of Particle Physics*. In: Chinese Physics C 38.9 (2014), p. 090001. URL: http://stacks.iop.org/1674-1137/38/i=9/a=090001.

[Pel+05] G. Pellegrini et al. *Characterization of magnetic Czochralski silicon radiation detectors*. In: Nucl. Instrum. Meth. A548 (2005), pp. 355–363. DOI: 10.1016/j.nima.2005.05.001.

[RD5] RD50. *Status of the NitroStrip Project*. URL: https://agenda.infn.it/contributionDisplay.py?contribId=8&sessionId=2&confId=11109.

[SR52] W. Shockley and W. T. Read. *Statistics of the Recombinations of Holes and Electrons*. In: Phys. Rev. 87 (5 Sept. 1952), pp. 835–842. DOI: 10.1103/PhysRev.87.835.

[SYS] ALIBAVA SYSTEMS. *Alibava website*. URL: https://www.alibavasystems.com/.

[Sys14] Alibava Systems. *Alibava User's Manual*. 2014. URL: https://www.alibavasystems.com/images/Catalogo/alibava-usermanual.pdf.

[Tan+18] M. Tanabashi et al. *Passage of particles through matter*. 2018. URL: http://pdg.lbl.gov/2018/mobile/reviews/pdf/rpp2018-rev-passage-particles-matter-m.pdf.

[Tay11] Lucas Taylor. Nov. 2011. URL: http://cms.web.cern.ch/news/how-cms-detects-particles.

[The07] User: TheNoise. *A p-n junction in thermal equilibrium*. Aug. 2007. URL: https://upload.wikimedia.org/wikipedia/commons/d/d6/Pn-junction-equilibrium.png.

[Wel] Weltmaschine. *Das Standardmodell der Teilchenphysik*. URL: https://www.weltmaschine.de/physik/standardmodell_der_teilchenphysik/.

[Wun92] Renate Wunstorf. *Systematische Untersuchungen zur Strahlresistenz von Silizium-Detektoren fuer die Verwendung in Hochenergiephysik-Experimenten*. 1992. URL: https://www-h1.desy.de/psfiles/theses/h1th-812.pdf.

Appendix

A. Appendix to Chapter 3

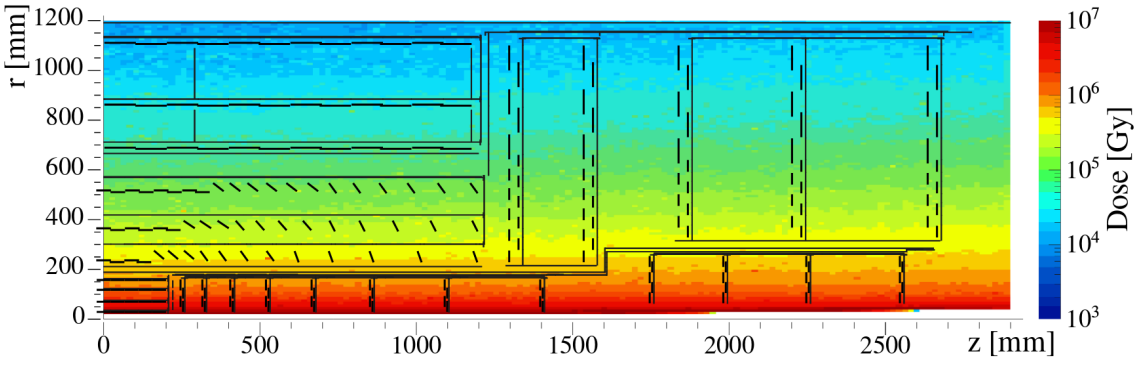

Figure A.1.: Expected dose in Gy for Phase-2 based on FLUKA simulations [Col17].

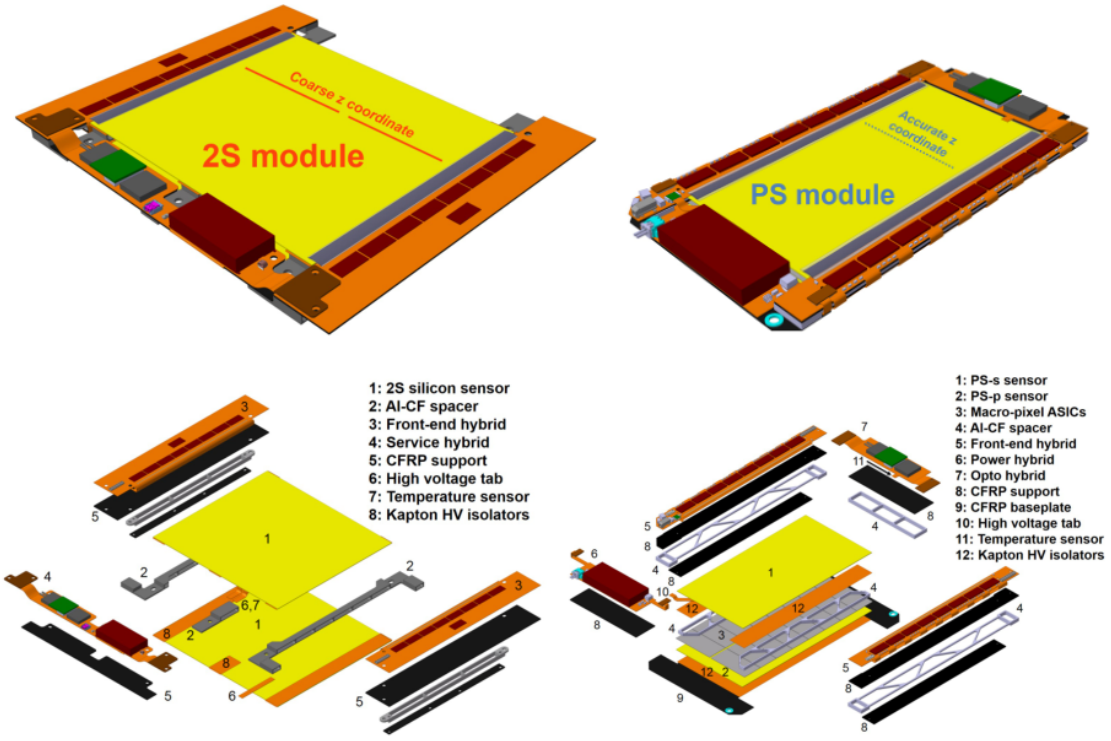

Figure A.2.: Sketch of p_T-modules for the Phase-2 Upgrade of the CMS experiment. 2S modules on the left side incorporate two back-to-back strip sensors. The PS modules, displayed on the right, house a macropixel sensor and a strip sensors. Further components are illustrated in the exploded view below [Col17].

B. Appendix to Chapter 4

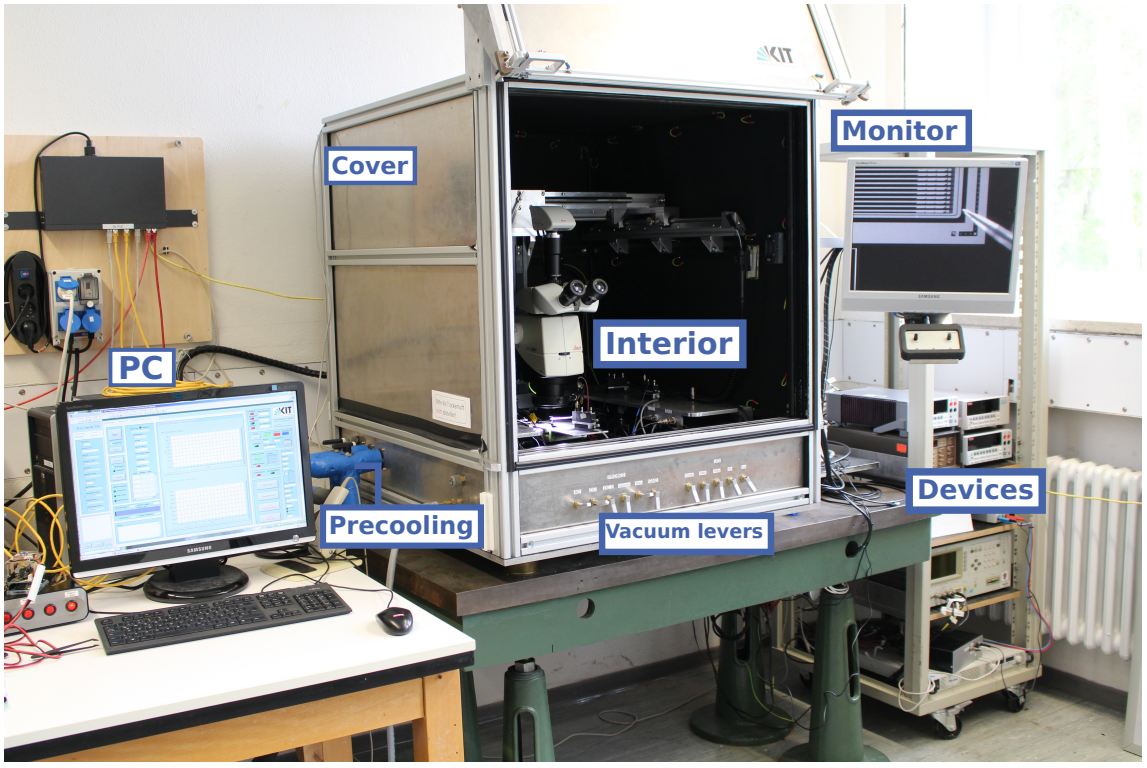

Figure B.1.: Probe Station at ETP. The interior of the probe station is covered by an aluminum box. Vacuum levers are used to fixed needle holders and sensors on the jig. The whole setup is controlled via a PC.

Table B.1.: Usual steps for annealing studies. After every step IV and charge collection measurements were performed.

Step Number	Time (min)	Temperature (°C)	Equivalent time at room temperature (d)
1	20	60	3.75
2	20	60	6.88
3	40	60	13.25
4	76	60	27.1
5	15	80	77.96
6	30	80	203.92
7	60	80	416.96

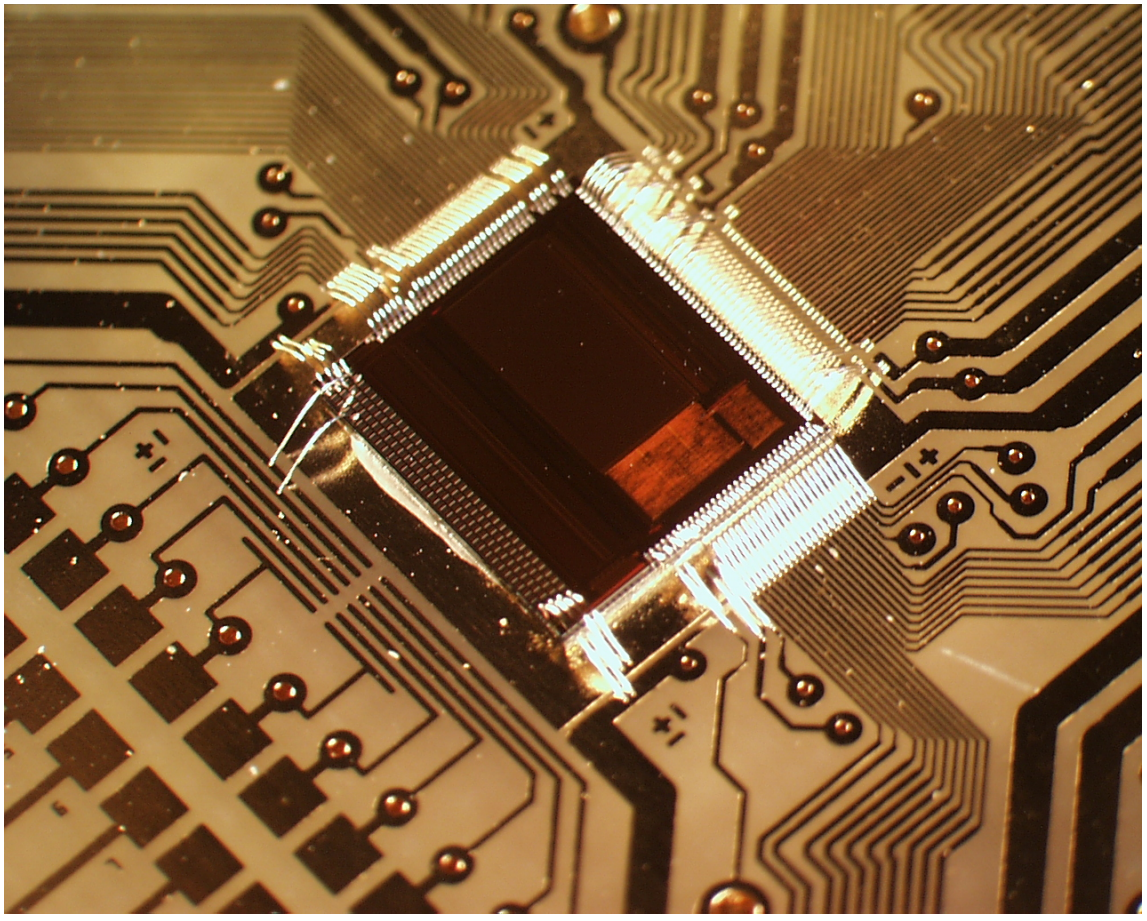

Figure B.2.: Picture of the Beetle chip designed by Uni Heidelberg [Hei07].

C. Appendix to Chapter 5

Table C.2.: Sensors with their name within the HPK campaign, demanded fluence and real fluence. The abbreviation n/a stands for 'not available'.

Plot Label	Name	Demanded Fluence	Real Fluence
200C1	KIT_Test_07	$3 \cdot 10^{14} n_{eq}/cm^2$	n/a
200C3	PCommon_07	$3 \cdot 10^{14} n_{eq}/cm^2$	n/a
200S3	PCommon_06	$6 \cdot 10^{14} n_{eq}/cm^2$	n/a
240C1	Irradiation_23	$3 \cdot 10^{14} n_{eq}/cm^2$	n/a
240C2	Irradiation_22	$3 \cdot 10^{14} n_{eq}/cm^2$	n/a
240C5	Irradiation_7	$6 \cdot 10^{14} n_{eq}/cm^2$	n/a
240C7	PCommon_7	$6 \cdot 10^{14} n_{eq}/cm^2$	n/a
240C8	KIT_Test_07	$3 \cdot 10^{14} n_{eq}/cm^2$	n/a
240S1	Irradiation_04	$6 \cdot 10^{14} n_{eq}/cm^2$	n/a
240S2	KIT_Test_08	$6 \cdot 10^{14} n_{eq}/cm^2$	n/a
240S3	Irradiation_18	$6 \cdot 10^{14} n_{eq}/cm^2$	n/a
300S1	FZ320P_04_Badd_1	$3 \cdot 10^{14} n_{eq}/cm^2$	$2.6 \cdot 10^{14} n_{eq}/cm^2$
300S2	FZ320Y_04_Badd_1	$3 \cdot 10^{14} n_{eq}/cm^2$	$2.6 \cdot 10^{14} n_{eq}/cm^2$
300S4	FZ320P_06_BPA_1	$6 \cdot 10^{14} n_{eq}/cm^2$	$5.5 \cdot 10^{14} n_{eq}/cm^2$
300S5	FZ320P_07_BPA_1	$6 \cdot 10^{14} n_{eq}/cm^2$	$6.11 \cdot 10^{14} n_{eq}/cm^2$
300S6	FZ320P_04_Bstd_2	$5 \cdot 10^{14} n_{eq}/cm^2$	$5 \cdot 10^{14} n_{eq}/cm^2$

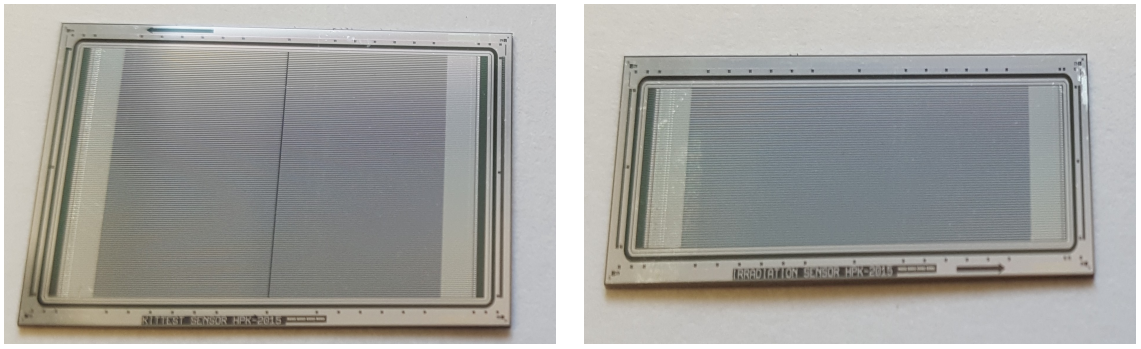

(a) (b)

Figure C.1.: Picture of a KIT_Test (a) and an Irradiation (b) type sensor.

Table C.3.: NitroStrip sensors with their respective plot label and particle type. All sensors are irradiated with a fluence of $\Phi_{tot} = 6 \cdot 10^{14}\,n_{eq}/cm^2$ pure or mixed.

Sample	Plot Label	Particle Type
NS_w19_S21	MCZ1	p
NS_w19_S23	MCZ2	p
NS_w13_S8	DOFZ1	p
NS_w16_S1	DOFZ2	p
NS_w1_S14	FZ1	p
NS_w1_S18	FZ2	p
NS_w19_S12	MCZ3	n
NS_w19_S3	MCZ4	n
NS_w13_S17	DOFZ3	n
NS_w13_S11	DOFZ4	n
NS_w1_S23	FZ3	n
NS_w1_S19	FZ4	n
NS_w19_S11	MCZ5	n+p
NS_w19_S10	MCZ6	n+p
NS_w13_S2	DOFZ5	n+p
NS_w13_S19	DOFZ6	n+p
NS_w1_S24	FZ5	n+p
NS_w1_S15	FZ6	n+p
NS_w19_S13	MCZ7	p+n
NS_w19_S7	MCZ8	p+n
NS_w13_S3	DOFZ7	p+n
NS_w13_S4	DOFZ8	p+n
NS_w1_S21	FZ7	p+n
NS_w1_S22	FZ8	p+n

D. Appendix to Chapter 6

Table D.4.: No_Pstop sensors with their respective plot label, thickness and project.

Name	Plot Label	Thickness	Project
No_Pstop_02	NP1	200	HPK_2S_II
No_Pstop_04	NP2	200	HPK_2S_II
No_Pstop_05	NP3	200	HPK_2S_II
No_Pstop_06	NP4	200	HPK_2S_II
No_Pstop_07	NP5	200	HPK_2S_II
No_Pstop_01	NP6	240	HPK_2S_I
No_Pstop_18	NP7	240	HPK_2S_I
No_Pstop_19	NP8	240	HPK_2S_I
No_Pstop_21	NP9	240	HPK_2S_I
No_Pstop_23	NP10	240	HPK_2S_I
No_Pstop_03	NP11	240	HPK_2S_I
No_Pstop_04	NP12	240	HPK_2S_I
No_Pstop_07	NP13	240	HPK_2S_I
No_Pstop_08	NP14	240	HPK_2S_I
No_Pstop_11	NP15	240	HPK_2S_I
No_Pstop_12	NP16	240	HPK_2S_I
No_Pstop_14	NP17	240	HPK_2S_I
No_Pstop_15	NP18	240	HPK_2S_I
No_Pstop_16	NP19	240	HPK_2S_I
No_Pstop_22	NP20	240	HPK_2S_I

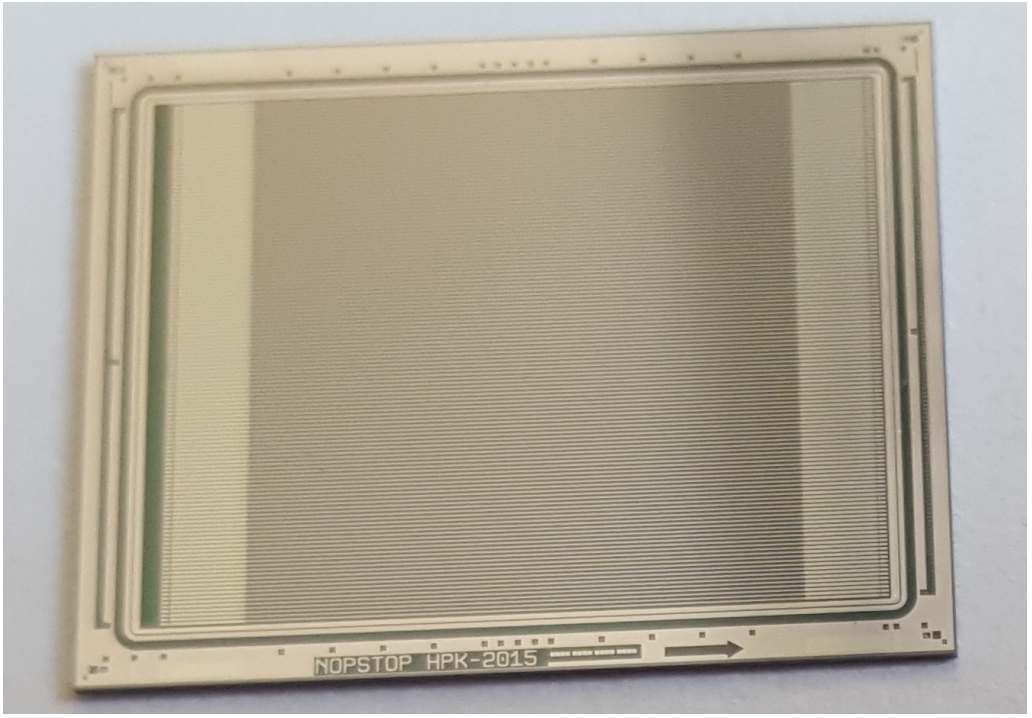

Figure D.2.: Picture of a No_Pstop type sensor with a strip length of 1.45 cm.

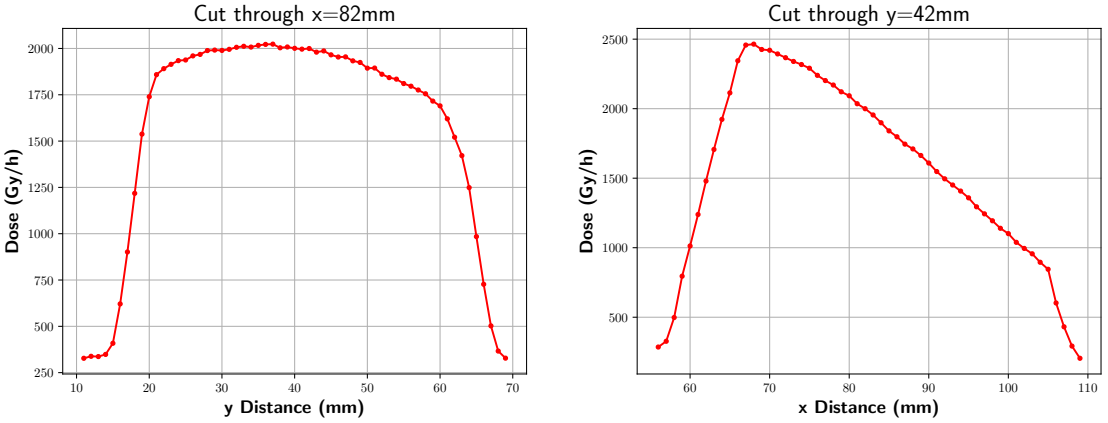

(a) (b)

Figure D.3.: Cross sections for the beamspot profile at 300 mm. Cut through the x-axis (a) and y-axis (b). An inhomogeneity is visible in the x direction.

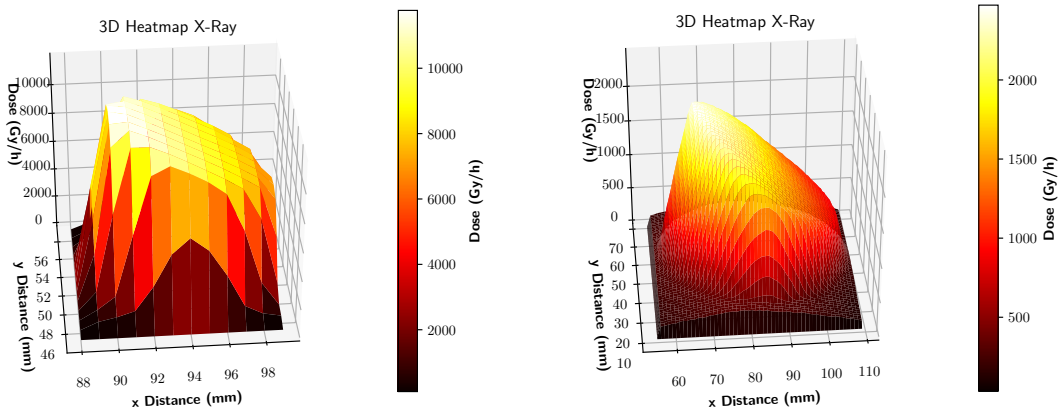

(a) (b)

Figure D.4.: Three-dimensional illustration of the beamspot profile for a distance of 100 mm (a) and 300 mm (b). In (b) the maximum dose is approximately 2482 Gy/h and the mean 1636 Gy/h.

Danksagung

Abschließend bedanke ich mich bei allen, die mich während der Zeit der Masterarbeit unterstützt und maßgeblich zum Gelingen beigetragen haben.

Prof. Dr. Thomas Müller danke ich für die Ermöglichung dieser Abschlussarbeit in der CMS-Gruppe des ETP und der hilfreichen Kommentare bezüglich meiner Arbeit am Institut. Für die Übernahme des Korreferats danke ich Prof. Dr. Ulrich Husemann.

Für die exzellente Betreuung und sehr konstruktiven Diskussionen woraus sich regelmäßig neue spannende Fragestellung ergaben, danke ich Dr. Alexander Dierlamm.

Bei Marius Metzler möchte ich mich für die verständnisvolle Betreuung in der Anfangsphase und späteren anregenden Diskussionen bedanken, sowie für die herausragenden Beratungen bezüglich Präsentationen, insbesondere im Englischen.

Meinen Zimmerkollegen Alexander Droll und Roland Koppenhöfer danke ich für die alltäglichen Dinge im Institutsleben und permanenter Unterstützung. Ebenso danke ich für die Beratung durch Dr. Andreas Nürnberg und Dr. Hans-Jürgen Simonis.

Für die ausgezeichnete Arbeit an Mechanik und Elektronik möchte ich mich bei Tobias Barvich, Pia Steck und Anita Weddigen bedanken. Zusätzlich zu dieser gilt mein Dank Felix Bögelspacher für die zuverlässigen Bestrahlungen mit Protonen am Zyklotron.